Utrecht University

Graduate school of natural sciences

Institute for theoretical physics

Spin-Orbit coupling in a fractal lattice.

Robert Cañellas Núñez

June 2021

Master's thesis

under the supervision of

Prof. Dr. Cristiane Morais Smith
PhD. Rodrigo Arouca

Abstract

Topological states of matter have attracted great attention during the last decades. These states are insulating in the bulk, but conducting at the edges. In addition, the conductivity is quantized and protected by a topological invariant. The quantum spin Hall effect (QSHE) is one of the hallmarks of topological states of matter. Besides its importance in fundamental science, it has potential technological applications, but a large bulk gap must be realized for these applications, to protect the topological edge states. Since one of the main ingredients to obtain the QSHE in Kane and Mele's work is related to the spin-orbit coupling, heavy elements with a strong spin-orbit coupling provide an ideal platform to obtain a robust QSHE phase. In fact, it has been shown theoretically and experimentally that ultrathin free-standing layers of Bi, called Bismuthene, present topological phases at room temperature. Recently, an experimental group demonstrated that Bi deposited on top of the semiconductor InSb forms atomic thin fractal structures. An interesting question is whether these Sierpisnki-like structures can host topological phases. We simulate this system using a muffin-tin method, and show that for some values of spin-orbit coupling indeed there are corner and edge modes that could have a topological origin. Moreover, our results describe the local density of states obtained experimentally. This work contributes to the more general question of whether topological states of matter may exist at non-integer dimensions.

Acknowledgments

The work presented here has been achieved mainly for the enormous effort of both my supervisors, who were able to keep me motivated along this year. They guide me through the process, while having many useful discussions. I wave learned much more apart from physics, including the my writing skills and organization. To this and much more, I would like to thank them for their patience.

I would like to tanks as well all my friends and family which gave me support for finishing this master.

Contents

Introduction

In the last two centuries, we have developed novel theoretical frameworks to describe phases of matter. The conventional perspective of band theory, which was adequate to classify metals, insulators, and semiconductors required further refinements to include more exotic materials such as superconductors and quantum Hall fluids. More concretely, the need of topological concepts to describe the Kosterlitz-Thouless transition [1] triggered the development of a set of new ideas to explain what we know nowadays as topological insulators. Topological insulators are materials that are insulating in the bulk, but conduct current along the boundaries. These metallic edge states are very robust because they are protected by symmetries.

The first observation of a topological insulator was the integer quantum Hall effect (IQHE) [2]. Right after its discovery, a topological invariant was identified, the so-called Chern number ($\mathbb{Z}$) [3]. The classification of the IQHE in terms of a topological invariant set the foundations of this new class of materials and remained the only known invariant until the work of Kane and Mele [4, 5]. In their work, they developed a toy model for graphene in which the intrinsic spin-orbit coupling between the next-nearest neighbours was opening a topological gap. For this time-reversal topological insulator, they introduced a new $\mathbb{Z}_2$ topological invariant that labels a trivial phase and a non-trivial one. In this model, instead of having chiral charge currents along the edge as in the integer quantum Hall phase, there are helical spin currents because spin up and down counter-propagate. This new state of matter, the quantum spin Hall phase, seemed very promising for future technological applications but it had some drawbacks. The operating temperature was cryogenic because, the gap in graphene was too small. Hence, a way to achieve a room temperature quantum spin Hall phase is to enlarge the topological gap by using heavier atoms, such as Bismuth from group V. Recent studies show that ultrathin free standing honeycomb layers of Bi atoms are indeed topological and host the quantum spin Hall phase at room temperature [6].

After the discovery by Kane and Mele, it became clear that a generic classification of topological insulators in terms of symmetries could be achieved. Indeed, depending on which of the three discrete symmetries are present (time-reversal, particle-hole or chiral), the topological insulator will reside in one of the ten symmetry classes. Then, depending on their integer dimension, there will be a topological invariant associated to them. This classification is known as the ten-fold way or the Altland-Zirnbauer symmetry classes [7]. This classification scheme (the ten-fold way) holds for non-interacting fermions, but it has recently been extended and generalized to include crystalline symmetries, non-Hermitian Hamiltonians, interacting systems or driven nonequilibrium systems. However, all these tables are constructed for integer dimensions, and not much is known about what would happen in between, for fractional dimensional systems, such as fractals. Recently, an experimental group has been able to synthesize Sierpiński-like islands made of Bi atoms on top of InSb [8]. Moreover, measurements of the local density of states suggest some topological features. Our aim here is to theoretically reproduce their measurements by performing muffin-tin calculations, and verify what happens when a two-dimensional free electron gas with intrinsic spin-orbit coupling is confined into a Sierpiński triangle. Will there be topological features at non-integer dimension or is the fractal structure is going to destroy them all? This is the main question to be answered in this thesis.

The text is divided in eight chapters, conclusions and appendices. In chapter 1, we provide a broad historical review of condensed matter, from the band classification to topological insulators, recalling a few of the most important contributions. Chapter 2 introduces the three discrete symmetries and presents the ten-fold classification. We continue with chapter 3 by introducing some basic concepts of fractals, in particular the Sierpiński triangle. In chapter 4, we derive the second-order contributions in $(v/c)^2$ of the Dirac equation, showing the emergence of the intrinsic spin-orbit coupling term. Then, in chapter 5 we give some overview of recent works related to topology and fractals. In chapter 6, we explain the method used and in chapter 7, we show some of the main results of our simulations. In chapter 8, we compare our results with the experimental measurements from the group of Jinfeng Jia [8]. These last two chapters consist of original work. Finally, we present our conclusions and outlook. A few appendices contain further details of calculations and measurements.

Chapter 1

Quantum states of matter

1.1 Band classification of matter

Condensed matter is a field in physics which attempts to describe how the constituents of matter rearrange among themselves, from a microscopic and macroscopic point of view, focusing mainly in solids and liquid states [9–11]. Depending on different parameters, such as temperature, the electromagnetic field, impurities or disorder, among many others, matter will organize itself in different phases. The last century has been a fruitful period, in which new quantum states of matter, such as superconductors and topological insulator, have been theoretically understood [12]. This would not have been possible without the advance of technology. The development of the Scanning Tunneling Microscope (STM) enabled researchers to obtain images of materials with atomic resolution, and also led to the creation of artificial lattices [13–15]. The Angle-Resolved Photoemission Spectroscopy (ARPES) technique allowed to measure and characterize the electronic structure, and enabled researchers to understand which interactions were the most important [16–19]. Nowadays it would be difficult to think about modern devices that do not use the quantum technologies [20].

Through the 20th century, physicists developed the roots of this field, solid state physics: from the Lorentz-Drude model in 1900, describing a classical free electron gas, to the quantum theory of electrons in solids, from 1928 to 1933 [21]. Two areas where these developments had impact are band theory and magnetism. The former allows one to understand the electronic transport in solids, distinguishing metals from semimetals, semiconductors, and insulators. With the latter, it was possible to explain paramagnetism, diamagnetism, ferromagnetism, and compute magnetic properties of metals, such as the susceptibility.

The discovery of superconductivity by Onnes in 1911 had to wait for nearly fifty years for a theoretical description. Landau succeeded to create a phenomenological theory that could classify different phases of matter. The foundation of this method is that one can expand the thermodynamic potential around the critical point as a power series in the order parameter, thus obtaining an effective field theory. Even though such expansion would be divergent because it contains singularities in higher-order coefficients, Landau argued that predictions can be made examining only the lower-order coefficients [22, 23]. Furthermore, in 1933 Ehrenfest introduced a scheme to classify phase transitions on the basis of jumps in derivatives of the free energy.

Many systems can be described using this systematic approach, where matter experiences a phase transition from a high-temperature symmetric phase characterized by a vanishing order parameter, to a low-temperature symmetry-broken state with a nonzero order parameter. For example, a ferromagnet has a net magnetization pointing to a preferred direction, breaking the rotation symmetry $O(3)$ associated to spins, while antiferromagnets do not have an overall magnetization. Solids break translation symmetry, as atoms form a crystalline structure and

therefore are localized at lattice sites. However, in 1980 von Klitzing *et al.* [2] experimentally discovered the quantum Hall state, a state of matter that could not be described with Landau's approach due to the absence of a *local* order parameter. The quantum Hall state does not break any symmetry, but showed novel physics, such as quantization of the Hall conductance and the appearance of a number of conducting edge modes [2]. These properties are deeply linked to topological features of the quantum state, as they are insensitive to smooth deformations of the parameters. A change is only possible if the system undergoes a quantum phase transition. This led to a new classification framework based on a *topological* order, an idea initially proposed by Thouless *et al.* in 1982 [3] and later refined by Wen in 1995 [24]. Before discussing the concept of topological phases more in depth, it is interesting to understand the corresponding mathematical description, as this will allow us to see its relevance in physics.

Topology is a branch in mathematics, which studies properties of geometric objects that are invariant under smooth deformations [25]. An illustrative example is the sphere, which can be smoothly deformed into any surface that does not contain any hole. Then, we can say that a disk, a bowl or a sphere are topologically equivalent. In contrast, a doughnut would be topologically distinct to the above, as it contains a hole. These statements are encompassed within the Gauss-Bonnet theorem, which asserts that the integral of the Gaussian curvature K of a compact Riemannian manifold defines an integer topological invariant, the Euler characteristic,

$$\chi = \frac{1}{2\pi} \int_S K dA. \tag{1.1}$$

This measure is related to the notion of genus g, the number of holes of the object, by $\chi = 2-2g$.

So, how would all this be related to physics? Notice that we have repeated a key concept, smooth deformations. In mathematics, these are homeomorphisms and homotopies, but in physics the terminology is adiabatic evolution. The underlying physics of a system is obtained from the Hamiltonian: if one can adiabatically connect one Hamiltonian to another without closing the bulk gap, then they correspond to the same topological class [26, 27]. Later, we will define topological invariant quantities to characterize these classes, but before addressing this problem, we will recall how materials are classified within the framework of band theory of solids.

When a solid is crystalline, the atoms are arranged in a periodic potential and we can exploit translation symmetry to label states with crystal momentum $\boldsymbol{k}$ inside the first Brillouin zone, the reciprocal of the Wigner-Seitz primitive cell. Then, Bloch's theorem states that the energy eigenstates take the form $|\psi_{\boldsymbol{k}}\rangle = e^{i\boldsymbol{k}\cdot\boldsymbol{r}} |u(\boldsymbol{k})\rangle$, where $|u(\boldsymbol{k})\rangle$ is the periodic eigenstate of the Bloch Hamiltonian, and the band structure is collectively determine by its eigenvalues $E_n(\boldsymbol{k})$ and eigenvectors $|u_n(\boldsymbol{k})\rangle$ [28].

Atoms are bound to lattice sites and their electrical, optical, and chemical properties are defined from their electronic configuration. There can be many electrons, which will form a many-body ground state described by a Slater determinant of single-particle states, obeying the Pauli exclusion principle and minimizing their energy. Nevertheless, a huge simplification is to assume that only the outer electrons, which are weakly bound to the atom, will determine their properties. There are two types of bands, the *valence* band, fully-filled, and the partially filled (or empty) *conduction* band. It is useful to define this also in terms of the Fermi energy, the chemical potential at zero temperature, as electrons of the *valence* band lie below the Fermi energy, and those from the *conduction* band lie above. This energy also defines the Fermi surface, a constant energy surface in momentum space.

The feature that enables us to distinguish among different materials is the band gap. It appears due to interactions of electrons with the ionic potential, enlarging the difference between the conduction and valence band, and giving rise to a forbidden region in the energy

spectrum.

Now we are in a position to understand the classification of materials using band theory:

- **Insulators** are characterized by a large band gap at the Fermi energy between the highest fully filled valence band and the lowest conduction band. Electrons then need a large energy to be excited towards the conduction band, hence their poor conductivity.
- **Semiconductors** are very similar to insulators, but they differ in that the forbidden band is much smaller, usually less than 2 eV. Electrons can be easily excited by thermal fluctuations. If this jump also involves a change in the momentum, the semiconductor is said to have an *indirect gap* and if not, a *direct gap*. To modify the conductivity, we can dope the material by introducing impurities, which can either accept, *p-type*, or donate, *n-type*, electrons and as a result, move the valence band up or the conduction band down, respectively. Doped semiconductors are called *extrinsic* and the pure ones are called *intrinsic*.
- **Semimetals** contain the Fermi energy inside a band, but the density of states is very poor around it. Nevertheless, at zero temperature they can conduct, contrarily to the first two types of materials above.
- **Metals** are also gapless, and consequently, electrons have many allowed states to populate at a minor energy cost, thus exhibiting a high conductivity.

The phenomenon of superconductivity is an especial case of a conducting material and cannot be explained by the use of band theory. The effect was first observed by Kamerlingh Onnes back in 1911, when he was at Leiden University. He managed to produce liquid Helium for the first time, and this motivated him to study different materials at low temperatures. He observed that the resistance of mercury dropped to zero for temperatures below a critical value. He was awarded with the Nobel Prize in 1913 for this discovery.

A few decades later, Ginzburg and Landau where able to explain the phenomenon macroscopically, but it took nearly fifty years until Bardeen, Cooper and Schireffer formulated a microscopic description of superconductivity, the so-called BCS theory, which gave them the Nobel Prize in 1972 [29, 30].

- **Superconductivity** is a phase of matter in which electrons, mediated by phonon interactions, form pairs below a critical temperature. These so-called Cooper pairs condense in the lowest energy state, and a gap opens in the material. This gap is of the order of thermal energy corresponding to pair formation. The collective behaviour is insensitive to scattering effects, and therefore do not show any resistance. The main difference from a perfect conductor is that in superconductors the magnetic field cannot penetrate the material, a phenomenon known as the Meissner-Ochsenfeld effect.

1.2 Topological states

After having defined the main types of conductors, we can now introduce a new type of materials that emerged at the end of last century and became a prominent field of research in modern condensed-matter physics.

- **Topological insulators** are phases of matter which exhibit gapless boundary modes that are topologically protected by symmetries. In other words, the material is an ordinary insulator in the bulk, but has a metallic boundary that is very robust and exhibits quantized conductivity.

The robustness of these extended boundary modes is related to the adiabatic evolution of the Hamiltonian, as mentioned earlier. As long as the generic symmetries of the Hamiltonian are preserved and the bulk gap is not closed, the number of edge states corresponds to a topological invariant. This is why these are also called symmetry-protected phases. Topological invariants are used to characterize different phases, and after many individual contributions, the areas of topological band theory and topological field theory were developed taking these concepts into account [31–35].

One striking result of these materials is the bulk-boundary correspondence, which states that the emergence of the edge currents is deeply related to the bulk topology of the system. By studying the material under periodic boundary conditions, one can know how it will behave at the boundary when it has a finite size.

After this general introduction, it is now time to make all these concepts more concrete and comprehend the interplay between symmetries and topological invariants, thus providing a formal classification of the different topological insulators. This will be the aim of the next chapter, but before doing so, we will briefly review in the next section the first discovered topological insulator.

1.3 Integer Quantum Hall Effect

This section is devoted to the Integer Quantum Hall Effect (QHE), which was historically the first discovered topological insulator. In 1879, Edwin Hall observed the classical Hall effect, which can be understood within the Drude model. Its features are a consequence of the Lorentz force acting on charged particles, while moving in a perpendicular magnetic field. Electrons will drift perpendicular to the electric field. Thus, a charge will be accommodated at the sides of the sample, generating a spontaneous electric voltage difference. The ratio between this transverse voltage and the current is known as the Hall resistance, which scales linearly with the magnetic field.

However, in 1980 von Klitzing *et al.* did a similar experiment using a 2D inversion layer or MOSFETs, at temperatures around 1 K and with a high magnetic field (of the order of 10 T) [2]. The result was completely different of what was expected. Instead of a linear dependence, when they measured the transverse (Hall) conductance σ_{xy}, they observed a stepwise dependence on the applied magnetic field, as depicted in figure 1.1. Furthermore, when σ_{xy} exhibited a plateau, the longitudinal conductivity σ_{xx} was zero. Only for some magnetic fields when the Hall conductance was changing, σ_{xx} was non-zero. Hence, dissipationless currents flow along the sample while σ_{xy} is in a plateau. What was even more striking, is that each plateau was quantized in terms of integer values of the fundamental unit of conductance e^2/h, and that the accuracy of the quantization is one part in 10^9. Moreover, the lower the temperatures and the more disordered was the sample, the more accurate was the measurement. Thus, the Integer QHE provided one of the best measurements of the fine structure constant $\alpha = e^2/\hbar c$ (in CGS units), and for this discovery he was awarded the Nobel Prize. To understand this phenomenon, many theoretical efforts were needed. Topology and disorder have been key on understanding this effect, and have opened a new field in condensed matter, known as Topological Insulators.

After describing the effect in general terms, we now follow a reasoning to better understand its features. First, we refer the reader who is not acquainted with the behaviour of electrons moving in a perpendicular magnetic field to appendix A. The energy spectrum of this system is similar to the one of harmonic oscillators, with a gap between Landau levels (LLs) given by the cyclotron frequency energy $\hbar\omega_B$. In the quantum mechanical picture, the current in a 2D system in the presence of a longitudinal eclectic field E and a perpendicular magnetic field

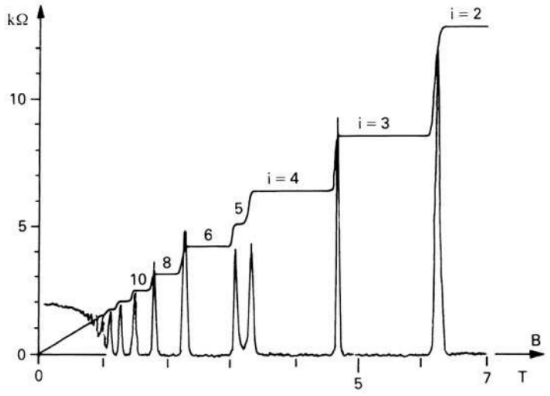

Figure 1.1: Integer QHE. Transverse resistivity as a function of the magnetic field. Peaks correspond to the longitudinal resistivity. This picture has been reproduced from Ref. [36].

$\boldsymbol{B} = (0, 0, B) = \nabla \times \boldsymbol{A}$ is given by

$$\boldsymbol{I} = -\frac{e}{m} \sum_{n=0}^{\nu-1} \sum_{k} \langle \psi_{nk} | - i\hbar\nabla + e\boldsymbol{A} | \psi_{nk} \rangle , \tag{1.2}$$

where m is the electron mass and $\nu \in \mathbb{Z}$ is the filling factor, which express how many Landau levels are completely filled. The current in the x-direction vanishes, as it is just the expectation value of the momentum of a harmonic oscillation, whereas in the y-direction we obtain

$$I_y = -\frac{e}{m} \sum_{n=0}^{\nu-1} \sum_{k} [\langle \hbar k \rangle - \langle eBx \rangle] = e\nu \sum_{k} \frac{E}{B} = \frac{e\mathcal{N}E}{B}\nu = \frac{eEA}{\phi_0}\nu, \tag{1.3}$$

where A is the area of the sample $\mathcal{N}$ is the number of states, and $\phi_0 = h/e$. Here, we used that the expectation value of a harmonic oscillator is $x_0 = -\hbar k + \frac{mE}{eB^2}$, which cancels the first term of the I_y. The quantized Hall resistance, and Hall conductivity then read

$$\rho_{xy} = \frac{V}{I_y} = \frac{\phi_0}{e}\frac{1}{\nu}, \quad \sigma_{xy} = \frac{1}{\rho_{xy}} = \nu\frac{e^2}{h}. \tag{1.4}$$

The above argument shows that whenever ν Landau levels are completely filled, the Hall conductivity is quantized in ν integer units of e^2/h. However, to understand why the plateaus form, we need to introduce disorder. Hence, let us introduce impurities to the system, and model them as a random potential $V(x)$. We can treat this potential perturbatively, as long as $V \ll \hbar\omega_B$. The disorder will have two effects. Firstly, the Landau levels will become broader (without overlapping), as each delta distribution will be replaced by a Lorentzian, lifting the degeneracy and conserving the total number of electrons in the band. Secondly, if the fluctuation of the potential is not appreciable in the magnetic length scale l_m, $|\nabla V| \ll \hbar\omega_B/l_m$, quantum states will become localized [37], as they will be trapped close to the extrema, with a cyclotron orbit along equipotential lines. Hence, disorder will open a mobility edge, corresponding to states that are centered at the band. The states located at the opposite edges of the sample are the only ones that will be extended, thus carrying the current. They have opposite chiriality, as one can see by computing the drift velocity v_y, which has opposite signs. Hence, an electron would need to cross the whole material to scatter with another electron, which is energetically unfavourable. Having no scattering processes is consistent with a zero longitudinal resistivity, and this is why these states are so robust to impurities. Away from the mobility edge, the states will become localized, and therefore they will not contribute to the Hall conductivity.

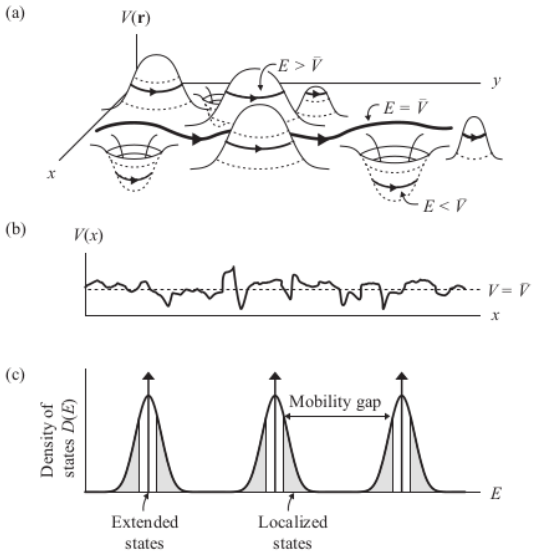

Figure 1.2: (a) Potential landscape in a two-dimensional sample with orbits of electrons. (b) Variation of the potential along a constant y coordinate. (c) Density of states for the Landau levels when disorder is introduced.

With the effect of disorder, we can now explain why the plateaus are formed. First, let us fix the density of electrons n_e in the system. If we decrease the magnetic field, the available states at each band will decrease (recall equation (A.10)). Hence, electrons will begin to populate the next Landau level. However, as long as we do not cross the mobility edge of the given Landau level, the conductivity will remain constant, as all these states will remain localized. Thus, the resistivity will be in a plateau. When the mobility edge is crossed, extended states will begin to be populated and hence, the conductivity will increase. Therefore, as long as the Fermi energy is in the mobility gap, the conductivity will remain in a plateau.

Although disorder seems to perfectly explain why we see these steps, the statement used for showing the quantization of the Hall conductance breaks down when we consider systems which are not translationally invariant. Even more important, it cannot predict the quantization of the Hall conductance in rational numbers that happens in the Fractional QHE [38]. Moreover, why is the quantization so accurate? In 1982, Thouless, Kohmoto, Nightingale, and den Nijs (TKNN) found out that there is a much deeper reasoning for all that, and they where able to identify σ_{xy} with a topological invariant [39].

1.3.1 The Adiabatic Theorem

To obtain this relationship let us consider a physical system described by a general Hamiltonian $H(\boldsymbol{\lambda})$ subjected to a set of parameters $\boldsymbol{\lambda} = (\lambda_1, \lambda_2, ...)$, which could be an electric field, a magnetic field, a flux, etc., evolving smoothly in time, i.e. $\lambda_i = \lambda_i(t)$. Let $\{|n(\boldsymbol{\lambda})\rangle\}_0^N$ be a complete orthonormal set,

$$\langle n|m\rangle = \delta_{nm}, \quad \sum_{n=1}^{N} |n\rangle \langle n| = \mathbb{I},$$

of instantaneous eigenstates of the time-dependent Schrödinger equation with a discrete energy spectrum and no degeneracies. Hence,

$$\hat{H}(\boldsymbol{\lambda}) |n(\boldsymbol{\lambda})\rangle = E_n(\boldsymbol{\lambda}) |n(\boldsymbol{\lambda})\rangle , \tag{1.5}$$

and $E_1 < E_2 < ... < E_N$. Then, under the assumption that the variation is slow, if we prepare an initial pure state, the adiabatic theorem states that after the time evolution, the final state will remain in the same instantaneous eigenstate, up to a phase,

$$|\Psi(0)\rangle = |n(\boldsymbol{\lambda}(0))\rangle\,,$$
$$|\Psi(\boldsymbol{\lambda}(t))\rangle = e^{i\alpha_n(t)}\,|n(\boldsymbol{\lambda}(t))\rangle\,.$$

We can see this by solving the differential equation that one obtains from the Schrödinger equation,

$$\hat{H}(t)\,|\Psi(t)\rangle = i\hbar\frac{\partial}{\partial t}\,|\Psi(t)\rangle\,. \tag{1.6}$$

From now on, we will drop the explicit dependence of the Hamiltonian, states, and energy with the parameters $\boldsymbol{\lambda}$, and will write only the time. However, keep in mind that the time always enters through the parameters $\boldsymbol{\lambda} = \boldsymbol{\lambda}(t)$ and thus, any time derivative can be regarded as $\partial_t = \dot{\boldsymbol{\lambda}}\nabla_\lambda$.

Suppose that after varying the parameters, the final state at time t is in a linear combination of the instantaneous eigenstates

$$|\Psi(t)\rangle = \sum_n c_n(t)\,|n(t)\rangle\,.$$

This state must fulfill the Schrödinger equation (1.6), which leads to the following equality

$$\sum_n E_n(t)c_n(t)\,|n(t)\rangle = i\hbar\sum_n\big[\dot{c}_n(t)\,|n(t)\rangle + c_n(t)\,|\dot{n}(t)\rangle\big].$$

By multiplying with $\langle m(t)|$ from the left

$$\begin{aligned} E_m c_m(t) &= i\hbar\big[\dot{c}_m(t) + \sum_n \langle m(t)|\,c_n(t)\,|\dot{n}(t)\rangle\big] \\ &= i\hbar\big[\dot{c}_m(t) + c_m(t)\,\langle m(t)|\dot{m}(t)\rangle\big] + i\hbar\sum_{n\neq m} c_n(t)\,\langle m(t)|\dot{n}(t)\rangle\,, \end{aligned}$$

and if we rearrange it, we obtain a first order linear differential equation:

$$\dot{c}_m(t) + \frac{i}{\hbar}\Big[E_m(t) - i\hbar\,\langle m(t)|\dot{m}(t)\rangle\Big]c_m = -\sum_{n\neq m} c_n(t)\,\langle m(t)|\dot{n}(t)\rangle\,. \tag{1.7}$$

The assumption of the adiabatic theorem considers that the transition amplitude between states along the smooth evolution of the parameters $\boldsymbol{\lambda}$ through time is highly suppressed and thus, the term at the r.h.s. vanishes. Integrating the homogeneous equation gives

$$c_m(t) = c_m(0)\,\exp\!\left\{\frac{-i}{\hbar}\int_0^t\big[E_m(t') - i\hbar\,\langle m(t')|\dot{m}(t')\rangle\big]\,\mathrm{d}t'\right\},$$

and hence, as long as the above approximation holds, the final state will be given by

$$|\Psi(t)\rangle = \sum_n c_n(0)e^{i\theta_n(t)}e^{i\gamma_n(t)}\,|n(t)\rangle\,, \tag{1.8}$$

which is the claim of the adiabatic theorem.

1.3.2 The Berry Phase

The first function defined

$$\theta_n(t) = -\frac{1}{\hbar}\int_0^t E_n(t')\,\mathrm{d}t'$$

is the usual dynamical factor of the energy correspondent to the eigenstate. The second one is of great importance, as encodes the geometry of the manifold where the parameters fluctuate. It is also known as Berry phase due to its discovery in 1984 [40],

$$\gamma_n(t) = \int_0^t i \langle n(t')| \nabla_{\boldsymbol{\lambda}} |n(t')\rangle \dot{\lambda} \, \mathrm{d}t' = \int_{\mathcal{C}} i \langle n(\boldsymbol{\lambda})| \nabla_{\boldsymbol{\lambda}} |n(\boldsymbol{\lambda})\rangle \, \mathrm{d}\boldsymbol{\lambda}. \tag{1.9}$$

In analogy to electromagnetism, we can define a gauge dependent vector potential called Berry connection,

$$\boldsymbol{\mathcal{A}}^n(\boldsymbol{\lambda}) = i \langle n(\boldsymbol{\lambda})| \nabla_{\boldsymbol{\lambda}} |n(\boldsymbol{\lambda})\rangle . \tag{1.10}$$

If we rewrite Eq.(1.9) in terms of this vector field and the path through the parameter space is closed, we can use Stokes' theorem to reexpress the Berry phase as the flux of a "magnetic field" through a surface enclosed by the path $\mathcal{C}$

$$\gamma(\mathcal{C}) = \oint_{\mathcal{C}} \boldsymbol{\mathcal{A}}^n \cdot \mathrm{d}\boldsymbol{\lambda} = \int_{\mathcal{S}(\mathcal{C})} (\nabla \times \boldsymbol{\mathcal{A}}^n) \cdot \mathrm{d}\boldsymbol{S}. \tag{1.11}$$

In addition, an anti-symmetric field strength called Berry curvature can also be defined. It is is gauge invariant, and is known as curvature of the connection,

$$\mathcal{F}^n_{ij} = \partial_{\lambda_i} \mathcal{A}_j - \partial_{\lambda_j} \mathcal{A}_i. \tag{1.12}$$

Writing all this together, one obtains that the Berry phase is given by

$$\gamma(\mathcal{C}) = \int_{\mathcal{S}(\mathcal{C})} \mathcal{F}^n_{ij} \frac{1}{2} \epsilon^{ijk} \, \mathrm{d}\boldsymbol{S}^k = \int_{\mathcal{S}(\mathcal{C})} \mathcal{F}^n_{ij} \, \mathrm{d}\boldsymbol{S}^{ij}. \tag{1.13}$$

1.3.3 Kubo Formula and the TKNN invariant

If a system is in an instantaneous eigenstate $|n\rangle$, then the perturbed state after time t, to first order in the time derivative, will be

$$|\psi_n\rangle = e^{i\theta_n(t)} \left[|n\rangle + i\hbar \sum_{m \neq n} \frac{\langle m|\dot{n}\rangle}{E_m - E_n} |m\rangle \right]. \tag{1.14}$$

The value $\langle m(t)|\dot{n}(t)\rangle$ can be rewritten in terms of the $\dot{\hat{H}}$ by noticing that if we differentiate the eigenvalue equation (1.5) and multiply it from the left by $\langle m|$, we get

$$\langle m| \dot{\hat{H}} |n\rangle + \langle m| H |\dot{n}\rangle = \langle m| \dot{E}_n |n\rangle + \langle m| E_n |\dot{n}\rangle ,$$

$$\text{hence} \quad \langle m|\dot{n}\rangle = \frac{\langle m| \dot{\hat{H}} |n\rangle}{E_n - E_m}.$$

Let assume that the state (1.8) is in a uniform magnetic field $\boldsymbol{B}$, and it can interact with a slowly varying electric field. In the Weyl gauge $A_0 = 0$, the time dependent parametrization enters through $\delta \boldsymbol{A} = \boldsymbol{E}t$. Our interest is to compute the conductivity, which is the response function of the current to the gauge potential, i.e. the response of the system under the influence of the applied electric field. From the standard path integral approach, we know that the currents are defined as functional derivatives,

$$J_\mu = \frac{\delta H}{\delta A_\mu}, \quad \text{hence} \quad \dot{H} = J_j E_j,$$

as time enters into H through the space components of the vector potential. Since the transverse conductivity tensor can be obtained by the average value of the current,

$$\langle J_k \rangle_{xy} = \sigma_{xy} \epsilon_{kl} E_l, \tag{1.15}$$

we can compute the expectation value of the current operator J_k in the state (1.8) to obtain the above relation with the conductivity. These lead to the expression known as Kubo formula

$$\sigma_{xy} = \frac{\langle J_x \rangle_{xy}}{E_y} = -i\hbar L_x L_y \sum_{m \neq n} \frac{\langle n| J_x |m\rangle \langle m| J_y |n\rangle - \langle n| J_y |m\rangle \langle m| J_x |n\rangle}{(E_m - E_n)^2}, \tag{1.16}$$

where we introduced the sample dimension area $L_x L_y$.

To connect this to a topological invariant, we must discretize the sample. The spectrum then will form bands, and the wavefunctions of the electrons will be in Bloch form, with a lattice momentum $\boldsymbol{k}$, that lives in a torus T^2. The current density element is given by

$$\mathrm{d}J_i = e v_i \mathrm{d}\rho = e \frac{1}{\hbar} \frac{\partial H(\boldsymbol{k})}{\partial k_i} \frac{\mathrm{d}^2 k}{(2\pi)^2}. \tag{1.17}$$

where the density element of states is $\mathrm{d}\rho = \mathrm{d}^2 k/(2\pi)^2$, and $\boldsymbol{v} = \nabla_{\boldsymbol{k}} H(\boldsymbol{k})$ is the group velocity. Thus, if we substitute this into the Kubo formula (1.16) and integrate over the whole Brillouin zone, it follows that

$$\sigma_{xy} = \frac{ie^2}{\hbar} \int \frac{\mathrm{d}^2 k}{(2\pi)^2} \int \frac{\mathrm{d}^2 k'}{(2\pi)^2} \sum_{E_n < E_F < E_m} \frac{\langle n| \partial_{k_y} H(\boldsymbol{k}) |m\rangle \langle m| \partial_{k_x} H(\boldsymbol{k}) |n\rangle - \langle n| \partial_{k_x} H(\boldsymbol{k}) |m\rangle \langle m| \partial_{k_y} H(\boldsymbol{k}) |n\rangle}{(E_m - E_n)^2}. \tag{1.18}$$

Now, the eigenstates $|n(\boldsymbol{k})\rangle$ ($|m(\boldsymbol{k'})\rangle$) are the single particle non-interacting states of the nth (mth) Landau level below (above) the Fermi energy, which completely fill the first Brillouin zone. Hence, it sums pairs of states from below and above the Fermi energy. Rewriting the numerator as

$$\langle n| \partial_{k_y} H(\boldsymbol{k}) |m\rangle = \langle n| \partial_{k_y} \Big(H(\boldsymbol{k}) |m\rangle \Big) - \langle n| H(\boldsymbol{k}) \partial_{k_y} |m\rangle = -\Big(E_m(\boldsymbol{k'}) - E_n(\boldsymbol{k}) \Big) \langle \partial_{k_y} n | m\rangle ,$$

and using the completeness relation

$$\int \frac{\mathrm{d}^2 k'}{(2\pi)^2} \sum_{E_n < E_F < E_m} \langle \partial_{k_y} n | m\rangle \langle m | \partial_{k_x} n\rangle = \int \frac{\mathrm{d}^2 k}{(2\pi)^2} \sum_n \langle \partial_{k_y} n| \left(\mathbb{I} - |n\rangle \langle n| \right) |\partial_{k_x} n\rangle ,$$

the transverse conductivity is reexpressed as

$$\sigma_{xy} = \frac{ie^2}{\hbar} \int \frac{\mathrm{d}^2 k}{(2\pi)^2} \sum_n \Big(\langle \partial_{k_y} n | \partial_{k_x} n\rangle - \langle \partial_{k_x} n | \partial_{k_y} n\rangle \Big). \tag{1.19}$$

At this point, we can identify the Berry connection $\boldsymbol{\mathcal{A}}^n(\boldsymbol{k}) = i \langle n| \frac{\partial}{\partial \boldsymbol{k}} |n\rangle$ and the Berry curvature $F_{ij}(\boldsymbol{k}) = \frac{\partial \mathcal{A}_j^n}{\partial k_i} - \frac{\partial \mathcal{A}_i^n}{\partial k_j}$, which allow us to rewrite the Hall conductivity in terms of the first Chern number.

$$\sigma_{xy} = \frac{e^2}{\hbar} \sum_n \int \frac{\mathrm{d}^2 k}{(2\pi)^2} F_{xy} = \frac{e^2}{h} \sum_n C_n = \frac{e^2}{h} C. \tag{1.20}$$

This is the conductivity of a band insulator, and is purely topological. As long as the Fermi energy lies in the gap, the Hall conductivity is going to be quantized by an integer, which is a sum of the first Chern numbers C_n, one for each n filled band. This can explain as well its robustness, as the Chern number cannot change if the gap is not closed. The nature of the Integer QHE is thus topological.

The role of gauge invariance can be used to see how each Landau level contributes to the edge current. The argument depends on the geometry, but the physics should not depend on it. The set-up is the same as before, but now electrons moves in the annulus, also called *Corbino ring*, and there is also a flux ϕ through the hole. Following the Laughlin argument, when the flux changes adiabatically exactly by one quantum flux $\Delta\phi = \phi_0$, the states increase their angular momentum by $\hbar$ and are mapped onto themselves, moving outwards $r_m \to r_{m+1}$ with m the quantum number for the angular momentum. As the number of electrons stays invariant through the process, if ν Landau levels are filled, each must exactly contribute with one electron to the Hall conductivity.

Now that we understood the origin of conductivity quantization in the integer QHE, we will delve into symmetries to look for a more general underlying principle behind the topological features.

Chapter 2

Symmetries

Symmetry has always been a powerful tool to characterize a system. Already in classical mechanics we encounter that a system invariant over time translations conserves energy, and invariance over spatial translations is associated with momentum conservation. Emmy Noether cast all this together, proving an important theorem in classical field theory [41]. Noether's theorem states that a symmetry will have an associated conserved current, thus connecting symmetries with conservation laws. In other areas of physics, symmetry is also important. As mentioned before, Bloch theorem enables us to classify materials in terms of the band structure; the phenomenological Ginzburg-Landau theory, classifies the different phases of matter in terms of a symmetric or a symmetry-broken state.

To classify topological matter, however, we need to drive our attention to discrete symmetries that appear in condensed matter, mainly the ones that have an anti-unitary nature [42]. At the end of the chapter, we will see that one can establish a systematic classification scheme, the so-called tenfold way, which predicts when matter will be in a topological or trivial phase, depending on the presence or absence of symmetries. This classification is an an extension of the threefold way of Wigner-Dyson's random matrix ensemble classification [43–45]. The first ones who realized this were Altland and Zirnbauer; hence the classification is referred to as the Altland-Zirnbauer (AZ) symmetry classes [7, 46]. The chapter is based in some recent works [47–50] that provide a more pedagogical account for the AZ classification. For a different approach based on K-theory, we refer the reader to the work of Kitaev [51].

To begin with, let us recall what we understand by a symmetry in quantum mechanics. Wigner theorem states that any invertible operator $\mathcal{U}$, which preserves the transition amplitude between any two single-particle states,

$$|\langle\alpha|\beta\rangle|^2 = \left|\langle\alpha\mathcal{U}^\dagger|\mathcal{U}\beta\rangle\right|^2 = |\langle\alpha'|\beta'\rangle|^2,$$

is a symmetry. $\mathcal{U}$ will be either unitary or anti-unitary, which is also referred as linear or anti-linear [52]. Thus, we have

$$\begin{aligned}\mathcal{U}(i\mathbb{I})\mathcal{U}^{-1} &= i\mathbb{I}, \quad \text{linear},\\ \mathcal{U}(i\mathbb{I})\mathcal{U}^{-1} &= -i\mathbb{I}, \quad \text{anti-linear}.\end{aligned}$$

Within the second quantization formalism, the Hamiltonian of a non-interacting system of fermions is given by

$$\hat{\mathcal{H}} = \sum_{ij} \hat{\psi_i^\dagger} H_{ij} \hat{\psi_j}, \tag{2.1}$$

with $\hat{\psi_i^\dagger}$ and $\hat{\psi_j}$ the second-quantized creation and annihilation operators, respectively, which satisfy the anticommutation relation $\{\psi_j, \psi_i^\dagger\} = \delta_{ij}$, and H_{ij} the single-particle Hamiltonian.

To simplify the notation, we can imagine the system discretized in a lattice, and the index i can be considered as an array involving different degrees of freedom, e.g., spin, orbital, lattice position, sublattice, etc. Then, we say that the operator $\hat{\mathcal{U}}$ is a symmetry if the second-quantized Hamiltonian commutes with it,

$$[\hat{\mathcal{U}}, \hat{\mathcal{H}}] = 0.$$

2.1 Time-Reversal Symmetry

This discrete symmetry reverses the flow of time, $T : t \to t$. Therefore, it must commute with any spatial symmetry, and invert operators that are proportional to odd time derivative

$$T\hat{x}T^{-1} = \hat{x}, \quad T\hat{p}T^{-1} = -\hat{p} \tag{2.2}$$

Notice that as the canonical commutation relation for $\hat{x}$ and $\hat{p}$ must hold,

$$T[\hat{x}_i, \hat{p}_j]T^{-1} = Ti\hbar\delta_{ij}T^{-1} = -[\hat{x}_i, \hat{p}_j] = -i\hbar\delta_{ij} \Rightarrow TiT^{-1} = -i. \tag{2.3}$$

Time-Reversal (TR) symmetry needs to change $i \to -i$. In second quantization, the TR operator acts on the creation and annihilation operators as

$$\hat{\mathcal{T}}\hat{\psi}_i\hat{\mathcal{T}}^{-1} = \sum_j (U_T^\dagger)_{ij}\hat{\psi}_j, \quad \hat{\mathcal{T}}\hat{\psi}^\dagger{}_i\hat{\mathcal{T}}^{-1} = \sum_j \hat{\psi}_j^\dagger (U_T)_{ji}, \tag{2.4}$$

with U_T a unitary matrix. Constraining the second-quantized Hamiltonian $\hat{\mathcal{H}}$ to be symmetric, we get for the single-particle Hamiltonian

$$U_T H^* U_T^{-1} = +H. \tag{2.5}$$

Defining the *anti-linear* complex conjugation operator K as

$$KAK^{-1} = A^*, \tag{2.6}$$

we can write the first-quantized TR operator as $T = U_T K$. Applying twice the operator, $T^2 = U_T K U_T K = U_T (U_T^T)^{-1} = \phi$, we obtain a diagonal matrix of phases that gives a constraint for the unitary matrix $U_T = \phi U_T \phi$, as $U_T = \phi U_T^T$, and $U_T^T = U_T \phi$. This can only be fulfilled if $\phi = \pm 1$.

For spinless particles in the position representation, the degrees of freedom are just the position and momentum operators. They transform as equation (2.2), but we can see that as the non-vanishing components of the momentum are purely imaginary, then $U_T \hat{p} U_T = \hat{p}$ (as). Thus, the matrix phases must be the identity with $\phi = 1$.

When particles have spin $\boldsymbol{S}$, the TR operator will flip the sign since it is an angular momentum. Thus, $T\boldsymbol{S}T^{-1} = -\boldsymbol{S}$. A change of sign can be implemented by a unitary U_T rotation of π around, i.e., the y-axis. Then, we write TR as

$$T = e^{-i\pi S_y} K. \tag{2.7}$$

If we now square this operator, we implement a rotation of 2π,

$$T^2 = e^{-i\pi S_y} K e^{-i\pi S_y} K = e^{-i\pi S_y} e^{i\pi S_y^*} = e^{-i2\pi S_y}. \tag{2.8}$$

Hence, for half-integer spin particles gives a factor of -1, but for integer spin, it gives the identity. This has a deep consequence for TR-invariant systems, the so called Kramer's theorem, which states that every energy mode of a TR invariant system with an odd number of spin-half particles is at least doubly degenerated [53].

We can prove this by first observing that if the single-particle state $|\psi\rangle$ is an eigenstate with eigenenergy ϵ, it must exist a TR partner with the same energy: $HT|\psi\rangle = TH|\psi\rangle = T\epsilon|\psi\rangle = |\psi\rangle$, as $[H,T]=0$. What we have left is to show that they are orthogonal. Thus,

$$\begin{aligned}\langle\psi|T\psi\rangle &= \sum_{m,n}\psi_m^*(U_T)_{mn}K\psi_n = \sum_{m,n}\psi_m^*(U_T)_{mn}\psi_n^* \\ &= \sum_{m,n}\psi_n^*(U_T)_{mn}\psi_m^* = \sum_{m,n}\psi_n^*(-1)(U_T)_{nm}K\psi_m = -\langle\psi|T\psi\rangle = 0.\end{aligned} \tag{2.9}$$

As we see, it is crucial to have $T^2=-1$, as this implies that the unitary matrix is antisymmetric, $U=-U^T$, and gives the required minus sign. Otherwise, we would not have any degeneracy. This statement only works for a state $|\psi\rangle = |\psi_1\rangle\otimes\cdots\otimes|\psi_N\rangle$ with N odd, as $T^2=(-1)^N\mathbb{I}^{\otimes N}$ acts in the Hilbert space of each particle. This implies that the scattering process between Kramer's pairs of states with an odd number of particles is forbidden, while for an even number it does not vanish.

Before ending this section, we can consider how the TR operator behaves in fermionic systems that have translation symmetry. We know from Bloch theorem that in this case, the momentum $\boldsymbol{k}$ it is going to be a good quantum number for indexing states. Thus, in Fourier space the Hamiltonian is given by

$$H = \sum_k c^\dagger_{\boldsymbol{k}\alpha\sigma}h^{\sigma\sigma'}_{\alpha\beta}(\boldsymbol{k})c_{\boldsymbol{k}\beta\sigma'}, \tag{2.10}$$

with $c^\dagger_{\boldsymbol{k}\alpha\sigma}$ and $c_{\boldsymbol{k}\beta\sigma'}$ the creation and annihilation operators of an electron with momentum $\boldsymbol{k}$, with α,β orbital indices and σ,σ' spin indices. To obtain how it transforms, one first needs to determine how TR acts on creation and annihilation operators. Using again the Pauli matrix to represent the spin rotation over the y-axis implemented by the TR operator and writing the Fourier transformation, we get

$$Tc^\dagger_{\boldsymbol{k}\alpha\sigma}T^{-1} = c^\dagger_{-\boldsymbol{k}\alpha\sigma'}i(\sigma^y)^T_{\sigma'\sigma} \quad\text{and}\quad Tc_{\boldsymbol{k}\alpha\sigma}T^{-1} = i\sigma^y_{\sigma\sigma'}c^\dagger_{-\boldsymbol{k}\alpha\sigma'}. \tag{2.11}$$

When TR is a symmetry of the Hamiltonian H, the Bloch Hamiltonian will transform as

$$\begin{aligned}THT^{-1} &= T\sum_{\boldsymbol{k}}c^\dagger_{\boldsymbol{k}\alpha\sigma}h^{\sigma\sigma'}_{\alpha\beta}(\boldsymbol{k})c_{\boldsymbol{k}\beta\sigma'}T^{-1} = \sum_k c^\dagger_{-\boldsymbol{k}\alpha\sigma''}i(\sigma^y)^T_{\sigma''\sigma}Th^{\sigma\sigma'}_{\alpha\beta}(\boldsymbol{k})T^{-1}i\sigma^y_{\sigma'\sigma'''}c^\dagger_{-\boldsymbol{k}\beta\sigma''''} \\ &= \sum_k c^\dagger_{\boldsymbol{k}\alpha\sigma''}i(\sigma^y)^T_{\sigma''\sigma}(h^{\sigma\sigma'}_{\alpha\beta}(-\boldsymbol{k}))^*i\sigma^y_{\sigma'\sigma'''}c^\dagger_{\boldsymbol{k}\beta\sigma''''} = \sum_k c^\dagger_{\boldsymbol{k}\alpha\sigma''}h^{\sigma''\sigma''''}_{\alpha\beta}(\boldsymbol{k})c^\dagger_{\boldsymbol{k}\beta\sigma''''} = H.\end{aligned}$$

We used that the Bloch Hamiltonian, $h^{\sigma\sigma'}_{\alpha\beta}(\boldsymbol{k})$, is a number, which implies complex conjugation under TR. The momentum has also been relabelled, and the matrix product has been defined as the transformed Bloch Hamiltonian. Dropping out the indices, this would reads as

$$Th(\boldsymbol{k})T^{-1} = h(-\boldsymbol{k}). \tag{2.12}$$

A similar argument of what we used to show Kramer's degeneracy can be done here. However, in momentum space Kramer's pairs are split in states with momentum $\boldsymbol{k}$ and $-\boldsymbol{k}$. A state $|\alpha_{\boldsymbol{k}}\rangle$ with energy $\epsilon_{\boldsymbol{k}}$ has a TR partner $T|\alpha_{\boldsymbol{k}}\rangle$ that is proper of the TR Bloch Hamiltonian $h(-\boldsymbol{k})$, with energy $\epsilon_{-\boldsymbol{k}}=\epsilon_{\boldsymbol{k}}$. Hence, we will only have Kramer's degeneracy at TR-invariant points, where $\boldsymbol{k}=-\boldsymbol{k}$.

2.2 Particle-Hole Symmetry

In second quantization, a particle-hole (PH) transformation $\hat{C}$ is a unitary operator that exchanges the fermionic creation and annihilation operators. Hence, a Fock space with p fermions and q holes is mapped to a Fock space with q fermions and p holes,

$$\hat{\mathcal{C}} : \mathcal{F}^{p,q} \to \mathcal{F}^{q,p}. \tag{2.13}$$

It is also referred to as charge conjugation, as one can see that for particle conserving systems it flips the charge, which is the difference between fermions and holes. Its action onto the second-quantized creation and annihilation operators can be written as

$$\hat{\mathcal{C}}\hat{\psi}_i\hat{\mathcal{C}}^{-1} = \sum_j (U_C^{*\dagger})_{ij}\hat{\psi}_j^\dagger, \quad \hat{\mathcal{C}}\hat{\psi}^\dagger{}_i\hat{\mathcal{C}}^{-1} = \sum_j \hat{\psi}_j (U_C^*)_{ji}, \quad \hat{\mathcal{C}}i\hat{\mathcal{C}}^{-1} = +i. \tag{2.14}$$

Again, if PH transformation is a symmetry of the second-quantized Hamiltonian $\hat{\mathcal{H}}$, they must commute, which implies that the first-quantized Hamiltonian satisfies

$$U_C H^* U_C^\dagger = -H. \tag{2.15}$$

If C anticommutes with the single-particle Hamiltonian, its square C^2 will commute. As before, by Schur's lemma it will be a multiple of the identity matrix, i.e. $C^2 = e^{i\phi}\mathbb{I}$, and consequently $C^2 = \pm 1$.
Observe that by using the complex conjugation operator K defined at equation (2.6), we can write the PH transformation acting on the single-particle Hilbert space as an *anti-unitary* operator $C = U_C K$. Then, for every system that has a PH symmetry, if it has an eigenstate $|\alpha\rangle$ with eigenvalue ϵ, it will have a PH-symmetric partner $C|\alpha\rangle$ with energy $-\epsilon$, as can be easily verified using equation (2.15),

$$HC|\alpha\rangle = HU_C(|\alpha\rangle)^* = -U_C(H|\alpha\rangle)^* = -U_C K\epsilon|\alpha\rangle = -\epsilon C|\alpha\rangle.$$

2.3 Chiral Symmetry

The last important discrete symmetry that we need to discus to classify topological insulators is the chiral symmetry. It can be defined as a combination between TR and PH symmetries,

$$\hat{\mathcal{S}} = \hat{\mathcal{T}} \cdot \hat{\mathcal{C}}. \tag{2.16}$$

Using equations (2.4) and (2.14), we can see how the fermionic operators transform under this symmetry

$$\hat{\mathcal{S}}\hat{\psi}_i\hat{\mathcal{S}}^{-1} = \sum_j (U_S^{*\dagger})_{ij}\hat{\psi}_j^\dagger, \quad \hat{\mathcal{S}}\hat{\psi}^\dagger{}_i\hat{\mathcal{S}}^{-1} = \sum_j \hat{\psi}_j (U_S^*)_{ji}, \quad \hat{\mathcal{S}}i\hat{\mathcal{S}}^{-1} = -i, \tag{2.17}$$

with $U_S = U_T U_C^*$. Observe that the first-quantized chiral symmetry $S = U_S$ is *unitary*. Now, to be a symmetry of the second-quantized Hamiltonian, we know that they must commute, which implies that the first-quantized Hamiltonian transforms as

$$U_S H U_S^\dagger = -H. \tag{2.18}$$

The same reasoning applies for the square of the chiral symmetry. However, as $U_S = U_T U_C^*$, we can pick an appropriate basis such that the arbitrary phases from TR and PH cancel out. Thus, $S^2 = \mathbb{I}$. The anticommutation relation $\{H, U_S\} = 0$ leads to a symmetric spectrum, since for any eigenvalue equation $H|\alpha\rangle = \epsilon|\alpha\rangle$, we will also have another one which is related by chiral symmetry as $HU_S|\alpha\rangle = -U_S H|\alpha\rangle = -\epsilon U_S|\alpha\rangle$.

Chiral symmetry is also referred to as a sublattice symmetry. To understand why, we can

use as an example a lattice where there are sublattices A and B. The first-quantized Hamiltonian would be given by a hopping with the same sublattice on the diagonal (a on-site potential), and off-diagonal terms encoding the hopping between sublattices. Similarly as before, one can see that the possible eigenvalues of the matrix U_S are ± 1. Thus, if there is a chiral symmetry, the following equations must hold

$$HU_S = \begin{pmatrix} H_{AA} & H_{AB} \\ H_{AB}^\dagger & H_{BB} \end{pmatrix} \begin{pmatrix} 1 & 0 \\ 0 & -1 \end{pmatrix} = \begin{pmatrix} H_{AA} & -H_{AB} \\ H_{AB}^\dagger & -H_{BB} \end{pmatrix} = \begin{pmatrix} -H_{AA} & -H_{AB} \\ H_{AB}^\dagger & H_{BB} \end{pmatrix} = -U_S H.$$

Therefore, the only possibility left is that when U_S is in diagonal form, the single-particle Hamiltonian H must be in block-off-diagonal form

$$H = \begin{pmatrix} 0 & H_{AB} \\ H_{AB}^\dagger & 0 \end{pmatrix}.$$

2.4 Tenfold way

At the beginning of the chapter, we anticipated that topological insulators can be classified in terms of three discrete symmetries. In first quantization, the only anti-unitary symmetries that exist are time reversal T and particle-hole C symmetries. However, we also said that we needed to consider their product, which is the unitary chiral symmetry S. Then, one could ask: Why are these anti-unitary symmetries so important in classifying the topological phases of matter? Why are we only considering one unitary symmetry, which is also related to their product? In this section, we will motivate and discuss these answers, presenting the tenfold way, which is a complete classification scheme for non-interacting fermions.

If one is interested in classifying all non-interacting topological insulators, one can address this by studying how the single-particle first-quantized Hamiltonian H is constrained under symmetry transformations. Recall that symmetries will commute with the second quantized Hamiltonian $\hat{\mathcal{H}}$, and preserve the probability under time evolution $U(t) = e^{-itH/\hbar}$ operator. There are only two options for constraining the Hamiltonian, since a linear representation of a quantum mechanical symmetry is either unitary or anti-unitary. It turns out that if one classifies topological phases which are protected by unitary symmetries, the result is not universal, but rather relies on the nature of the unitary symmetries that constrain the Hamiltonian. Therefore, the anti-unitary symmetries are responsible for protecting the topological phases.

To study the set of all possible forms of Hamiltonians, first one removes the unitary symmetries. If G_0 is a group of symmetries, where its elements $g \in G_0$ have a linear representation of unitary matrices U_g that are a symmetry of the first-quantized Hamiltonian, then we can always choose a basis in which the representation of the first-quantized Hamiltonian is reduced to a block-diagonal form H^λ. Each block is related to an irreducible representation λ of G_0, that decomposes the vector space of single-particle states as a direct sum $V = \bigoplus_\lambda V_\lambda$. The form of all possible blocks H^λ is independent of the symmetry group G_0. Therefore, they must be related to the other possibility, which are the anti-unitary symmetries [49, 54]. However, we mentioned that it is also necessary to include chiral symmetry, even though it is unitary in first quantization. This happens because the unitary symmetries that reduce the single-particle Hamiltonian to a block-diagonal form commute with H. Therefore, chiral symmetry $S = U_S$, which anticommutes, is not included.

The set of all possible blocks of H^λ are given by the presence or absence of these three discrete symmetries. As we saw in the previous sections, the square of TR and PH operators can be ± 1. Adding the option to not be invariant under these symmetries, there is 3 possibilities for each, which gives $3 \times 3 = 9$ different ways of transforming the Hamiltonian H^λ under these symmetries. For 8 out of these 9 possibilities, the presence or absence of chiral symmetry is already fixed. It is when TR and PH are not present that we can still have (or not) a chiral

Cartan	T	C	S	Time evolution operator $U(t) = e^{itH}$	Anderson Localization NLσM Manifold G/H
A (unitary)	0	0	0	$\mathrm{U}(N)$	$\mathrm{U}(2n)/\mathrm{U}(n)\times\mathrm{U}(n)$
AI (orthogonal)	+1	0	0	$\mathrm{U}(N)/\mathrm{O}(N)$	$\mathrm{Sp}(4n)/\mathrm{Sp}(2n)\times\mathrm{Sp}(2n)$
AII (symplectic)	−1	0	0	$\mathrm{U}(2N)/\mathrm{Sp}(2N)$	$\mathrm{SO}(2n)/\mathrm{SO}(n)\times\mathrm{SO}(n)$
AIII (ch. unitary)	0	0	1	$\mathrm{U}(N+M)/\mathrm{U}(N)\times\mathrm{U}(M)$	$\mathrm{U}(n)$
BDI (ch. orth.)	+1	+1	1	$\mathrm{SO}(N+M)/\mathrm{SO}(N)\times\mathrm{SO}(M)$	$\mathrm{U}(2n)/\mathrm{Sp}(2n)$
CII (ch. sympl.)	−1	−1	1	$\mathrm{Sp}(2N+2M)/\mathrm{Sp}(2N)\times\mathrm{Sp}(2M)$	$\mathrm{U}(n)/\mathrm{O}(n)$
D	0	+1	0	$\mathrm{O}(N)$	$\mathrm{O}(2n)/\mathrm{U}(n)$
C	0	−1	0	$\mathrm{Sp}(2N)$	$\mathrm{Sp}(2n)/\mathrm{U}(n)$
DIII	−1	+1	1	$\mathrm{O}(2N)/\mathrm{U}(N)$	$\mathrm{O}(n)$
CI	+1	−1	1	$\mathrm{Sp}(2N)/\mathrm{U}(N)$	$\mathrm{Sp}(2n)$

Table 2.1: Tenfold classification of symmetry classes. The first column are the Cartan's label. The T column corresponds to TR symmetry, when commutes with the first quantized Hamiltonian appears a $+1$ or a -1 depending on the value of T^2. If it is 0, the symmetry is not present, hence anticommutes with H. Same applies for PH symmetry C. For Chiral symmetry S, 1 when anticommutes with H, 0 when does not anticommute (when is present or not, respectively). The last column represents the symmetric spaces where the NLσM field theory, describing the boundary, lives. Note that are the same elements of the column before, but permuted. This table has been reproduced from [49].

symmetry. Thus, $9 - 1 + 2 = 10$ which are the 10 different symmetry classes in which a first-quantized Hamiltonian H can be.

Table 2.1 shows the 10 different symmetry classes corresponding to topological phases. The first column is the label that the mathematician Élie Cartan assigned to the different symmetric spaces [55, 56]. He obtained the same result by studying the different generalizations of spheres with constant curvature. The next three columns correspond to the symmetries that we have discussed. Zero means that the symmetry is not present, ± 1 gives the value to which the TR and PH operator squares, and for chiral, 1 indicates that the symmetry is present. On the fifth column, the coset spaces where the time evolution operator lives are represented. All these spaces can be obtained recursively by fixing the constraints of the symmetries when they are present. The simplest case is class A, which does not have any symmetry. Consequently, the Hamiltonian does not have a limitation, and it will be a general $N \times N$ Hermitian matrix. When TR is present and $T^2 = +1$, the Hamiltonian in a certain basis will be given by a real symmetric matrix H_s. As any Hermitian matrix H can be decomposed in a symmetric and antisymmetric part, $H_s = H - H_a$. Then, the time evolution operator correspondent to H_s will live in the coset space $\mathrm{U}(N)/\mathrm{O}(N)$, as the exponentiation of the Hermitian and asymmetric Hamiltonian lives in $\mathrm{U}(N)$ and $\mathrm{O}(N)$, respectively. This means that $e^{itH} \in \mathrm{U}(N)$ and $e^{itH_a} \in \mathrm{O}(N)$. Following a similar reasoning, one can continue imposing the limitations to the Hamiltonian due to the symmetries and obtain the rest of the symmetric spaces

A characteristic feature of topological phases is to present a topological invariant. Hence, if the listed symmetric spaces are in a non-trivial phase, there must have one topological invariant assigned to them. As a matter of fact, this is the case, and the corresponding invariants are shown in table 2.2.

To understand how the topological invariants appear, we look back to the last column of table 2.1. The classification of the ten symmetry classes is in one-to-one correspondence with a problem of Anderson localization [48], which is a phenomenon that occurs when translational symmetry is broken [37]. A way to achieve this is by placing impurities in the material, as they will disturb the potential landscape. When this type of disorder is strong enough, the spatially

Cartan\d	0	1	2	3	4	5	6	7	8	
Complex case:										
A	$\mathbb{Z}$	0	$\mathbb{Z}$	0	$\mathbb{Z}$	0	$\mathbb{Z}$	0	$\mathbb{Z}$	$\cdots$
AIII	0	$\mathbb{Z}$	0	$\mathbb{Z}$	0	$\mathbb{Z}$	0	$\mathbb{Z}$	0	$\cdots$
Real case:										
AI	$\mathbb{Z}$	0	0	0	$2\mathbb{Z}$	0	$\mathbb{Z}_2$	$\mathbb{Z}_2$	$\mathbb{Z}$	$\cdots$
BDI	$\mathbb{Z}_2$	$\mathbb{Z}$	0	0	0	$2\mathbb{Z}$	0	$\mathbb{Z}_2$	$\mathbb{Z}_2$	$\cdots$
D	$\mathbb{Z}_2$	$\mathbb{Z}_2$	$\mathbb{Z}$	0	0	0	$2\mathbb{Z}$	0	$\mathbb{Z}_2$	$\cdots$
DIII	0	$\mathbb{Z}_2$	$\mathbb{Z}_2$	$\mathbb{Z}$	0	0	0	$2\mathbb{Z}$	0	$\cdots$
AII	$2\mathbb{Z}$	0	$\mathbb{Z}_2$	$\mathbb{Z}_2$	$\mathbb{Z}$	0	0	0	$2\mathbb{Z}$	$\cdots$
CII	0	$2\mathbb{Z}$	0	$\mathbb{Z}_2$	$\mathbb{Z}_2$	$\mathbb{Z}$	0	0	0	$\cdots$
C	0	0	$2\mathbb{Z}$	0	$\mathbb{Z}_2$	$\mathbb{Z}_2$	$\mathbb{Z}$	0	0	$\cdots$
CI	0	0	0	$2\mathbb{Z}$	0	$\mathbb{Z}_2$	$\mathbb{Z}_2$	$\mathbb{Z}$	0	$\cdots$

Table 2.2: Classification of topological phases of matter as a function of the symmetries present. Depending on the dimensionality they will have a different topological invariant. When the system is in a trivial phase is represented by a 0. If there is a topological phase labeled by an integer, appears a $\mathbb{Z}$, and if is labeled by even integers a $2\mathbb{Z}$. The $\mathbb{Z}_2$ indicates the existence of trivial and non-trivial phase. See that there is a period of 8, meaning that the d, and the $d-8$ dimensional symmetry classes have the same topological classification. This is known as Bott periodicity.This table has been reproduced from [49].

extended states tend to become exponentially localized near the impurities [37, 57]. This is what is known as an Anderson insulator, which does not transport neither current nor heat. However, the gapless boundary modes in topological phases are due to the topology of the bulk, and therefore they must be insensitive to the disorder. Then, we can achieve the classification of topological phases in d dimensions by studying the evasion of Anderson localization of a $\bar{d} = d - 1$ dimensional boundary, which can be accomplished by a non-linear sigma model (NLσM) field theory [48]. This type of model is used to describe a Heisenberg ferromagnet, where at each point of the space we design a spin vector, pointing to the surface of a sphere. In our case, there is a field which points to the generalized sphere, hence $\Phi(r) \in G/H$. Then, if the action of the NLσM describing the $\bar{d}$ dimensional boundary contains a term that has a purely topological origin, then it will evade the Anderson localization [48].

The scope of this section was to provide a method and some arguments to support table 2.2. Therefore, we will just state the answer to the possible terms, which rely on the Homotopy Group $\pi_{\bar{d}}(G/H)$, of the $\bar{d}$ dimensional target space G/H. The reader who would like to know more is referred to Ref. [48, 49].

The action of the NLσM will evade the Anderson localization problem when it allows:

- a $\mathbb{Z}_2$ topological term $\iff \pi_{\bar{d}}(G/H) = \mathbb{Z}_2$
- a Wess - Zumino - Witten term $\iff \pi_{\bar{d}+1}(G/H) = \mathbb{Z}$.

In this chapter, we have seen how the three discrete symmetries, namely time reversal, particle hole, and chiral symmetry are defined. Depending on whether they are present or not, they will constrain the time evolution operator to live in one of the ten symmetric spaces summarized in table 2.1. Moreover, depending on the dimensionality, a trivial (0) or a topological phase ($\mathbb{Z}$, $\mathbb{Z}_2$ or $2\mathbb{Z}$) may exist, if and only if the target space of the NLσM evades Anderson localization at the boundary. However, this classification in terms of the dimensionality shown at table 2.2 corresponds to integer dimensions. Then, a natural question arises when we think about systems that have a non-integer dimension, such as fractals. Will these topological phases still be present, or they will not survive? Can a similar classifications be derived for fractional dimensions? In this thesis, we will investigate at what happens when we

confine electrons in a Sierpinski triangle. Then, we will include the spin-orbit coupling, which may drive matter into topological phases, and verify whether if characteristic features, such as corner or edge modes, appear in this fractal geometry.

Chapter 3

Fractals

We have seen at the end of last chapter that the topological nature of systems is deeply related to their dimension. There have been different kinds of extension of the classification of topological insulators. One of these focusses on different symmetries, in addition to time-reversal, particle-hole, or chiral symmetry such as lattice symmetries. Other efforts considered non-Hermitian Hamiltonians or driven (Floquet) systems. A natural question is whether a classification of topological insulators can be extended to non-integer dimension. Some recent studies have focused on the topological properties of fractal lattices. S. Fischer *et al.* [58] mapped the Haldane's Chern insulator and Hofstadter problem to a fractal lattice. They showed that although in two dimensions the boundary modes are topological, the edge states of the fractal realizations had no universal properties, and their stability depends on the model. Nevertheless, calculations of the Hall conductivity in a Sierpiński carpet by M. Fremling *et al.* [59] showed that the edge states contributed in a quantized way to the transverse conductivity. Moreover, in presence of disorder the phenomena remained robust. In this chapter, we will present some fractal geometries and define their main properties such as their non-integer dimension.

The word Fractal comes from fractus, which means fractured, and originates from Latin. The term was coined by Mandelbrot in 1975, although the first examples where already studied at the end of the XIX century. Fractals are self-similar structures with a non-integer dimension [60] that appear in many fields, ranging from biology [61, 62] (heartbeat, lungs, brain, and circulatory system) to economics [63] (stock market). The occurrence of fractals in such different areas can be attributed to their intricate geometry. For example, trees look like our lungs, both follow a branching pattern. Due to this pattern, they can realize a much larger area in a smaller volume, being able to store more O_2 or CO_2. Since fractal geometries are abundant in nature, it is important to understand how electronic quantum systems behave when they are constrained in such geometries. The vast majority of studies in quantum systems focuses on integer dimensions, and not much is known for fractional dimensions. Yet, dimensionality is well known to strongly impact material properties.

An example of a mathematical fractal is shown Fig. 3.1, which corresponds to the Sierpiński triangle. It is built by starting with a filled triangle and cutting an inverted triangle in its center (see white region in Fig. 3.1). We depict its building block, an equilateral triangle labeled by G=0, and the fist three generations. The first-order generation, G=1, is built by combining three copies of such a triangle. Proceeding iteratively, we can construct any generation by using the previous one.

It is interesting to notice that if one keeps repeating this procedure ad infinitum, the area is going to be zero and the perimeter infinite. This seems to be paradoxical, but it has an easy explanation. If the area and the perimeter of the equilateral triangle $G = 0$ are respectively given by A_0 and P_0, for the first generation $G = 1$ they are going to be given by $A_1 = \frac{3}{4}A_0$ and

Figure 3.1: Building block ($G = 0$) and Sierpiński triangles for the first three generations.

$P_1 = \frac{3}{2}A_0$, as we have removed the central triangle, which is a quarter of the original triangle. For the perimeter, as the inner sides of the new small triangles are $1/2$ of the original one, they add $3/2$ more. Hence, if one keeps repeating this scaling procedure, one obtains the limits:

$$A_\infty = \lim_{G\to\infty}\left(\frac{3}{4}\right)^G = 0, \qquad P_\infty = \lim_{G\to\infty}\left(\frac{3}{2}\right)^G = \infty.$$

This is only valid in theory, because in reality they will be always finite. The Hausdorff-Besicovitch dimension is the generalized metric concept of a topological space, which can have non-integer values. It is defined by

$$d_H = -\lim_{\epsilon\to 0^+}\frac{\ln N}{\ln \epsilon} \tag{3.1}$$

where N is the number of elements forming the finite cover and ϵ is the diameter of the sets forming the cover [60]. For the Sierpiński triangle, N is the number of triangles that we have in a given generation and ϵ is the length of the side of a triangle. Therefore, we have after G generations $N_G = 3^G$ and $L_G = (1/2)^G$ and thus,

$$d_H = \lim_{G\to\infty}\frac{\ln 3}{\ln 2} \approx 1.58.$$

Another typical example of a fractal is the Koch snowflake, which has as well an equilateral triangle as a starting point. To construct the next generation one removes the inner third of each side and one draws an equilateral triangle where the side was removed. In Fig. 3.2, we have illustrated the first few iterations.

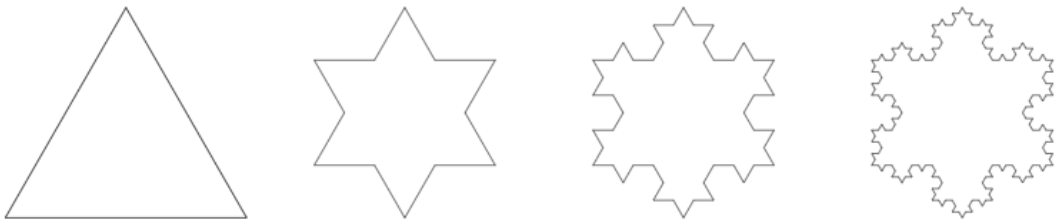

Figure 3.2: Building block and first three iterations.

The unit of self-similarity is also known as Koch curve, see Fig. 3.3. The iterative procedure is established by replacing each straight segment by the Koch curve.

As each side is replaced for a Koch curve, after G generations the number of sides is given by $N_G = 3\cdot(4/3)^G$ and each side will have length $L_G = (1/3)^G$. The perimeter is then given by $P_G = N_G \cot L_G = 3(3/4)^G$. The area can be obtained by using a recurrence equation and solving in terms of the initial area A_0, to find

$$A_G = A_{G-1} + \frac{1}{4}N_G L_G^2 A_0,$$

which gives $A_\infty = 8/5A_0$. As before we can define the Hausdorff dimension, which is given by $d_H = -\lim \frac{\ln N_G}{\ln L_G} \approx 1.26$.

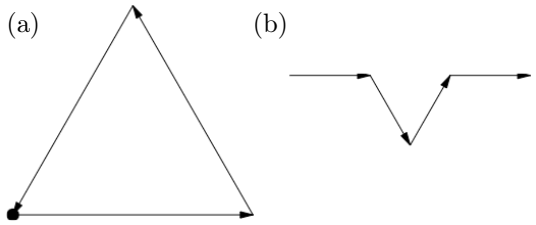

Figure 3.3: (a) building block and right (b) Koch curve.

Chapter 4

Effect of Spin-Orbit Coupling

In this chapter, we will show how to derive, the spin orbit coupling (SOC) Hamiltonian from a microscopic description. We will follow the lecture notes from the course Atomic Physics and Radiation [64]. The intrinsic spin-orbit coupling comes from the fine structure of the Hamiltonian, which includes relativistic effects up to second order in v/c. We begin with the time independent Dirac equation and perform the minimal coupling substitution, thus obtaining the motion of an electron and a positron in an electromagnetic field described by the vector potential $\boldsymbol{A}$ and escalar potential φ,

$$\mathcal{H}_D \to \mathcal{H}_D - e\varphi, \quad -i\hbar\nabla \to -i\hbar\nabla + \frac{e}{c}\boldsymbol{A}.$$

In the bi-spinor representation, this reads

$$\mathcal{H}_D\boldsymbol{\psi} = \begin{pmatrix} m_e c^2 - e\varphi & c\boldsymbol{\sigma}\cdot\left(-i\hbar\nabla + \frac{e}{c}\boldsymbol{A}\right) \\ c\boldsymbol{\sigma}\cdot\left(-i\hbar\nabla + \frac{e}{c}\boldsymbol{A}\right) & -m_e c^2 - e\varphi \end{pmatrix} \begin{pmatrix} \psi_e(\boldsymbol{r}) \\ \psi_p(\boldsymbol{r}) \end{pmatrix} = W \begin{pmatrix} \psi_e(\boldsymbol{r}) \\ \psi_p(\boldsymbol{r}) \end{pmatrix}, \tag{4.1}$$

with $W = \sqrt{c^2\boldsymbol{p}^2 + m_e^2 c^4}$ the relativistic energy and $\psi_e(\boldsymbol{r})(\psi_p(\boldsymbol{r}))$ the electron (positron) wavefunction. To study the non-relativistic limit, we first need to identify the non-relativistic energy with $E = W - m_e c^2$. The two coupled equations from (4.1) are

$$E\psi_e(\boldsymbol{r}) = -e\varphi\psi_e(\boldsymbol{r}) + c\boldsymbol{\sigma}\cdot\boldsymbol{\Pi}\psi_p(\boldsymbol{r}), \tag{4.2}$$

$$E\psi_p(\boldsymbol{r}) = c\boldsymbol{\sigma}\cdot\boldsymbol{\Pi}\psi_e(\boldsymbol{r}) - \left(2m_e c^2 + e\varphi\right)\psi_p(\boldsymbol{r}), \tag{4.3}$$

and $\boldsymbol{\Pi} = -i\hbar\nabla + \frac{e}{c}\boldsymbol{A}$ is the cinematic momentum. Using these equations, we can rewrite the solutions and expand them as a power series

$$\psi_p = \frac{c\boldsymbol{\sigma}\cdot\boldsymbol{\Pi}}{E + 2m_e c^2 + e\varphi}\psi_e \approx \frac{\boldsymbol{\sigma}\cdot\boldsymbol{\Pi}}{2m_e c}\left(1 - \frac{E + e\varphi}{2m_e c^2} + \cdots\right)\psi_e. \tag{4.4}$$

If we consider at the first-order contribution, we find

$$\psi_p \approx \frac{\boldsymbol{\sigma}\cdot\boldsymbol{\Pi}}{2m_e c}\psi_e, \tag{4.5}$$

and therefore, we can rewrite Eq. (4.2) as

$$E\psi_e(\boldsymbol{r}) \approx -e\varphi\psi_e(\boldsymbol{r}) + \frac{\left(\boldsymbol{\sigma}\cdot\boldsymbol{\Pi}\right)^2}{2m_e}\psi_e.$$

Using the following two relations,

$$\left(\boldsymbol{a}\cdot\boldsymbol{\sigma}\right)\left(\boldsymbol{b}\cdot\boldsymbol{\sigma}\right) = \boldsymbol{a}\cdot\boldsymbol{b} + i(\boldsymbol{a}\times\boldsymbol{b})\cdot\boldsymbol{\sigma},$$
$$(-i\hbar\nabla)\times\boldsymbol{A} = -i\hbar\left(\nabla\times\boldsymbol{A}\right) - \boldsymbol{A}\times(-i\hbar\nabla),$$

we can rewrite

$$(\boldsymbol{\sigma}\cdot\boldsymbol{\Pi})^2 = \boldsymbol{\Pi}^2 + i\boldsymbol{\sigma}\cdot(\boldsymbol{\Pi}\times\boldsymbol{\Pi}) = \left(-i\hbar\nabla + \frac{e}{c}\boldsymbol{A}\right)^2 + i\frac{e}{c}\boldsymbol{\sigma}\Big((-i\hbar\nabla)\times\boldsymbol{A} + \boldsymbol{A}\times(-i\hbar\nabla)\Big)$$
$$= \left(-i\hbar\nabla + \frac{e}{c}\boldsymbol{A}\right)^2 + \frac{e\hbar}{c}\boldsymbol{\sigma}\cdot(\nabla\times\boldsymbol{A})\,.$$

We can see that the first order correction is the Pauli Hamiltonian, which shows how the Dirac equation describes particles with spin $\frac{1}{2}$ and the giromagnetic ratio of the electron is $g_s = 2$ (corrections to this appear in quantum electrodynamics, which are a few orders smaller). Thus,

$$\mathcal{H}_P = \frac{1}{2m_e}\left(-i\hbar\nabla + \frac{e}{c}\boldsymbol{A}\right)^2 - e\varphi + \frac{e\hbar}{2m_e c}\boldsymbol{\sigma}\cdot(\nabla\times\boldsymbol{A})\,. \tag{4.6}$$

However, this first-order correction does not change the energy levels for fields that allow bounded states. Therefore, to include relativistic effects we need to go to second order in v/c. From equation (4.3), we can substitute the first-order approximation (4.5)

$$\psi_p = \frac{\boldsymbol{\sigma}\cdot\boldsymbol{\Pi}}{2m_e c}\psi_e - \frac{E+e\varphi}{2m_e c^2}\psi_p = \frac{\boldsymbol{\sigma}\cdot\boldsymbol{\Pi}}{2m_e c}\psi_e - \frac{E+e\varphi}{2m_e c^2}\frac{\boldsymbol{\sigma}\cdot\boldsymbol{\Pi}}{2m_e c}\psi_e.$$

If we then substitute this last expression to the eigenvalue equation (4.2), we obtain

$$(\mathcal{H}_P + \mathcal{H}')\,\psi_e = E\psi_e \tag{4.7}$$

with

$$\mathcal{H}' = -\frac{1}{4m_e^2c^2}(\boldsymbol{\sigma}\cdot\boldsymbol{\Pi})(E+e\varphi)(\boldsymbol{\sigma}\cdot\boldsymbol{\Pi}) \tag{4.8}$$

denoting the second order contribution. Using that

$$[\boldsymbol{\sigma}\cdot\boldsymbol{\Pi}, E+e\varphi] = [\boldsymbol{\sigma}\cdot(-i\hbar\nabla), E+e\varphi] = e(\boldsymbol{\sigma}\cdot(-i\hbar\nabla))\varphi - e\varphi(\boldsymbol{\sigma}\cdot(-i\hbar\nabla)) = -ie\hbar(\boldsymbol{\sigma}\cdot\nabla\varphi),$$

we can rewrite

$$\mathcal{H}' = -\frac{1}{4m_e^2c^2}(\boldsymbol{\sigma}\cdot\boldsymbol{\Pi})\Big\{(\boldsymbol{\sigma}\cdot\boldsymbol{\Pi})(E+e\varphi) - [\boldsymbol{\sigma}\cdot\boldsymbol{\Pi}, E+e\varphi]\Big\}$$
$$= -\frac{1}{4m_e^2c^2}(\boldsymbol{\sigma}\cdot\boldsymbol{\Pi})^2(E+e\varphi) - \frac{ie\hbar}{4m_e^2c^2}(\boldsymbol{\sigma}\cdot\boldsymbol{\Pi})(\boldsymbol{\sigma}\cdot\nabla\varphi)$$
$$= -\frac{1}{4m_e^2c^2}\left[\left(\boldsymbol{p}+\frac{e}{c}\boldsymbol{A}\right)^2 - \frac{e\hbar}{c}\boldsymbol{\sigma}\cdot(\nabla\times\boldsymbol{A})\right](E+e\varphi) - \frac{ie\hbar}{4m_e^2c^2}\left[\boldsymbol{\sigma}\cdot\left(-i\hbar\nabla + \frac{e}{c}\boldsymbol{A}\right)\right](\boldsymbol{\sigma}\cdot\nabla\varphi).$$

If we expand this last expression, drop out terms of higher order than $O((\frac{v}{c})^2)$, and use the relation from the Pauli equation

$$E + e\varphi = \frac{p^2}{2m_e} + O\left(\frac{v}{c}\right),$$

we obtain

$$\mathcal{H}' \approx -\frac{p^4}{8m_e^3c^2} + \frac{e\hbar}{4m_e^2c^2}\boldsymbol{\sigma}\cdot(-i\hbar\nabla\times(\nabla\varphi)) - \frac{ie\hbar}{4m_e^2c^2}(-i\hbar\nabla)\cdot(\nabla\varphi).$$

Since

$$-i\hbar\nabla\times(\nabla\varphi) = -i\hbar[\nabla\times(\nabla\varphi)] - (\nabla\varphi)\times(-i\hbar\nabla) = -(\nabla\varphi)\times(-i\hbar\nabla),$$

we finally obtain

$$\mathcal{H}' \approx -\frac{p^4}{8m_e^3c^2} - \frac{e\hbar}{4m_e^2c^2}\boldsymbol{\sigma}\cdot(\nabla\varphi)\times(-i\hbar\nabla) - \frac{ie\hbar}{4m_e^2c^2}(-i\hbar\nabla)\cdot(\nabla\varphi). \tag{4.9}$$

Looking at equation (4.9), we can see that the last term is non Hermitian and therefore, the norm of the state will not be conserved, leading to a decrease of the probability. This happens because the wave-function ψ_e does not represent correctly the non-relativistic limit of the Dirac equation at order $(v/c)^2$. By using (4.5), the norm at order $(v/c)^2$ is given by

$$\boldsymbol{\psi}^\dagger\boldsymbol{\psi} = \psi_e^*\psi_e + \psi_p^*\psi_p \approx \psi_e^*\left(1+\frac{p^2}{4m_e^2c^2}\right)\psi_e \approx \left[\left(1+\frac{p^2}{8m_e^2c^2}\right)\psi_e\right]^*\left(1+\frac{p^2}{8m_e^2c^2}\right)\psi_e,$$

and therefore the wave-function with constant norm is given by

$$\psi^{(nr)} = \left(1+\frac{p^2}{8m_e^2c^2}\right)\psi_e. \tag{4.10}$$

To obtain the Hermitian Hamiltonian that has $\psi^{(nr)}$ as an eigenstate, we multiply equation (4.7) by $1+\frac{p^2}{8m_e^2c^2}$,

$$\begin{aligned}\left(1+\frac{p^2}{8m_e^2c^2}\right)E\psi_e &= \left(1+\frac{p^2}{8m_e^2c^2}\right)(\mathcal{H}_P+\mathcal{H}')\,\psi_e \\ E\psi^{(nr)} &= (\mathcal{H}_P+\mathcal{H}')\,\psi^{(nr)} + \left[1+\frac{p^2}{8m_e^2c^2},\mathcal{H}_P+\mathcal{H}'\right]\psi_e.\end{aligned}$$

The commutator can be approximated as

$$\begin{aligned}\left[1+\frac{p^2}{8m_e^2c^2},\mathcal{H}_P+\mathcal{H}'\right] &= \frac{1}{8m_e^2c^2}[(-i\hbar\nabla)^2,\mathcal{H}_P+\mathcal{H}'] \approx \frac{1}{8m_e^2c^2}[(-i\hbar\nabla)^2,-e\varphi] \\ &= -\frac{e}{8m_e^2c^2}\left(-i\hbar\nabla\cdot[-i\hbar\nabla,\varphi]+[-i\hbar\nabla,\varphi]\cdot-i\hbar\nabla\right) \\ &= -\frac{e}{8m_e^2c^2}\Big\{-i\hbar(-i\hbar\nabla)\cdot(\nabla\varphi)-i\hbar(\nabla\varphi)\cdot(-i\hbar\nabla) \\ &= \frac{e\hbar^2}{8m_e^2c^2}\Big\{\nabla\cdot(\nabla\varphi)+(\nabla\varphi)\cdot(\nabla)\Big\}.\end{aligned}$$

The final eigenvalue equation for an electron moving in an electromagnetic field with corrections up to $(v/c)^2$ is given by

$$E\psi^{(nr)} = \mathcal{H}_F\psi^{(nr)} = (\mathcal{H}_P+\mathcal{H}_m+\mathcal{H}_{SO}+\mathcal{H}_{Darwin})\,\psi^{(nr)}. \tag{4.11}$$

The Hamiltonian $\mathcal{H}_F$ is known as the fine-structure Hamiltonian, and as we can see, it has four different contributions,

$$\mathcal{H}_P = \frac{1}{2m_e}\left(-i\hbar\nabla+\frac{e}{c}\boldsymbol{A}\right)^2 - e\varphi + \frac{e\hbar}{2m_ec}\boldsymbol{\sigma}\cdot(\nabla\times\boldsymbol{A}), \tag{4.12}$$

$$\mathcal{H}_m = -\frac{p^4}{8m_e^3c^2}, \tag{4.13}$$

$$\mathcal{H}_{SO} = -\frac{e\hbar}{4m_e^2c^2}\boldsymbol{\sigma}\cdot((\nabla\varphi)\times\boldsymbol{p}), \tag{4.14}$$

$$\mathcal{H}_{Darwin} = \frac{e\hbar^2}{8m_e^2c^2}(\nabla^2\varphi). \tag{4.15}$$

The first one is the Pauli Hamiltonian $\mathcal{H}_P$, which emerges from the first-order relativistic corrections describing the kinetic energy and interaction energy of an electron with the electromagnetic field, as we have shown.

$\mathcal{H}_m$ represents the corrections to the mass of the particle due to relativistic effects up to $(v/c)^2$, as we can see in the expansion of the kinetic energy,

$$\sqrt{p^2c^2 + (m_e c^2)^2} = m_e c^2 + \frac{p^2}{2m_e} - \frac{p^4}{8m_e^3 c^2} + \cdots$$

$\mathcal{H}_{SO}$ is the intrinsic spin-orbit coupling, which originates from the electromagnetic interaction between the orbital and spin degrees of freedom of a particle. Electrons moving with velocity $\boldsymbol{v}$, which are bounded to the atomic nucleus due to the electric field $\boldsymbol{E} = -\boldsymbol{\nabla}\varphi$, will feel a magnetic field $\boldsymbol{B'} = \frac{1}{c}\boldsymbol{v} \times \boldsymbol{E} = -\frac{1}{c}(\boldsymbol{\nabla}\varphi) \times \boldsymbol{v}$ in its rest reference frame. This field is going to couple with the spin magnetic moment of the electron μ_s, giving rise to an interaction energy between both given by

$$-\boldsymbol{\mathcal{M}}_s \cdot \boldsymbol{B'} = -g_s \mu_B \boldsymbol{S} \cdot \frac{1}{c}(\boldsymbol{\nabla}\varphi) \times \boldsymbol{v} = -\frac{e\hbar}{2m_e^2 c^2}\boldsymbol{\sigma}(\boldsymbol{\nabla}\varphi) \times \boldsymbol{p}. \tag{4.16}$$

This last expression, however, has a factor of 1/2 missing known as Thomas factor. To obtain the correct form, one needs to take into account that when the reference frame of the electron accelerates with respect to the lab, the spin of the electron experiments a precession independent of the presence of a magnetic field. This precession occurs because: two consecutive Lorentz boost are equivalent to one boost and a rotation [65].

The last term, $\mathcal{H}_{Darwin}$, is a consequence of an interference between the positive and negative components of the wave packet, causing violent oscillations to the electron (*Zitterbewegung*). It is also called a contact term, since the Poisson equation $\nabla^2\varphi = 4\pi\rho$ needs to be verified, and therefore, it is only non-zero for s orbitals [66].

4.1 Intrinsic Spin-Orbit Coupling and Topological Phases

We have seen how the coupling between the spin and angular momentum of an electron emerges naturally when relativistic effects, up to second order in v/c, are taken into account. The importance of this interaction is that it is believed to play a crucial role in driving matter to topological phases. In 2005, Kane and Mele introduced the spin-orbit coupling in the tight-binding description of graphene [4, 5]. This led them to the quantum spin Hall (QSH) phase. In this new state, a topological gap is opened at the bulk, while a pair of counterpropagating modes move along the edge. These boundary modes are helical: the spin is locked with the motion of the particles, such that the helicity $h = \boldsymbol{\sigma} \cdot \boldsymbol{p}$ is preserved. Hence, spin-up electrons move in one direction and spin-down ones move in the opposite direction. The pair is related by time-reversal symmetry, (a so-called Kramer's pair) and as long as the bulk gap is not closed, or time-reversal symmetry is broken by some strong interaction or a magnetic field, they will be insensitive to scattering effects. Therefore, they are protected by symmetries and the material is a time-reversal topological insulator. The band structure of the QSH phase is classified by a Z_2 topological invariant, which is 1 when the boundary modes are present at the topological phase, or 0 if they are not present at the insulating phase (trivial).

This new state of matter is very interesting because it could have novel applications in spintronic devices, which could serve, for example, for filtering the spin. However, the main problem is that graphene is made of carbon atoms, which has a very small spin-orbit coupling, and consequently the topological gap opened is also very small. In fact, for graphene the gap is of the order of 10^{-3} meV, and to suppress all thermal excitations from the bulk, we would need to go to temperatures around $0.01K$ [67]. Experimentally, the QSH phase was first observed in HgTe/CdTe quantum wells at mK temperatures [68, 69], and after in InAs/GaSb heterostructures [70]. As a consequence, no real world device can be developed and take profit of this

material properties due to this low operation temperature. To overcome this issue, the research has been focused on enhancing the topological gap, looking for new material candidates that could host a QSH effect, but now at room temperature. Since the gap is proportional to the spin-orbit coupling strength, the first option would be to find materials that have a stronger spin-orbit coupling.

4.2 Spin-Orbit Coupling Strenght

As an approximation, we can investigate the spin-orbit coupling for hydrogen-like atoms. If an electron moves in a Coulomb electrostatic potential, the potential energy is given by

$$V(r) = -e\varphi(r) = -\frac{1}{4\pi\epsilon_0}\frac{Ze^2}{r},$$

with Ze the charge of the nucleus and e the electron charge. In this section we will recover the factor of $1/4\pi\epsilon_0$ with ϵ_0 the vacuum electric permittivity. Before taking the mean value of the spin-orbit coupling Hamiltonian, we can rewrite equation (4.14) in terms of the spin and angular momentum operators,

$$\mathcal{H}_{SO} = -\frac{e}{2m_e^2c^2}\boldsymbol{S}\cdot\left(\frac{\boldsymbol{r}}{r}\frac{\mathrm{d}\varphi}{\mathrm{d}r}\times\boldsymbol{p}\right) = \frac{1}{2m_e^2c^2}\frac{1}{r}\frac{\mathrm{d}V}{\mathrm{d}r}\boldsymbol{S}\cdot(\boldsymbol{r}\times\boldsymbol{p}) = \frac{1}{2m_e^2c^2}\frac{Ze^2}{r^3}\boldsymbol{L}\cdot\boldsymbol{S} = \xi(r)\boldsymbol{L}\cdot\boldsymbol{S}. \quad (4.17)$$

To compute now $\langle\mathcal{H}_{SO}\rangle$, we need to fix a basis. We can choose between two different complete sets of compatible observables that define their own different basis. Either $\{\mathcal{H}, \boldsymbol{L}^2, \boldsymbol{S}^2, L_z, S_z\}$ or $\{\mathcal{H}, \boldsymbol{L}^2, \boldsymbol{S}^2, \boldsymbol{J}^2, J_z\}$, with their respective basis $\{|n,\ell,m_L,m_S\rangle\}$ or $\{|n,\ell,j,m\rangle\}$, where $\boldsymbol{J} = \boldsymbol{L}+\boldsymbol{S}$ is the total angular momentum. However, it is better to work with the second basis because $\boldsymbol{L}\cdot\boldsymbol{S} = \frac{1}{2}(\boldsymbol{J}^2 - \boldsymbol{L}^2 - \boldsymbol{S}^2)$, and thus $\mathcal{H}_{SO}$ is already diagonal. The proper functions of this basis are spherical harmonics and are given by

$$\psi(\boldsymbol{r},\sigma)_{jn\ell m} = \frac{1}{r}P_{n\ell j}(r)\Omega^{\ell}_{jm}(\hat{\boldsymbol{r}},\sigma) := \langle\boldsymbol{r},\sigma|n,\ell,j,m\rangle\,, \quad (4.18)$$

with $P_{n\ell j}(r)$ satisfying the radial part of the Schrödinger equation and the spherical spinors Ω^{ℓ}_{jm}, the angular contribution. If we now take the mean value of equation (4.17), we can observe that the energy displacement is proportional to Z^4,

$$\begin{aligned}\langle\mathcal{H}_{SO}\rangle &= \langle n,\ell,j,m|\,\mathcal{H}_{SO}\,|n,\ell,j,m\rangle = \int_0^\infty P_{n\ell j}(r)\xi(r)P_{n\ell j}(r)\,\mathrm{d}r\int\left[\Omega^{(\ell)}_{jm}(\hat{\boldsymbol{r}},\sigma)\right]^\dagger\boldsymbol{L}\cdot\boldsymbol{S}\Omega^{(\ell)}_{jm}(\hat{\boldsymbol{r}},\sigma)\,\mathrm{d}\Omega \\ &= \frac{\hbar}{2}\langle\xi(r)\rangle\Big[j(j+1)-l(l+1)-3/4\Big] = \frac{\hbar}{2}\frac{1}{2m_e^2c^2}\frac{Ze^2}{4\pi\epsilon_0}\langle r^{-3}\rangle\Big[j(j+1)-l(l+1)-3/4\Big],\end{aligned}$$

for $\ell\neq 0$ and zero otherwise. By using that

$$\langle r^{-3}\rangle = \frac{Z^3}{a_0^3n^3\ell(\ell+1/2)(\ell+1)},$$

we can rewrite $\langle\mathcal{H}_{SO}\rangle$ as

$$\langle\mathcal{H}_{SO}\rangle = \frac{\hbar}{2}\frac{1}{2m_e^2c^2}\frac{Ze^2}{4\pi\epsilon_0}\frac{Z^3}{a_0^3n^3}\left[\frac{j(j+1)-l(l+1)-3/4}{\ell(\ell+1/2)(\ell+1)}\right] = -E_n\frac{Z^2\alpha^2}{2n}\left[\frac{j(j+1)-l(l+1)-3/4}{\ell(\ell+1/2)(\ell+1)}\right]. \quad (4.19)$$

We used that the energy levels are given by $E_n = -\frac{e^2}{4\pi\epsilon_0 a_0}\frac{Z^2}{2n^2}$, the Bohr radius $a_0 = \frac{4\pi\epsilon_0\hbar^2}{e^2m_e}$, and the fine structure constant is $\alpha = \frac{e^2}{4\pi\epsilon_0\hbar c}$. If the spin-orbit coupling grows with the atomic number as Z^4, it is going to be much larger in heavier atoms, leading to an enhanced topological gap [6, 71–73].

Chapter 5

Experimental motivation

5.1 Bismuthene on a SiC substrate

In the past few years, researchers in condensed matter have driven their attention to the synthesis of two-dimensional lattices with hexagonal symmetry using elements of the group IV and V. The idea behind it is to simulate graphene physics, but with a larger topological gap. If this attempt is successful, these materials will not be constrained to operate at cryogenic temperatures. Hence, new spintronic devices, with dissipationless currents, will be developed for technological applications.

A promising result was a recent publication by Reis *et al.* [6]. In their work, they combined theory and experiment to demonstrate new realizations of a QSH phase at high temperature. The method consists in synthesizing a reconstructed monolayer of Bismuth atoms on top of SiC(0001). As we have seen, the atomic spin-orbit coupling in heavy-atom systems is much larger than in lighter ones. Thus, the Bi atoms with $Z = 83$ are an excellent candidate to exhibit robust topological effects. Indeed, Reis *et al.* have shown that the substrate where Bi is grown stabilizes its topological nature, thus confirming the theoretical prediction that a hexagonal lattice of ultrathin free-standing Bi atoms, called bismuthene, hosts a $\mathbb{Z}_2$ topological phase [73–75].

To describe the low-energy bands near the Fermi level, they developed a multi-orbital tight-binding Hamiltonian because the outer shell of the atom is $6s^2 6p^3$. The p_z orbitals point out of plane and are pushed to higher energy, as they hybridize with the substrate, forming π bonds. Due to this hybridization with the substrate, inversion symmetry is broken, allowing for a Rashba term that splits valence bands of opposite spins. Therefore, the remaining orbitals hybridize and form sp^2 orbitals, giving rise to σ bonds yielding the same honeycomb geometry as graphene. This σ sector, mainly p_x and p_y orbitals, is the main contribution at low energies and will be responsible for the increase of the topological gap, as they allow for a huge onsite SOC due to the coupling of the spin with the L_z component.

By performing perturbation theory and truncating to leading order, the effective Hamiltonian of the σ sector reads

$$H_{eff}^{\sigma\sigma} = H_0^{\sigma\sigma} + \lambda_{SOC} H_{SOC}^{\sigma\sigma} + \lambda_R H_R^{\sigma\sigma}, \tag{5.1}$$

where $H_0^{\sigma\sigma}$, $H_{SOC}^{\sigma\sigma}$, and $H_R^{\sigma\sigma}$ are the Hamiltonians corresponding to the hopping, intrinsic spin-orbit coupling, and Rashba effect, respectively (with λ_{SOC} and λ_R denoting their respective strength). The experimental evidence of a QSH phase with its characteristic non-trivial topological invariant $\mathbb{Z}_2 = 1$ is strongly supported by their theoretical calculations, using this "downfolding" procedure and orbital filtering [6, 71], as well as density functional theory [76, 77]. Furthermore, this QSH system is very different from the Kane and Mele model [4, 5].

It owns its nature to the large on site SOC, in contrast to the next-nearest neighbours SOC in graphene. By performing STM measurements, they observed a large bulk gap of $E \sim 0.8$ eV and conducting edge channels. For this reason, tight-binding calculations for heavy atoms with a multi-orbital basis, which allow for this type of SOC, is believed to be a key feature for predicting new QSH phases with large topological gaps.

5.2 Fractals in electronic quantum simulators

The way how we look at materials was revolutionized in 1981 by Binnig and Rohrer, when they invented the STM at IBM [13–15]. This was the first time that researchers could look at materials with atomic precision, obtaining topographic images with ultra-high resolution. Moreover, they could measure the density of electrons at all points of the sample, and their discovery additionally enabled them to rearrange atoms, one by one. Only five years later, they were awarded with the Noble Prize in Physics.

The ability to rearrange atoms can be used to experimentally realize fractal structures. In a recent work Kempkes *et al.* studied the consequence of confining electrons in a two-dimensional Sierpinski triangle [78]. To obtain this geometry, they inserted CO molecules in a Cu(111) substrate. Afterwards, they used of the STM to manipulate the CO's, to force the electrons into a fractal shape. Figure 5.1 shows that the lack of COs forms a Sierpinski fractal, while the COs form what is called the anti-lattice.

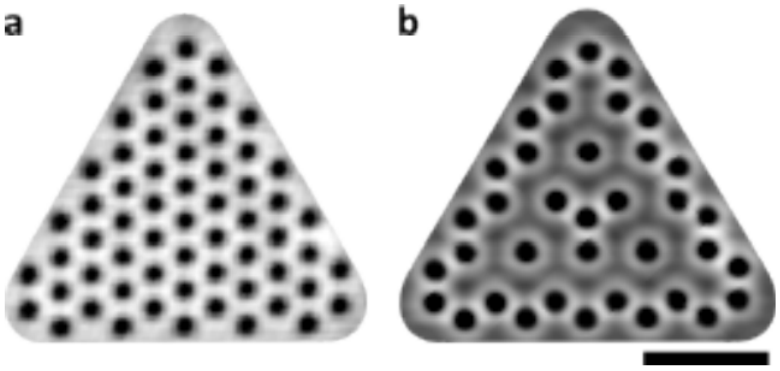

Figure 5.1: Images obtained with an STM. (**a**) Triangular lattice formed by the CO molecules bonded at the substrate. (**b**) After removing the CO's, the G(3) Sierpinski triangle is formed. The remaining CO form the anti-lattice, while the extracted ones form the tight-binding lattice. Scale bar: 4 nm. Figure adapted from Ref. [78].

To study how electrons behave in this fractal configuration, they used two different theoretical methods. The first method is called the muffin-tin approximation. In this approximation, the CO molecules act as potential barriers that repel the electrons on the substrate. The potential barriers are modeled with a circular step (disk) potential, resembling an upside-down muffin-tin. The configuration of the potential is illustrated in Fig. 5.2. The second method is the tight-binding model. Now, electrons are confined in each atomic site. They can hop to nearest neighbours (NN) and also to next-nearest neighbours (NNN). Observe that there is a big difference between the two methods. The latter can only have electrons at the atomic sites and the former hosts them in the whole region. Therefore, one is discrete and the other is continuum.

By solving these models, Kempkes *et al.* were able to compute the local density of states (LDOS). This is a measure that identifies where it is more probable to find electrons at a given energy, or in other words, how large is the amplitude of the electron's wavefunction. Figure

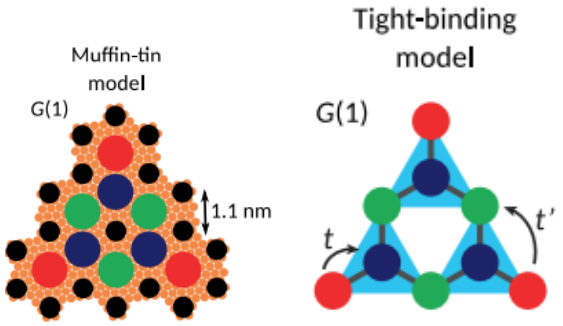

Figure 5.2: (a) Muffin tin model: the anti-lattice, patterned by the CO molecules, is represented by the black dots. These are the regions where electrons encounter a repulsive potential. In all the other sites, they are free to move. (b) The tight-binding model: here, electrons are located at these discrete points. They can hop to their nearest neighbour and next-nearest neighbour with amplitude t and t', respectively. The color code indicates the number of nearest neighbours that the site has: red (R) one, green (G) two, and blue (B) three. The distance between black dots is 1.1 nm. Figure reproduced from Ref. [78].

.

5.3 shows the LDOS measured with the STM and evaluated using the tight-binding approach. Although they are not fully identical, they share the main features and we can say that theory agrees with experiment. There are a few interesting voltage values. For $E = -0.325$ eV, the three different lattice sites (RBG) have a similar LDOS. At $E = -0.2$ eV, the B and G sites present a peak, while the red is in a minimum. Around $E = -0.1$ eV, the B sites present a minimum, while the R and G sites show a maximum. Finally, at $E = 0.1$ eV, R and G are minimum, while B is at a maximum.

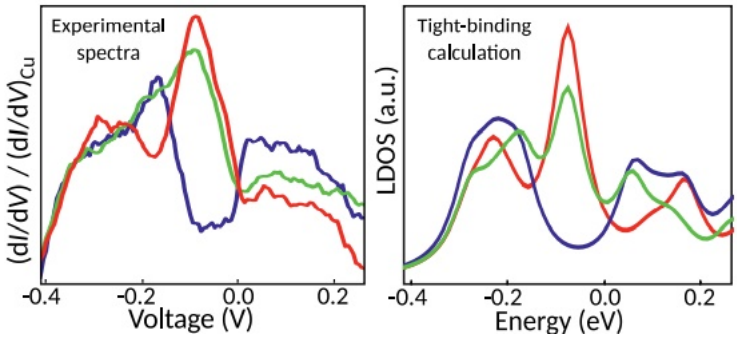

Figure 5.3: (a) Experimental spectra obtained using an STM. (b) Theoretically calculated tight-binding spectra. This image was reproduced from Ref. [78].

To further discuss these values of energy, we refer the reader to Fig. 5.4, where a comparison between the LDOS computed at each site for the two models and the experimental results is shown. The small yellow triangle of the last column corresponds to the G(1) region. Each circle follows the same color code as Fig. 5.2, and their areas are proportional to the LDOS. The first row, which corresponds to $E = -0.325$ eV, displays a similar LDOS for all sites. This is translated in to a fully connected Sierpinski triangle. Thus, electrons will have a strong bonding between sites and the conductivity through the path (RBGBR) is excellent. The second row at $E = -0.2$ eV is very interesting because one can observe the self-similarity of the Sierpinski triangle in the LDOS. The fully connected LDOS at $E = -0.325$ eV for G(3) is subdivided into nine self-similar G(1) parts at $E = -0.2$ eV, since the R sites connecting them have a low LDOS, hence a poor conductivity. The third row, at $E = -0.1$ eV, clearly

shows how a minimum in the LDOS for the blue sites affects the conductivity along (RBGBR) pathways. The NN interaction will drop consistently and electrons will need to propagate with the NNN hoping. The last row, which corresponds to $E = 0.1$ eV, is similar to the previous one, and the conductivity of electrons will also be suppressed. However, now the LDOS is maximum at the complementary (blue) sites. In general, one can conclude that the experiment and both theoretical results show significant correspondence. Nevertheless, the LDOS of the muffin-tin model is closer to the reality.

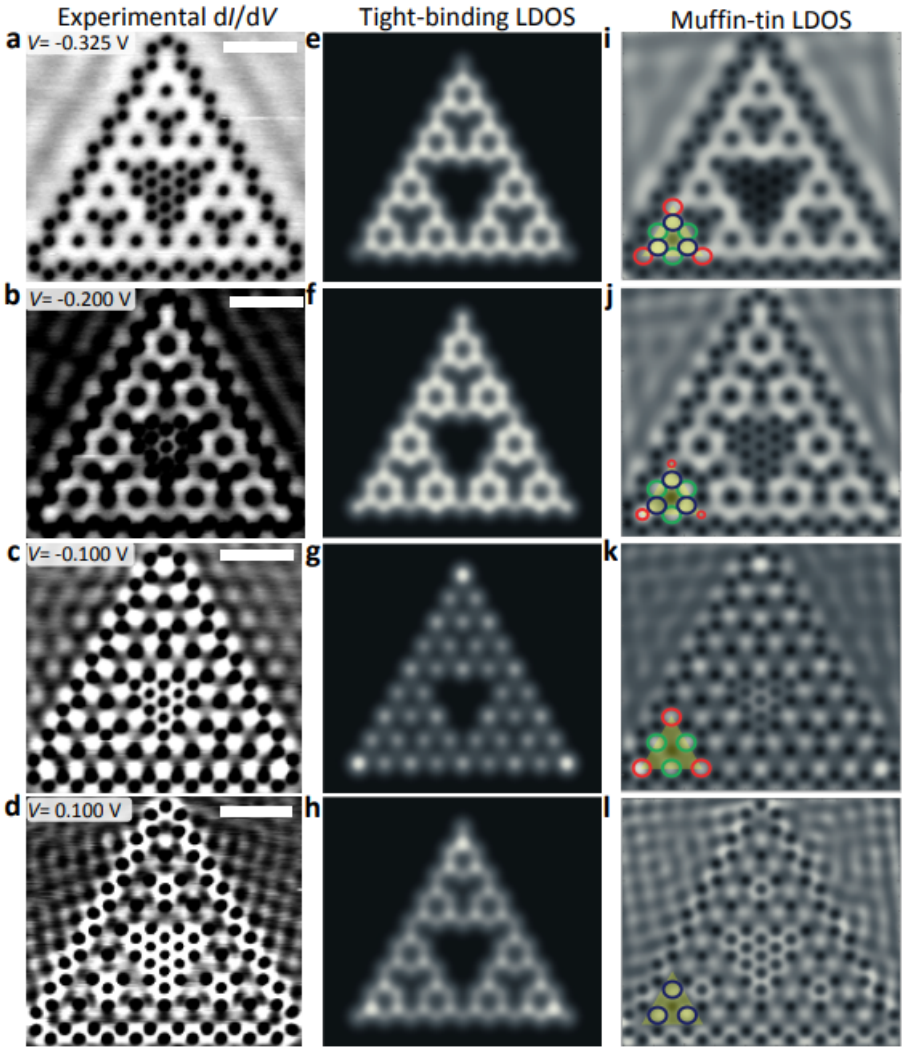

Figure 5.4: Each column presents the LDOS for the G(3) Sierpinski triangle. From left to right we can find the experiment, the tight-binding, and the muffin-tin calculations. Each row corresponds to the same potential, labeled in the top left corner. The yellow triangle represents the G(1) region with the colored circles distinguishing different sites. A larger LDOS is represented by a higher brightness. However, the colored circles have a bigger diameter in order to enhance the differences. This image was reproduced from Ref. [78].

Finally, they computed the LDOS for different generations, and observed that they exhibit the same pattern. This was an indication of the self similarity of the geometry. To verify whether the wavefunctions shared the scaling properties of the Sierpinski triangle, they computed the fractal dimension of the muffin-tin LDOS. The results indicated that the dimension

was indeed fractional, very close to the theoretical value 1.58 of the Sierpinski triangle. Then one can say that the wavefunctions of electrons confined in a fractal geometry also behave in a fractal manner, *i.e.* they are self similar and have a fractal dimension.

5.3 Quantum transport in fractal networks

Another interesting work in fractals is the one done by Xu *et al.*, where they studied the quantum dynamics of photons in different Hausdorff dimensions [79]. To unveil the transport, they built photonic lattices in Corning Eagle XG glass using femtosecond-laser direct-writing techniques. A sketch of the sample is depicted in Fig. 5.5.

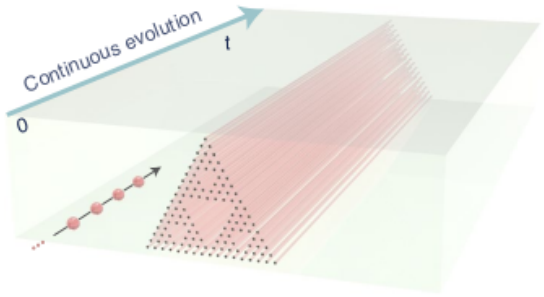

Figure 5.5: Sketch of the Sierpinski photonic sample. Arrow indicates the direction of time evolution. Figure reproduced from Ref. [79].

When a horizontally polarized photon is introduced at the corner of the fractal, the dynamics can be described by continuous-time quantum walks [80]. By building samples with different lengths they observed the evolution pattern of photons at different times, since the longitudinal propagation length Z is proportional to time. Then, to characterize quantitatively the diffusion scaling of photons over the fractal networks, they computed the mean square displacement (MSD) and the Pólya number [81].

The propagation of light in a waveguide j is given by the Helmholtz equation in the paraxial approximation. It reads

$$i\frac{\partial_j \psi}{\partial Z} = \sum_l H_{jl}\psi_l, \tag{5.2}$$

where H_{jl} indicates the coupling between waveguides j and l. Notice that then the propagation of light in the waveguide is analogous to a Schrödinger equation where Z plays the role of time and H of the Hamiltonian. To describe this system theoretically and simulate the experimental results, they assumed a tight-binding model with an onsite β_i propagation constant, and a NN coupling strength C_{ij}. Hence, the Hamiltonian reads

$$H = \sum_{i=1}^{N} \beta_i a_i^\dagger a_i + \sum_{<ij>} C_{ij} a_i^\dagger a_j, \tag{5.3}$$

with $a_i^\dagger$ and a_i the creation and annihilation operators, respectively, at site i. If the initial state at the corner is given by $|\psi(0)\rangle = |1\rangle$, after time t the state is $|\psi(t)\rangle = \sum_{j=1}^{N} a_j(t)\,|j\rangle = e^{-iHt}\,|\psi(0)\rangle$. Therefore, the probability distribution at time t can be expressed as

$$p_j(t) = |a_j(t)|^2 = |\langle j|\,U(t)\,|1\rangle|^2 = |U_{j1}(t)|^2. \tag{5.4}$$

Based on this distribution, the MSD defined as $\langle r^2(t)\rangle = \sum_j^N r_j^2 p_j(t)$ is straightforwardly computed. The other measure, the Pólya number, gives the probability that the initial state ever

returns to the starting point, defined as $P = 1 - \prod_i^{\infty}[1 - p_0(t_i)]$.

Figure 5.6 shows the comparison between the experimental and simulation results. Fig. 5.6(a) is a sketch of the cross section of the photonic lattice, showing the top vertex as the input position. The behaviour of the MSD is compared in the log-log plots of Fig. 5.6(b). Both

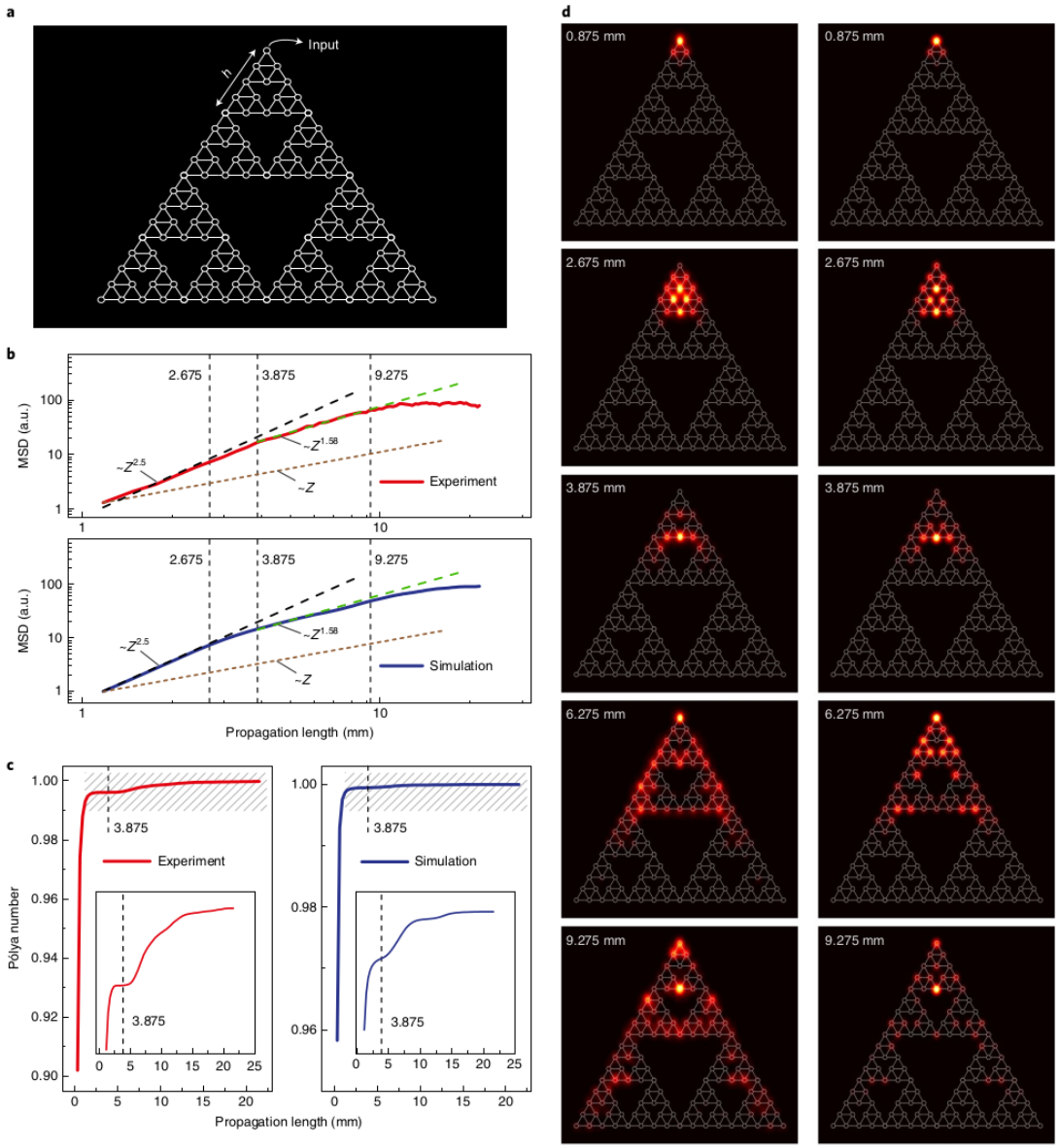

Figure 5.6: (a) Sketch of the cross section of a fractal photonic sample. (b) and (c) show the comparison between the experimental (red) and the simulation (blue), for the MSD and Pólya number, respectively. (d) Depict the transport patterns at different propagation lengths for the experimental observations on the left, and simulations on the right. Figure reproduced from Ref. [79].

show an excellent agreement along the entire sample. In contrast to infinite regular lattices that have a quadratic growth in the scaling behaviour [82, 83], in fractal samples the slope is continuously changing. From $0 < Z < 2.675$ mm, the quantum transport follows the normal regime. After the first void, the fractal geometry starts to exhibit its effects and the scaling

behaviour of the MSD is governed by the fractal dimension d_f,

$$\langle r^2(t)\rangle \sim t^{d_f}. \tag{5.5}$$

The MSD keeps increasing, and when the photons reach the end of the sample, at $Z = 9.275$ mm, it saturats.

The evolution of the Pólya number is depict at Fig. 5.6(c), for the experimental and simulation realizations. In the regular case, there is rapid growth and a saturation plateau. However, in the fractal case there is a similar behaviour at the start, but at a propagation length $Z = 3.875$ mm, which marks the onset of the fractal regime, there is a plateau. This anomalous transport behaviour of photons, typical of fractals, shows that when they reach some empty space, the probability starts to saturate, forming a plateau. However, they eventually find paths surrounding the voids and continue to propagate, what is reflected in the following growth in the Pólya number. When they have explored the entire sample, the Pólya number saturates, as expected.

5.4 Fractal photonic topological insulators

Recently, Biesenthal *et al.* have published an article were they show an experimental evidence that photonic lattices of helical waveguides, following a Sierpinski gasket geometry, host topological chiral edge states [84]. The work is supported by a theoretical tight-binding description, which corroborates their observations.

The system can be described by a coupled set of tight-binding equations

$$i\frac{\partial}{\partial z}\Psi_n = \sum_{<m>} ce^{i\vec{A}(z)\cdot\vec{r}_{mn}}\Psi_m, \tag{5.6}$$

where z is the optical axis, Ψ_n the electric field amplitude, c the strength of the hopping between NN which have a $\vec{r}_{mn}$ distance, and $< m >$ denotes summation over NN. The gauge vector potential $\vec{A}(z) = kR\Omega(\sin\Omega z, -\cos\Omega z)$ is induced from the driven periodicity, with k the wavenumber of the light, R the radius, and Ω the longitudinal frequency of the helix. By introducing this helix modulation of the waveguides, the system becomes topological [84]. The comparison between the eigenvalues corresponding to the trivial and topological fourth-generation Sierpinski triangle is depicted in Fig. 5.7. In the driven case, with $\vec{A}(z) \neq 0$, the mid-gaps become topological, hosting topological edge states. Colors are indicative of the topological nature, as they represent the real-space Chern number $C^{(rs)}$. Notice that for the static case, Fig. 5.7 (B), $C^{(rs)}$ is zero everywhere, in contrast to the driven case, Fig. 5.7 (F), where there are multiple regions with $C^{(rs)} \neq 0$. Specifically, the topological edge states with $C^{(rs)} = +1$ circulate counterclockwise along the outer boundary and for the ones with $C^{(rs)} = -1$, circulate in the opposite direction, along the inner edges.

Moreover, using laser-direct-written photonic waveguide lattices, they could observe the topological edge transport. In Fig. 5.8, the dynamics of these topological edge states is shown. The top row shows the position of the injected Gaussian broad beam and the lower shows the intensity output measured. The counterclockwise topological edge state propagating along the outer perimeter is shown in (A) to (F) by varying the starting position. Similarly, (G) to (J) exhibit the topologically protected edge state propagating clockwise along the inner boundary.

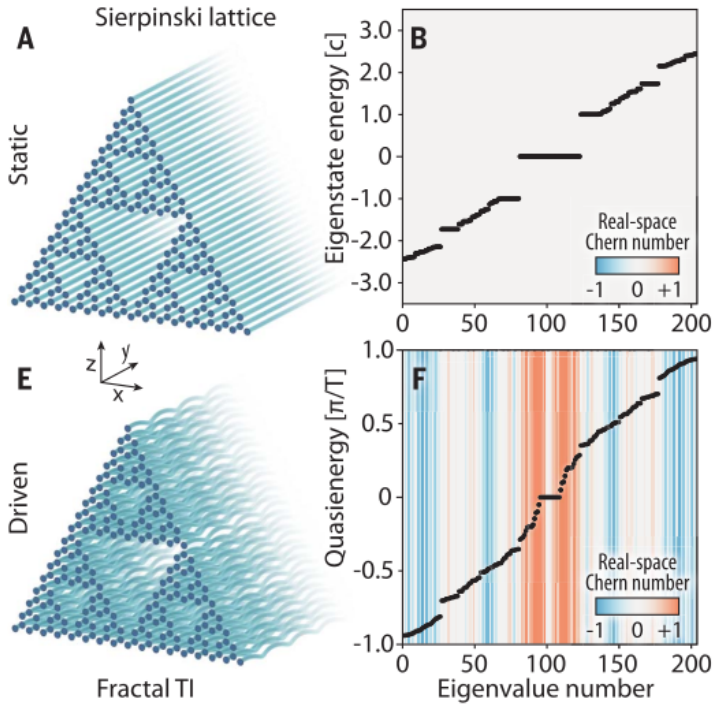

Figure 5.7: (A) Sierpinski lattice with static waveguides. (B) Eigenvalues corresponding to the static case, with $C^{(rs)} = 0$ everywhere. (E) Sierpinski lattice with helical waveguides. (F) Eigenvalues corresponding to the driven case, with $C^{(rs)} \neq 0$ in many regions. Figure reproduced from Ref. [84].

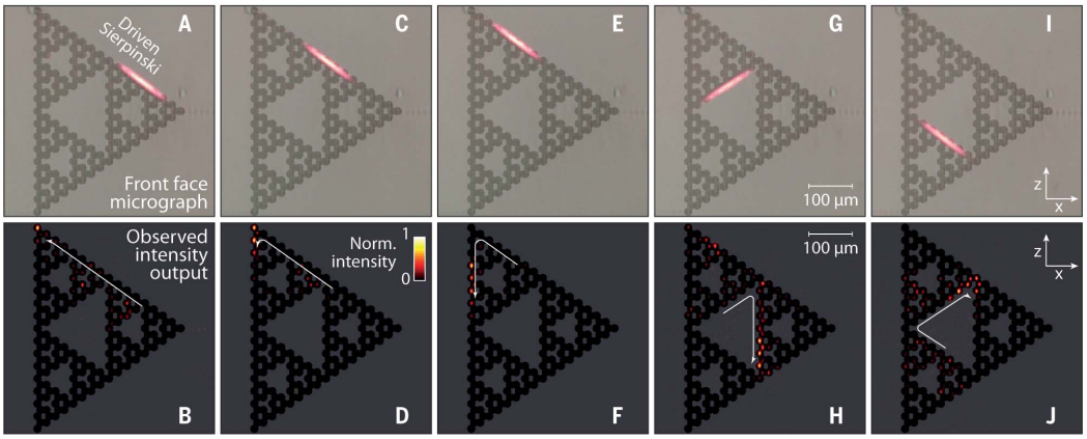

Figure 5.8: (A)-(F) depict the topological transport along the outer edge, by varying the initial position. (G)-(J) shows the inner edge state. Figure reproduced from Ref. [84].

5.5 Sierpiński Structure in Bi Thin Films on InSb Surfaces

In 2021, Chen *et al.* [8] have synthesized for the first time a material composed of a single element that has a lattice structure made of Sierpinski triangle islands. Previously, it was reported the fabrication of Sierpiński triangles supra-molecule on top of metal surfaces such as Ag [85], Au [86] and Cu [78]. The precious fractal structures formed were made of CO compounds, organic, metal organic, etc. [87]. The group of Jinfeng Jia [8] obtained this pattern formation by epitaxially growing monoatomic layers of Bi on top of the semiconductor InSb(111)B surface around 400 K. After cooling the system down, they performed STM measurements at liquid helium temperatures around 4 K, using a tungsten tip. The results are depicted in Fig. 5.9. Figures 5.9 (a) and (b) show the fractal structure of the lattice, with different Sierpiński triangles islands, and layers of Bi atoms. Figure 5.9 (c) shows a sketch of the different layers of the material, with the different colors and numbers indicated in (a) and (b). On top of the substrate, there is a wetting layer composed of Bi, Sb, and In atoms, which is denoted by level 0. On top of this, there is a 1-ML of Bi atoms forming the Sierpiński triangle-like level S_1. Next, there is level 2 labeling a 2-ML of Bi atoms, and on top there is the S_3 level, which is also a 1-ML of Bi atoms. Level 4 is expected to be a 4-ML of Bi atoms, and B corresponds to the highest level. The measurements shown in Figs. 5.9 (d), (e), and (f), correspond to the different color lines, which target different height profiles.

The interest in these structures is due to their fractal arrangement, combined with the large SOC exhibited by the Bi atoms. As we have discussed at the beginning of this chapter, the theoretical and experimental work by Reis *et al.* shows the appearance of topological states in Bismuthene like samples [6]. Therefore, the structures synthesised here are in principle prone to the detection of topological effects in a fractal.

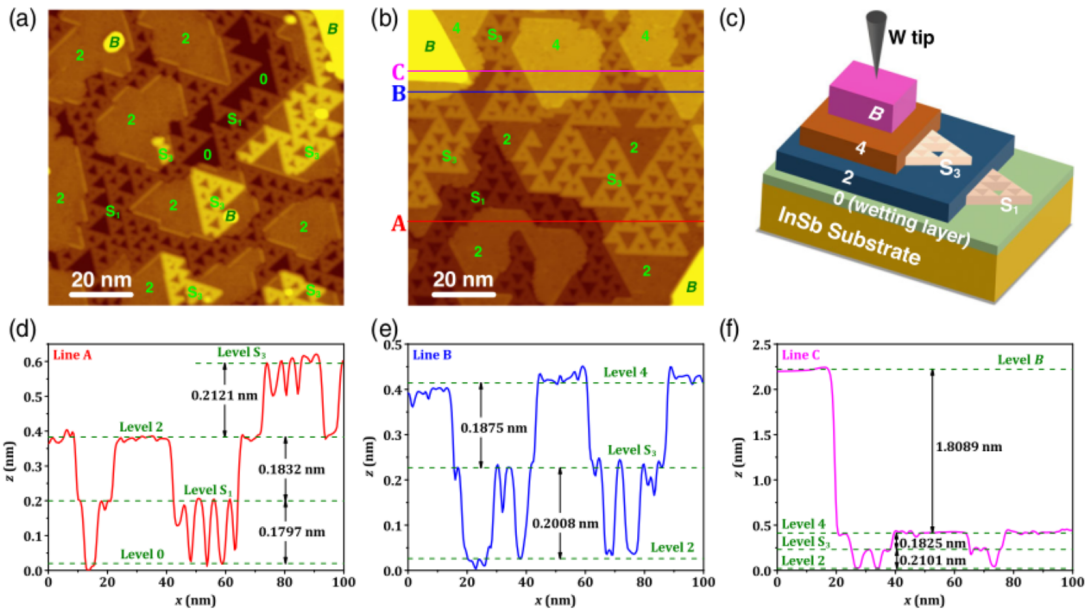

Figure 5.9: (a) and (b) STM images, where ST-like structure can be visualized. (c) Sketch of the levels appearing in the two previous samples. (d)-(f) Three different height profiles corresponding to the red, blue, and pink color lines. This figure has been reproduced from Ref. [8].

Figure 5.10 shows the measurement of the LDOS of a piece of the sample that is depicted at the lower right corner. A high population of electrons is labeled by the color pink, and the lighter is the blue, the less LDOS there is. The first row with LDOS taken at different bias

voltages shows that with increasing energy, the tunneling current is predominantly outside the Sierpiński triangle. The most interesting are the ones at the lowest row, from $E = 700$ mV to $E = 600$ mV. We highlight these three because there is a sharp pink edge along the boundaries of the Sierpiński triangles. Although they concluded in Ref. [8] that there were not topological phases, these highlighted measurements of Fig. 5.10 suggest that for this range of energy, there could be a topological state. Thus, this needs further investigation, which will be the aim of the next chapters.

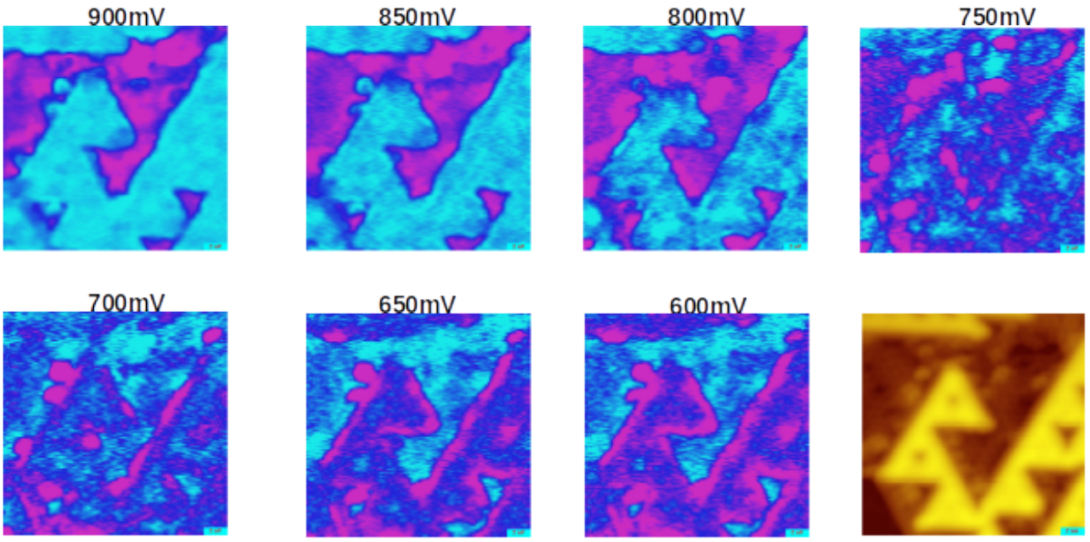

Figure 5.10: STM measurements for different bias voltage of the fractal sample depicted at the right bottom. Pink and light blue correspond to high and low LDOS, respectively. The image is a courtesy of the group of Jinfeng Jia.

Chapter 6

Muffin-tin method

Physics problems usually require a lot of simplifications because they tend to be very complex, as they involve many degrees of freedom. The behaviour of the electrons in a fractal lattice is not an exception. Nevertheless, the muffin-tin method is a simple approach that allows us to simulate artificial lattices, obtaining electronic properties such as the local density of states [78, 88].

The method is very similar to a particle in a box, as it consists of solving the one-electron time-independent Schrödinger equation, but with a specific potential landscape that confines the electrons. To reproduce the behaviour of the surface states, we approximate them as free particles, neglecting interactions that they could have among themselves and with the electrons of the bulk. They form a two dimensional free electron gas, which can move in the continuum set of points of the substrate. We want to restrict their motion to a certain geometry, since we are interested to know how they behave in that configuration. In our case, this is the Sierpiński triangle. A way to achieve this experimentally, is to put adatoms on top of the substrate, which can either attract or repeal the electronic cloud. Gomes *et al.* developed this method using CO molecules on top of Cu(111) [89]. When the adatoms surround the area of interest, their effective repulsive potential will scatter back the wave functions of the electrons, confining them as desired.

To better understand this procedure, let us look at the geometry in case, the Sierpiński triangle. The lattice is constructed considering that atoms are located at each vertex and center of the equilateral triangles that form the fractal, as shown in Figure 6.1.

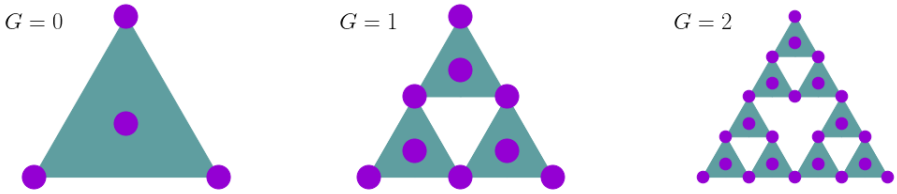

Figure 6.1: Building block of the Sierpiński triangle labeled by $G = 0$, followed by the first two generations. Purple dots correspond to the lattice structure.

Now, to enforce the electrons to move on the green area, a proper choice would be to place the adatoms on the adjacent sites of the white region, forming what we call the anti-lattice. The effective repulsive potential of an adatom is modeled as a square potential with radial symmetry,

$$V(r) = \begin{cases} v & \text{if } r < R, \\ 0 & \text{otherwise.} \end{cases} \tag{6.1}$$

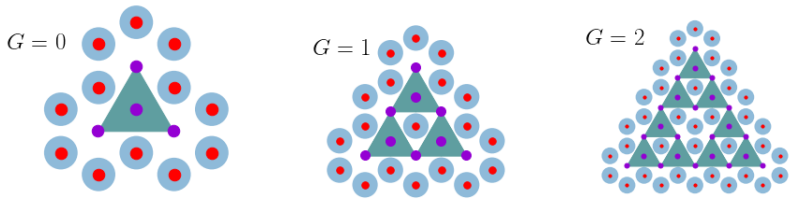

Figure 6.2: Building block of the Sierpiński triangle labeled by $G = 0$, followed by the first two generations. Purple dots correspond to the lattice structure and the anti-lattice is denoted by the red dots. The zone where the effective potential of the adatoms is nonzero is represented by a blue disk.

Kempkes *et al.* simulated an experimentally realized this fractal [78], as we have already discussed in section 5.2. Following their work, we first solved the eigenvalue problem of the two dimensional free electron gas with the patterned potential for any generation G,

$$\boldsymbol{H}_S\boldsymbol{\psi} = \left(-\frac{\hbar^2}{2m_e^*}\boldsymbol{\nabla}^2 + \mathbf{V}\right)\boldsymbol{\psi} = E\boldsymbol{\psi}. \tag{6.2}$$

Since going to higher generations does not change much the LDOS due to the self similarity, and only increases the computation time, as the lattice grid needs to be increased, we will restrict to the lower generations. To diagonalize the Hamiltonian of the one-electron time-independent Schrödinger equation, we need to discretize our space. If we define a square box of n points in each direction, linear operators are mapped to (n^2, n^2) square matrices, and wavefunctions to n^2 vectors. In one dimension (setting a constant increment Δx between all points), the first-and second-order derivatives at site x_i are approximately given by

$$\psi'(x_i) = \frac{\psi(x_{i+1}) - \psi(x_{i-1})}{2\Delta x}, \quad \psi''(x_i) = \frac{\psi(x_{i+1}) - 2\psi(x_i) + \psi(x_{i-1})}{\Delta^2 x} \tag{6.3}$$

for $n = 2, ..., n-1$ and therefore, we can rewrite it in matrix notation as

$$\boldsymbol{\mathcal{D}_x} = \frac{1}{2\Delta x}\begin{pmatrix} 0 & 1 & 0 & \cdots & 0 \\ -1 & 0 & 1 & \ddots & \vdots \\ 0 & \ddots & \ddots & \ddots & 0 \\ \vdots & \ddots & \ddots & \ddots & 1 \\ 0 & \cdots & 0 & -1 & 0 \end{pmatrix}, \quad \boldsymbol{\mathcal{D}_x}^2 = \frac{1}{\Delta^2 x}\begin{pmatrix} -2 & 1 & 0 & \cdots & 0 \\ 1 & -2 & 1 & \ddots & \vdots \\ 0 & \ddots & \ddots & \ddots & 0 \\ \vdots & \ddots & \ddots & \ddots & 1 \\ 0 & \cdots & 0 & 1 & -2 \end{pmatrix}. \tag{6.4}$$

The derivatives at the end points need to be treated differently. Thus, we approximate them as

$$\begin{aligned} \psi'(x_1) &= \frac{\psi(x_2) - \psi(x_1)}{\Delta x}, & \psi'(x_n) &= \frac{\psi(x_n) - \psi(x_{n-1})}{\Delta x}, \\ \psi''(x_1) &= \frac{\psi(x_3) - 2\psi(x_2) + \psi(x_1)}{\Delta^2 x}, & \psi''(x_n) &= \frac{\psi(x_n) - 2\psi(x_{n-1}) + \psi(x_{n-2})}{\Delta^2 x}. \end{aligned} \tag{6.5}$$

If we go to two dimensions, each point of the grid can be written as $x_{ij} = i\Delta x + j\Delta y$, with $i, j = 1, ..., n$, and the Laplacian becomes $\nabla^2 = \partial_x^2 + \partial_y^2 = I_n \otimes \boldsymbol{\mathcal{D}_x}^2 + \boldsymbol{\mathcal{D}_y}^2 \otimes I_n$, since our wave

function is the vector

$$\boldsymbol{\psi} = \begin{pmatrix} \psi(x_{11}) \\ \psi(x_{21}) \\ \vdots \\ \psi(x_{n1}) \\ \psi(x_{12}) \\ \vdots \\ \psi(x_{nn}) \end{pmatrix}.$$

Similarly, the potential V is mapped to a matrix where the entries ij are all zero, unless the coordinate x_{ij} is inside the disk defined before at Eq. 6.1. When diagonalizing the Hamiltonian, we set a cutoff to the number of eigenvalues and eigenvectors that we want to obtain. As we are interested in the low-energy spectrum, we solve only for the m smallest values. By restricting this set and using sparse matrix, the computation time is highly reduced.

After obtaining the set of energies and waves functions, we compute the local density of states. This gives a measure of how the electronic cloud of the substrate is distributed, enabling us to compare it with images obtained with an STM. The LDOS is given by

$$LDOS(\epsilon - \epsilon') = \sum_{\epsilon'} |\boldsymbol{\psi}_{\epsilon'}(\boldsymbol{x})| \delta(\epsilon - \epsilon') \approx \sum_{\epsilon'} |\boldsymbol{\psi}_{\epsilon'}(\boldsymbol{x})| \frac{b}{(\epsilon - \epsilon')^2 + (\frac{b}{2})^2}, \tag{6.6}$$

where we replaced the delta function by a Lorentzian $L(\epsilon - \epsilon')$ with broadening b. This is necessary because states with energy ϵ' are broadened due to electron-electron and electron-phonon scattering. Thus, the finite lifetime excitations also contribute to the tunneling current measured by the STM [78].

6.1 Comparison with literature

In order to check whether the program written for the simulation was correct, we first focused on reproducing the results published by S. Kempkes *et al.* [78]. To do so, we solved the Schrödinger Eq. (6.2) for the first generation of the Sierpinski triangle using the same parameters. The shape of the potential used is the muffin-tin, defined at Eq. (6.1), with a height of $v = 0.9$ eV, and the radius of scatterers equal to $R = 0.3$ nm. As this refers to a free electron gas on top of Copper, we used an onset energy of $u_s = 0.45$ eV, a lattice parameter of $a_0 = 1.1$ nm, and an effective electron mass $m_{eff} = 0.42$.

In Fig. 6.3, we show the comparison of the LDOS of a free electron gas confined to the first generation of the Sierpinski triangle. In Fig. 6.3 (a) we show the results from Ref. [78] and in Fig. 6.3 (b) our own results. Here, we will limit to discus the main differences, while arguing which might be the reasons for them. The plots are going to be discussed in more depth later.

We noticed that the LDOS is very sensitive to how it is computed. Mathematica is a black box, you do not know which subroutine they used for obtaining the eigenvalues and eigenvectors, and in our case we developed a code in Python. Because of that, there are a few parameters such as the discretization of the box, the number of eigenvalues computed, or the amount of free space surrounding the Sierpinski triangle that could be different. Therefore, this could change slightly the results. In addition, we observed that the numerical error due to the scatterers position could be a source to these differences. When the same simulation is preformed, but with a rotation of some angle, the LDOS curve changes. Moreover, there is always a difficulty in choosing exactly the center of the site, the point in which we are interested. Just a small shift by a grid point can lead to different results. However, the main features and trends remain the same, and when you map the LDOS to the two dimensional sample, at the

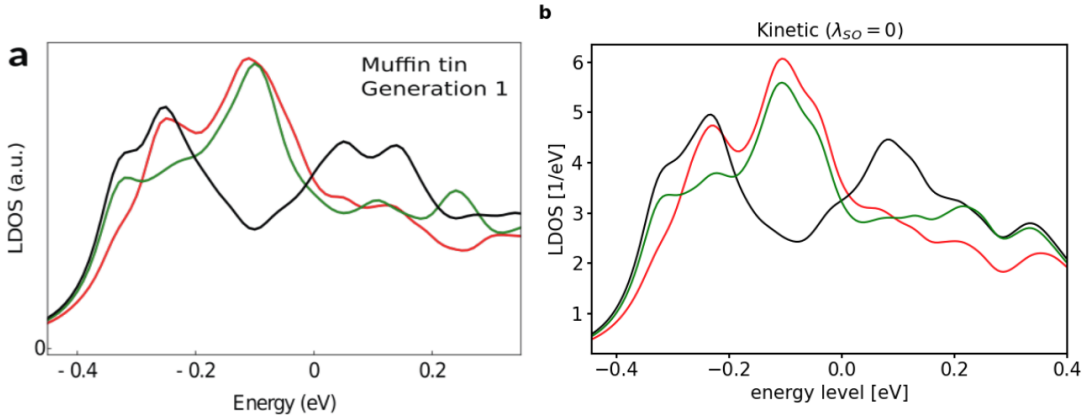

Figure 6.3: Comparison of the LDOS with Kinetic contribution for G=1. (a) Results taken from Kempkes *et al.* [78]. (b) Our own calculations.

same energy values, both results are indistinguishable.

In Fig. 6.4, we show the effect of the grid resolution and the number of waves used in the simulation. Mainly, one can observe from top left to right bottom, that the range of energy is linearly proportional to the number of waves. Furthermore, the grid resolution also changes a bit the LDOS, but it is more redundant. Lastly, as the height of the LDOS is related to the probability, when there are more states the peaks decrease.

There are only three different lines, although the first generation has nine sites. This is due to the self-similarity of the fractal. Each site is assigned to a color that reflects its connectivity. Red has one nearest-neighbour, green has two, and black has three. Due to this C_3 rotational symmetry of the lattice, all sites with the same number of neighbours show a similar LDOS, with a minimal difference that comes from numerical precision. To avoid this difference, the mean of all sites of same colour are computed. The key features can be seen by focusing on the lowest range of energy. The LDOS starts populating first the black site. At $E = -0.325$ eV, all sites have a similar weight, in a bulk configuration. At $E = -0.2$ eV, the red and green are more intense than the black. This intensifies with increasing energy and at $E = -0.1$ eV, the red and green sites have a high peak, while the black has a dip. This is characteristic of a non-bonding configuration. Electrons at this energy would need to hop through next NN because the black sites have a minimum. After this, the LDOS of the sites that were in a peak start decreasing, and the black sites increase, till reaching the peak at $E = 0.1$ eV.

In Fig. 6.6, we show the LDOS heatmap along the edge of the Sierpinski for the same parameters used before, for all the energy range. High LDOS intensity is labeled with brighter colors and low intensity with darker colors. The path taken is reflected on the x-axis as shown in Fig. 6.5 by the x coordinate of the line connecting the center of the red site at the bottom left corner, till the center of the top red site. Below zero, there is a horizontal yellow line around $E = -0.3$ eV, which corresponds to the bulk phase, with all sites exhibiting a similar LDOS. Then, around $E = -0.1$ eV, there are two darker holes, corresponding to the non-bonding configuration. Although at higher energies there are horizontal yellow lines, signaling what could be an edge state, when looking at the two dimensional map we observe that the LDOS is high everywhere.
In this section, we will not analyze in detail what happens at higher energies, which correspond to higher orbitals. Here, we concentrate on obtaining results using the same parameters as in Ref. [78], and showing that the LDOS is very similar, although the method used leads to slightly modified curves. In the next section, we will map the LDOS to the two dimensional lattice in more detail.

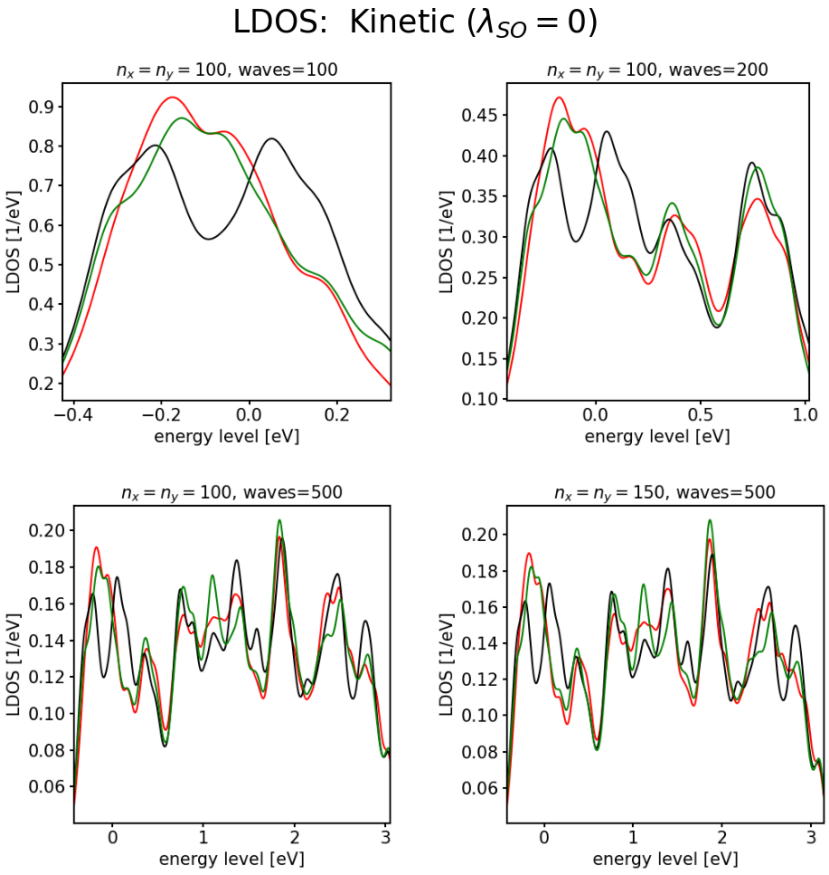

Figure 6.4: LDOS computed for the red, green, and black sites of the $G = 1$ Sierpiński triangle, with only the kinetic energy contribution, for different values of grid discretization and number of eigenvalues. A lattice parameter of $a_0 = 1.1$ nm, a potential height of $v = 0.9$ eV, and scatterers with $R = 0.3$ nm are used.

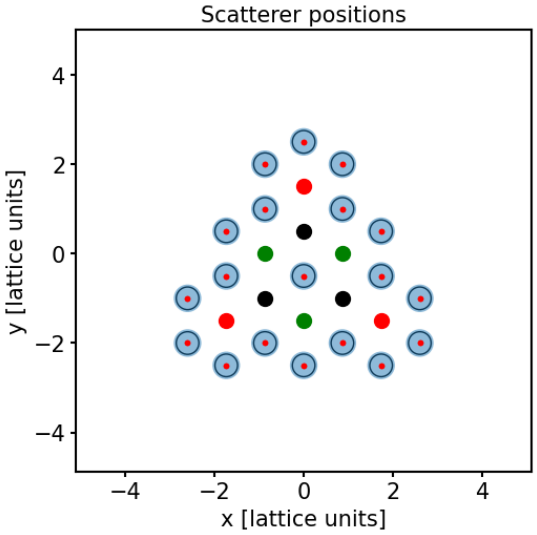

Figure 6.5: Simulation box. Scatterers placed at the anti-lattice are represented by a blue disk with a red center, which is the zone of non-zero muffin-tin potential. Red, green, and black dots label the sites for the Sierpinski triangle, with connectivity one, two, and three, respectively.

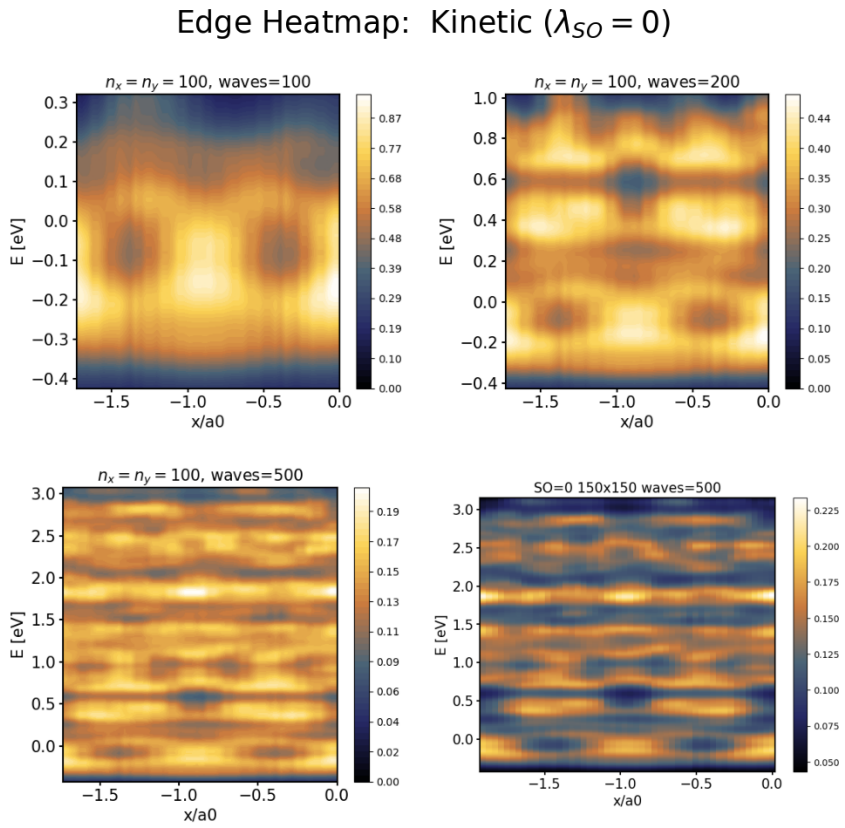

Figure 6.6: Kinetic heatmap of the LDOS along the left edge of the Sierpiński, for different values of grid discretization and number of waves. Each horizontal slice corresponds to a configuration and the x-axis labels the coordinate along the edge. The color bar reflects the intensity of the LDOS.

Chapter 7

Theoretical results

This chapter contains the main results of this thesis, which are the effects of the spin-orbit coupling when a two-dimensional free electron gas is confined in a Sierpinski triangle. For a better comparison we first show the kinetic contribution alone, and then we include the spin-orbit coupling. Afterwards, we will consider the third generation to acquire a better understanding. Finally, we will replace the muffin-tin with a Gaussian potential and see which new features emerge.

7.1 First generation Muffin-tin results

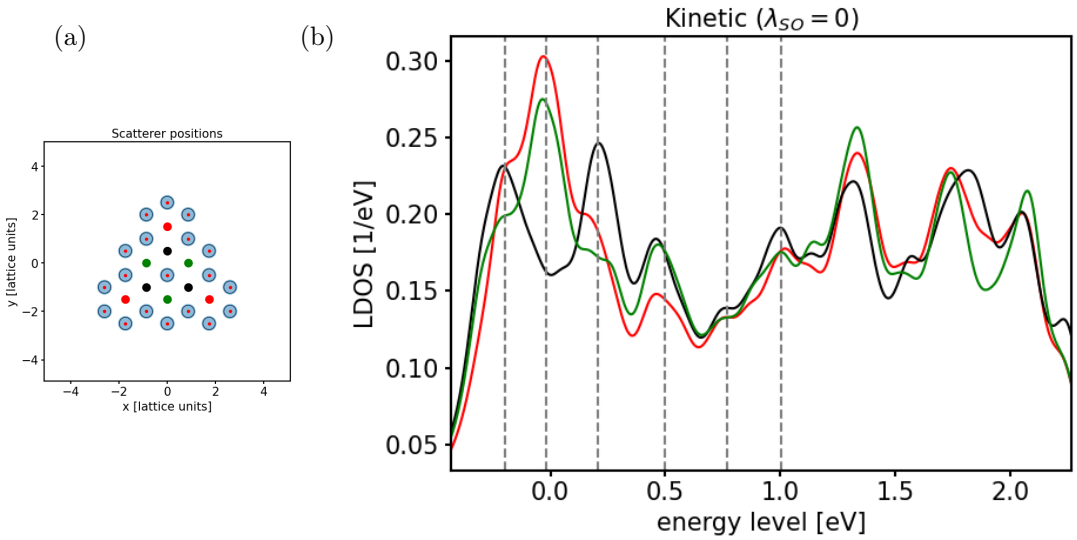

Figure 7.1: (a) Simulation box. Scatterers placed at the anti-lattice are represented by a blue disk with a red center, which is the zone of non-zero muffin-tin potential. Red, green, and black dots label the sites for the Sierpinski triangle, with connectivity one, two, and three, respectively. (b) LDOS for all different sites. Dashed lines represent the energies used in Fig. 7.2.

In Fig. 7.1(a), the blue dots denote the region where the muffin-tin potential is non-zero, while the red, green, and black dots label the sites of the Sierpinski triangle. The results shown in Fig. 7.1(b) are very similar to the ones shown in the previous chapter. We have changed the lattice parameter, the box dimensions, the resolution, and the wavefunctions. For the remaining of this work, we will set the lattice parameter $a_0 = 1$ nm, which only shifts

the peaks by 0.1 eV. Observe that now, the maximum of the red and green sites are around $E = 0$ eV and not $E = -0.1$ eV. The space between the outer scatterers and the boundary of the square box is set to $2.5 \cdot a_0$ nm, in the abscissa and ordinate axes. If we would not have enough space, the boundary would had influenced the LDOS inside the Sierpinski. For this simulation, the grid resolution is $n_x = n_y = 80$, and the number of waves is 500. The rest of the parameters is kept the same, $m_{eff} = 0.42$, $u_s = 0.45$ eV, $v = 0.9$ eV, and $R = 0.3$ nm.

The vertical dashed lines in grey represent the first interesting values of energies, which are mapped to the Cartesian plane in the next figure. Between these lines, the system is evolving from one configuration to another, having a less defined LDOS map along the sample. We have already mentioned the first three LDOS that can be clearly distinguished. A first peak at $E = -0.198$ eV for the red and black sites, with less population at the green site. We can already see the tendency of the wavefunctions to split into self similar parts, as it is happening for the green site. At $E = -0.017$ eV, there is the mentioned non-bonding configuration, and at $E = 0.208$ eV the black sites acquire a larger LDOS, while the red and green sites have the LDOS more towards the boundary, with a node between the black and red sites.

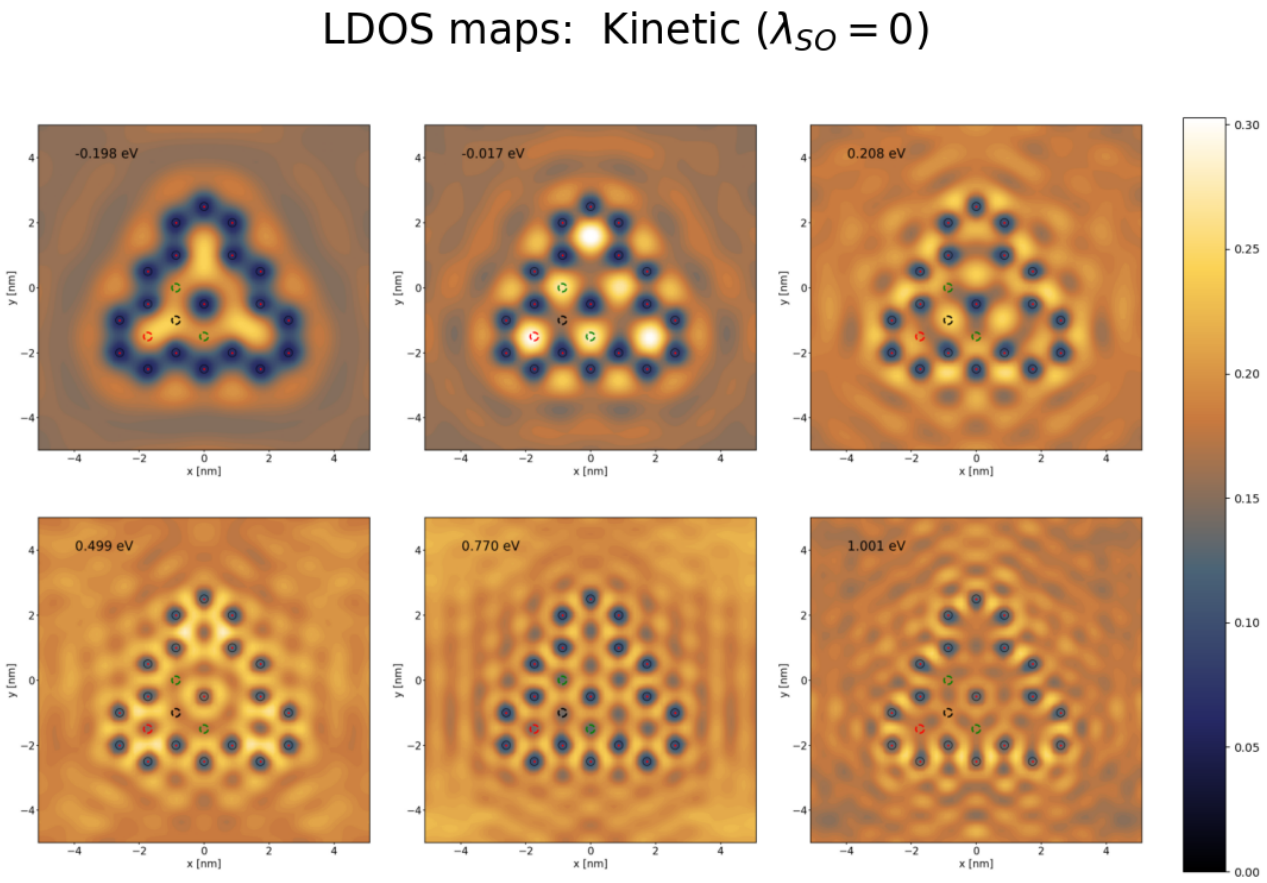

Figure 7.2: Map of the LDOS to the two dimensional lattice. From top left to right bottom, the figures correspond to the selected values of energy from figure 7.1. The maximum of the color bar has been set equal to the LDOS peak of the red site.

To investigate the next three configurations, it is better to focus on figure 7.2 because

when electrons go into higher orbitals, the center of the site is not as representative as when we are looking at s orbitals (as we did before). When the height of the LDOS of the three sites with different colors are around half of the intensity of the highest red peak, we observe configurations with nodes at each site, with occupation around them. For a bias voltage of $E = 0.499$ eV, there is a clear node surrounded by a high value of LDOS at each red site. The green and black sites are forming together a circular node, surrounding the central scatterer. However, one can already observe the beginning of the formation of a perfect honeycomb, which is well formed at energies $E = 0.770$ eV. There are nodes centred at each lattice position, and the LDOS is in between them. For the last selected value, at $E = 1.001$ eV, the LDOS is a bit low, but we can see that a node is forming in between two NN's, and the LDOS is at the remaining space. The black sites have clearly three nodes around them, while the green have two and the red has one. Configurations with a node at the sites are p-wave like, whereas the ones with a node between the sites correspond to even higher orbitals.

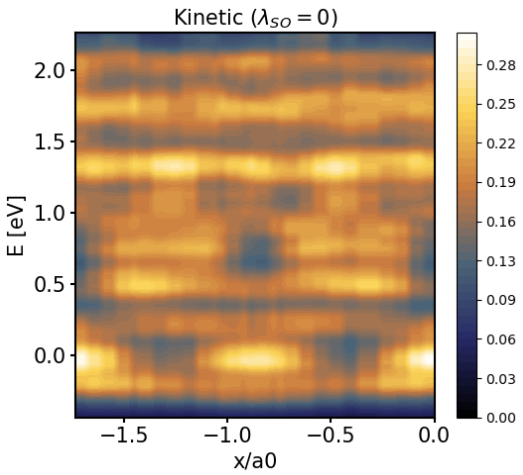

Figure 7.3: Kinetic heatmap of the LDOS along the left edge of the Sierpiński, following a straight line connecting the two red sites at the corners..

A way to detect an energy where it could be an edge state, is by plotting the LDOS along an edge for a certain range of energy. This is what is done in Fig. 7.3. The path chosen connects the red sites at the corners of the left edge. Around zero energy, we can see the lobes corresponding to the non-bonding configuration. Although there seems to be yellow horizontal lines above and below zero energy, there is no clear edge state, as at these energies there is weight also inside the triangles.

After this first section, where we have studied the confinement of a free electron gas by a muffin-tin potential patterning the anti-lattice, we move to one of the main questions of this thesis. How is the effect of the SOC interaction in a fractal? Does it open topological gaps, and drive matter to topological phases, hosting edge states or corner states? To answer these questions, we follow the same procedure as before, but now we will include the SOC term given by Eq. (4.14) into the Schrödinger equation. Hence, we need to solve the eigenvalue equation

$$\boldsymbol{H}\boldsymbol{\psi} = \left(-\frac{\hbar^2}{2m_e^*}\boldsymbol{\nabla}^2 + \lambda_{SO} \cdot \frac{\hbar^2}{(2m_e^* c)^2}(\boldsymbol{\nabla}\varphi \times \boldsymbol{p}) \cdot \boldsymbol{\sigma} + \mathbf{V} \right) \boldsymbol{\psi} = E\boldsymbol{\psi}. \tag{7.1}$$

The parameter λ_{SO} has been introduced to represent the strength of the SOC. The value has been set to $\lambda_{SO} = 1 \cdot 10^6$, such that the kinetic and SOC terms have the same order of magnitude. Hence, the SOC effect is going to be relevant enough, and we will be able to observe which changes it might produce.

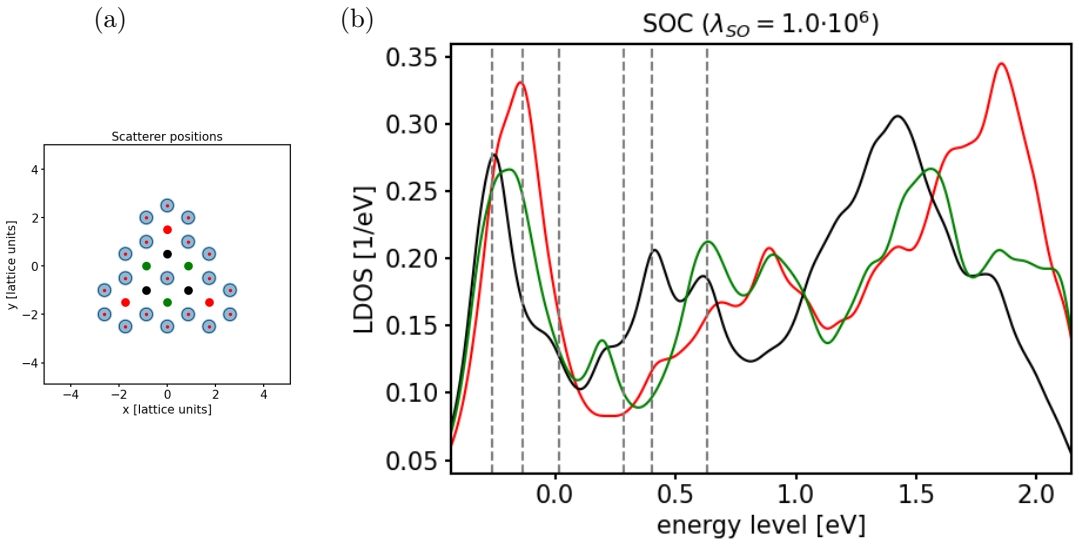

Figure 7.4: (a) Simulation box. The scatterers placed at the antilattice are represented by a blue disk with a red center, which is the zone of non-zero muffin-tin potential. Red, green, and black dots label the sites for the Sierpinski triangle with connectivity one, two and three, respectively. (b) LDOS for all different sites. The dashed lines correspond to selected energies in Fig. 7.5 for which the full LDOS will be shown.

In figure 7.4(a), we can see the anti-lattice of the first generation, and in Fig. 7.4(b) the LDOS. As before, we have selected a few interesting values of energy (see dashed lines). By looking at the shape of the lines, we can already see that some features have completely changed. First, the original peaks have been shifted to lower energies. The black line now has only one peak at low energy. In addition, the first configuration at $E = -0.264$ eV looks more like a bulk phase, as all different sites have a similar LDOS weight. Then, we can see how the SOC has turned off the non-bonding configuration: the green site became a bit more different than the red site, while the black one continues to have the lowest LDOS. Thus, the SOC has destroyed the non-bonding phase, producing an isolated corner state at $E = -0.133$ eV.

For the following values of energy, is better to look directly at the LDOS maps shown in figure 7.5, since the LDOS is very low at each site. At $E = 0.032$ eV, a high (white) LDOS intensity appears surrounding the scatterers of the outer perimeter. For this bias voltage, it seems that the SOC is producing a high LDOS at the region were the gradient of the potential is higher. In a real material, we can imagine that one has an approximate constant potential at the bulk. When one approaches the edge of the sample, there is a huge change in the potential because we need to connect with the vacuum. Hence, the boundary is where the gradient of the potential is stronger, and therefore we can think that this phase, which has all the LDOS surrounding the lattice, is an edge state, with no population at the lattice. For the next value of energy, at $E = 0.283$ eV, the same feature appears, but now at the inner boundary: there is an edge state along the inside perimeter. For $E = 0.403$ eV, the image is similar to the last image obtained including only the kinetic term. However, now the nodes are located at each red and green sites, while the triangular shape at the black site is much brighter. For the last selected value, $E = 0.629$ eV, the LDOS is mainly occupying the space in between the red and black sites.

For the LDOS at the edge, which is shown in figure 7.6, we will focus mainly on the lower-energy behaviour. Around $E = 0$ eV, the three lobes have been converted into a straight line. The brighter spots towards the ends of the line correspond to corner states. Upon increasing energy, an LDOS gap is opened, since there is an edge state along the outer and inside perime-

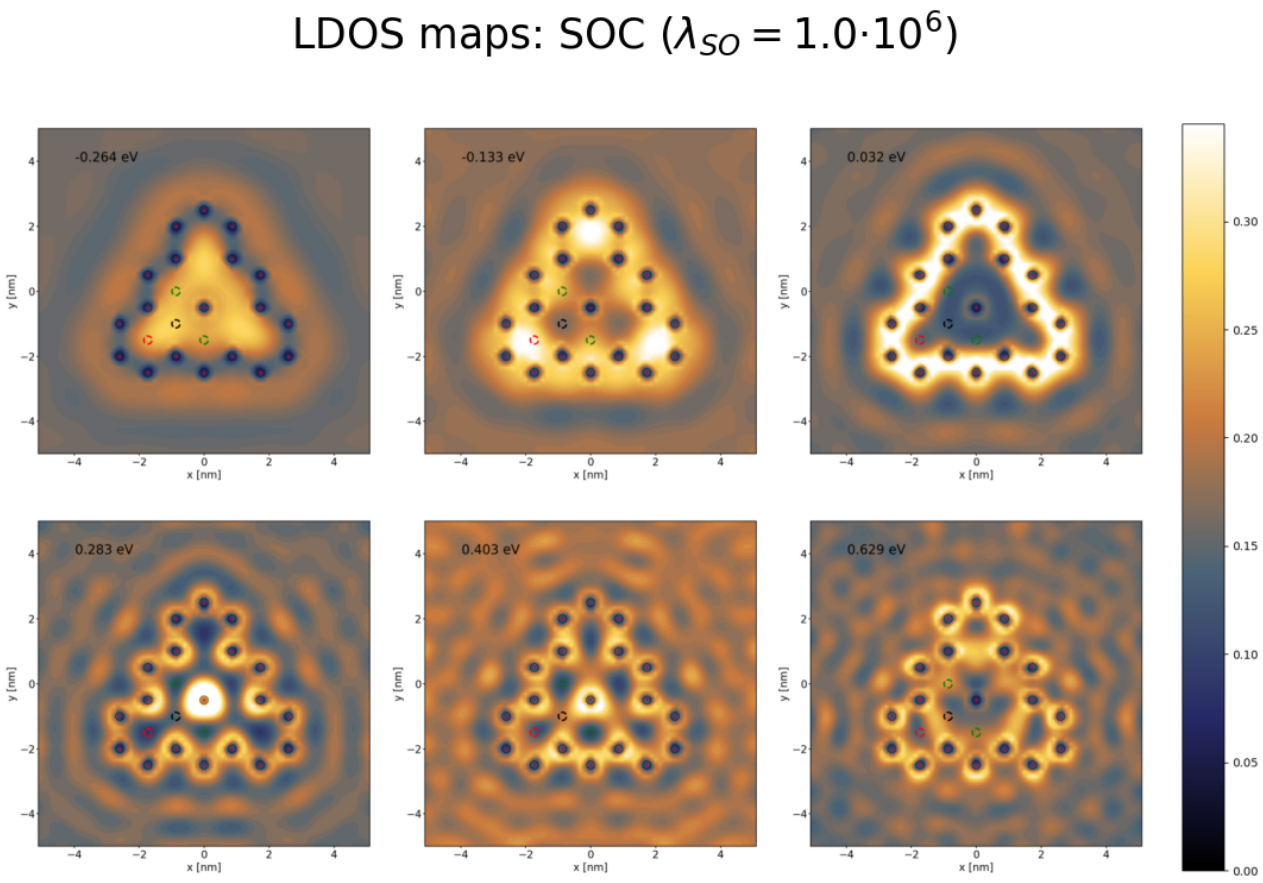

Figure 7.5: LDOS map of the first generation of the Sierpiński triangle at the selected energy values. These solutions include the SOC term with a strength of $\lambda_{SO} = 1.0 \cdot 10^6$. The maximum of the color bar has been set equal to the highest red peak at $E = -0.133$ eV.

ters, while there is no LDOS weight at the lattice.

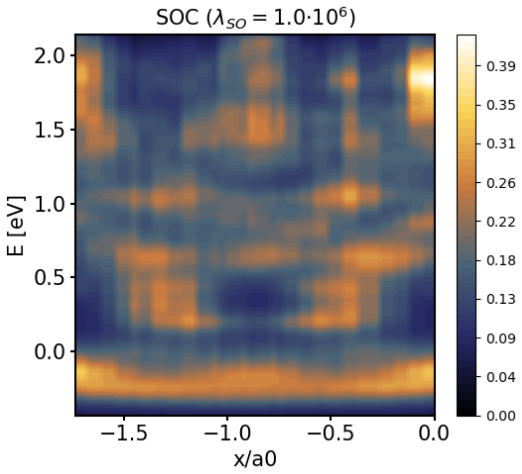

Figure 7.6: Heatmap of the LDOS along the left edge of the Sierpiński following a straight line connecting two red sites at different vertices, including the SOC.

Figure 7.7 shows, for each type of (black, green, and red) site, the trend of the LDOS for different values of the intrinsic SOC parameter λ_{SO}. All sites show a similar behaviour, but the position and intensity of the peaks changes slightly. Generally, we see how the SOC is opening a gap in the LDOS in between the two peaks at low and high energies. Although we are not considering here those high energies corresponding to higher-order orbitals, it is worth mentioning the general trend. In addition, in between these two peaks there is a another one, which has a much lower LDOS. Observe that the energies at which these three peaks appear follow a trend in decreasing order of connectivity: they appear at lower energies for the black sites, which have higher connectivity, then for the green, and finally the red. These features are intensified when we increase the value of the parameter λ_{SO}.

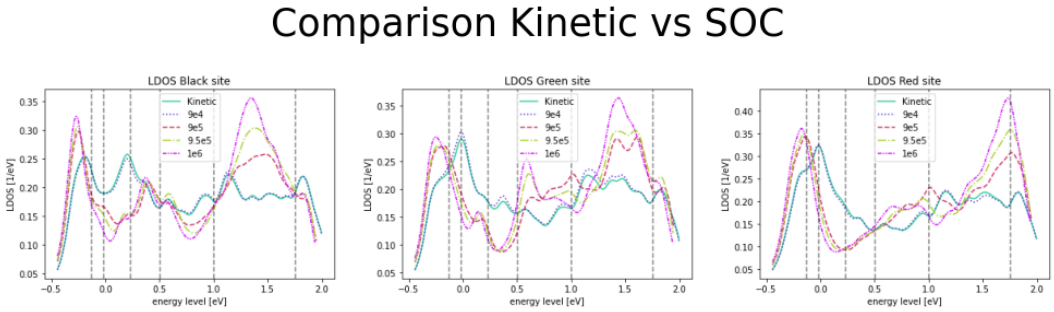

Figure 7.7: LDOS comparison for simulations with different value of λ_{SO}, at each site.

7.2 First generation Gaussian results

In this section, we consider again the same system, the first generation of a Sierpiński triangle, but now we replace the shape of the muffin-tin potential by a Gaussian function. The reason to do this is the abrupt change of the muffin-tin potential at the boundaries. It jumps from 0 to v, exhibiting an infinite derivative at a distance R from the scatterer center. The smoothness of the Gaussian potential gradient will be reflected in the LDOS, allowing for more resolution in between the phases, therefore revealing new interesting states.

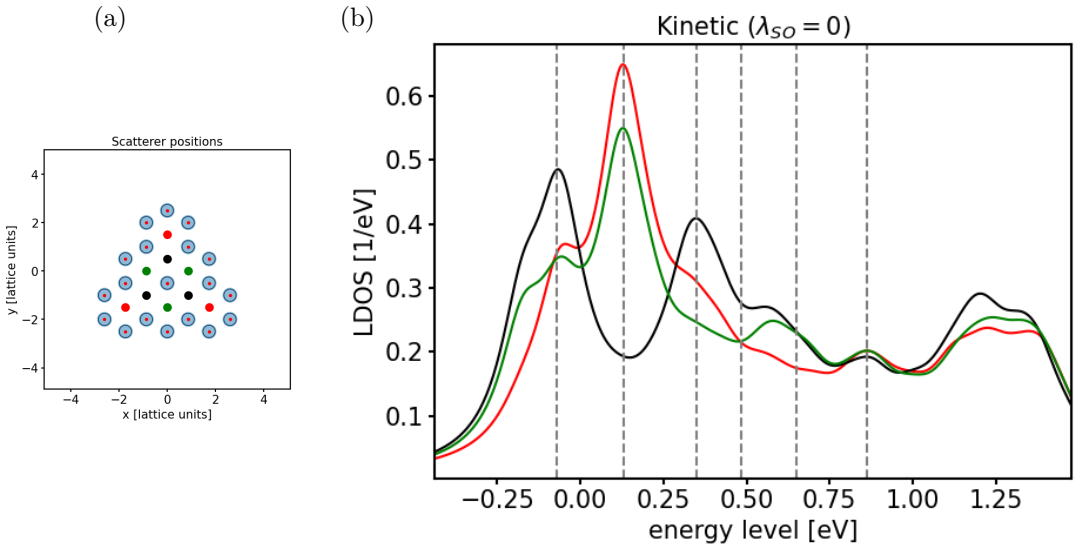

Figure 7.8: (a) Simulation box. The FWHM of the Gaussian potential is given by the blue disk diameter encircling a red dot. Red, green, and black label the sites for the Sierpinski triangle with connectivity one, two, and three, respectively. (b) LDOS for all different sites. Dashed lines correspond to selected the energies at which the LDOS maps will be shown in Fig. 7.9.

The results shown in figure 7.8 are structured as before. The Gaussian potential is represented by blue circles centered at red dots and electronic sites are shown in red, black and green (left figure), ($\lambda_{SO} = 0$). The diameter of the blue circle has been used to set the Full Width at Half Maximum (FWHW), hence defining the variance of the distribution. The LDOS shows the characteristic features of the kinetic term that we commented at the beginning of the chapter. To avoid repeating the same, we are going to directly discuss figure 7.9, where one can see the LDOS for the six values of energy represented by dashed lines in figure 7.8. However, before doing so, it is worth noticing that despite exhibiting the same trend, the peaks are shifted and at higher energies they are less pronounced.

The main difference when one compares the Gaussian and muffin-tin results is that now, the red peak that sets the color bar range is much higher for the Gaussian potential. This is because the range of energy now is smaller, which happened in spite of keeping the grid resolution, $n_x = n_x = 80$, and the number of waves= 500 constant. This shift in the color is the reason why at low energies the configurations are much sharper and well defined. As a consequence, at higher energies they appear less populated, and seem to not be as relevant. The first three plots are very similar to the results obtained using the muffin-tin potential. For the last three plots, we choose first $E = 0.485$ eV to show how the LDOS is decreasing. Then, we consider the configuration at $E = 0.650$ eV, where there is a node at the red site, and a ring of nodes surrounding the central scatterer. The last one, at $E = 0.861$ eV, was already seen with the muffin-tin results: there is a high intensity surrounding all sites at which one

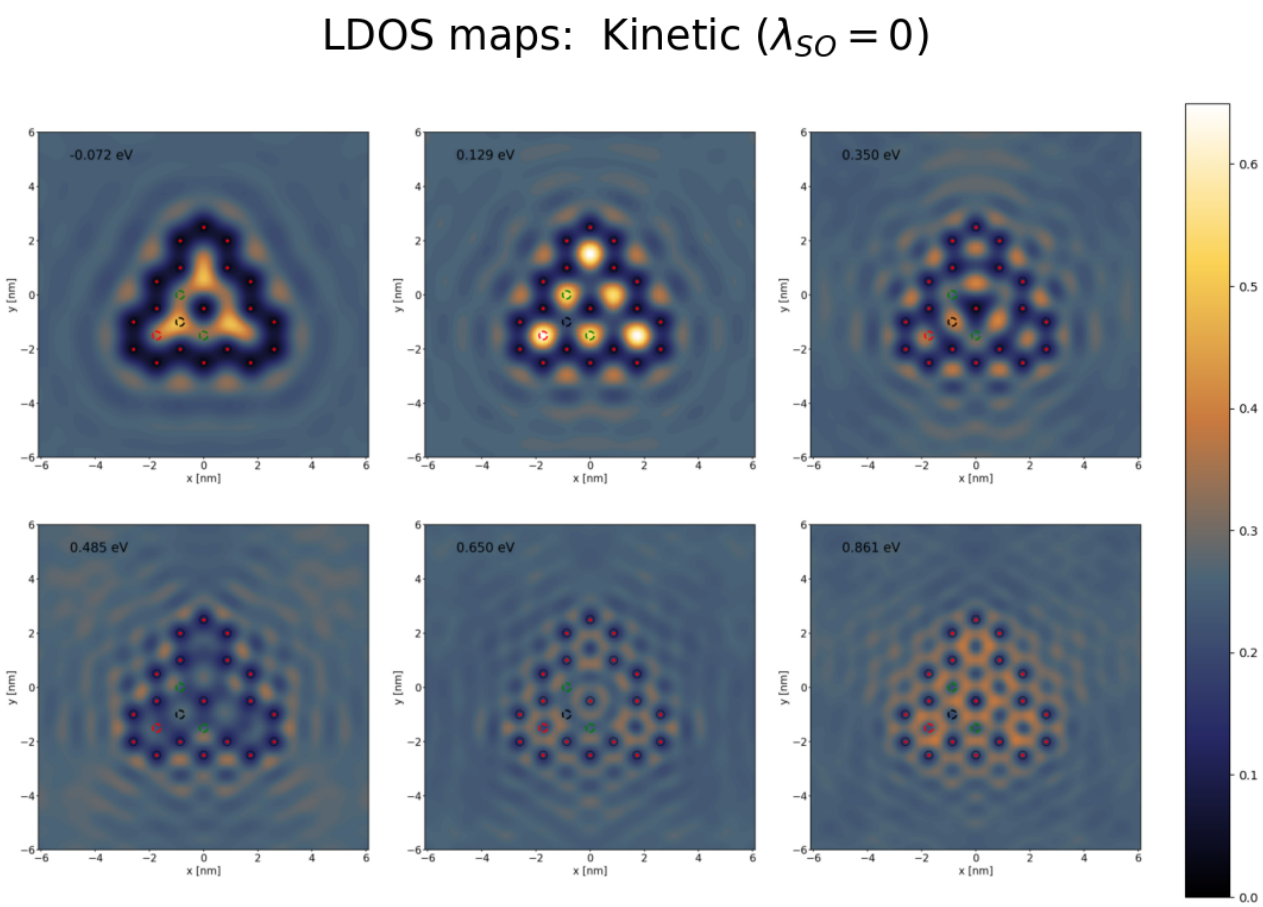

Figure 7.9: Map of the LDOS for the 1st Sierpiński structure. From top left to right bottom, the figures correspond to the selected values of energy shown in figure 7.8. The maximum of the color bar has been set equal to the LDOS of the highest red peak.

observes the nodes.

The LDOS along the edge shown in figure 7.10 exhibits the same features as before, but much sharper. Mainly, we see a straight line slightly below zero energy corresponding the phase at $E = -0.072$ eV of Fig. 7.9, with less LDOS at the green site, and between $E = 0$ and $E = 0.25$ eV there are three ellipses with a high LDOS (light color) characteristic of the non-bonding configuration.

We have seen that the Gaussian results are not much different from the muffin-tin when we consider only the kinetic term. However, the differences are much more relevant when we include the SOC with λ_{SO} finite, see Figs. 7.11 and 7.13. The selected phases to depict the Gaussian potential LDOS maps are the same ones that we showed before in Fig. 7.2. We see in Fig. 7.11 again the two main effects, namely the breaking of the non-bonding phase and the appearance of the corner state, which is now much clearer because the difference of the LDOS between the red and the other sites has increased. The scan maps of the LDOS at the selected energy values are shown in figure 7.13. At $E = -0.142$ eV, there is a peak at the black and at the green, and the lowest intensity is the red. As expected, we can see three small self-similar triangles, with a bright region centered at the black site. At $E = -0.076$ eV, the LDOS is

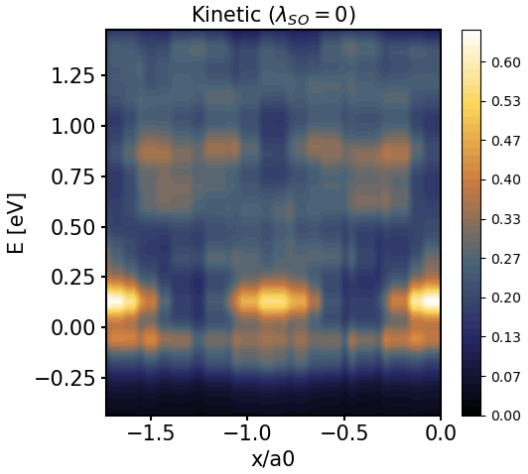

Figure 7.10: Heatmap of the LDOS along the left edge of the Sierpiński following a straight line connecting two redsites for the Gaussian potential.

nearly equal at each site, since this is a bulk configuration. Afterwards, the LDOS spreads towards the edge of the lattice. It looks like an edge state (now centered at the boundary sites) that has a bit more occupation at the corner. This trend continues, the population at the green site keeps decreasing, till the corner state is isolated at $E = 0.049$ eV. Then, at $E = 0.210$ eV we find an edge state as before, along the outer perimeter. Lastly, at $E = 0.275$ eV, the LDOS goes to a minimum at each site, and there is a high intensity surrounding the green node.

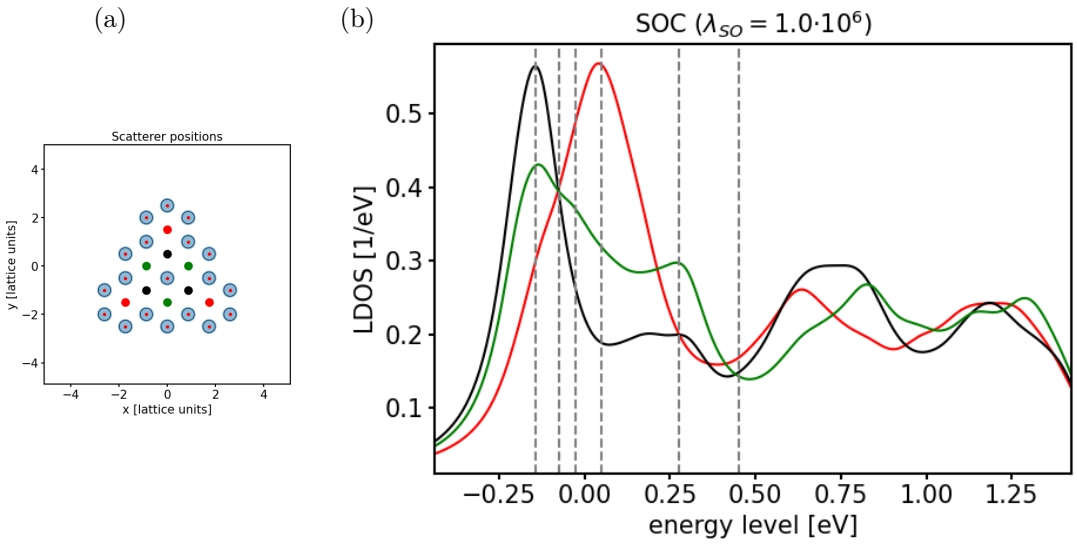

Figure 7.11: (a) Simulation box. The FWHM of the Gaussian potential is given by the blue disk diameter encircling the red dot. Red, green, and black label the sites for the Sierpinski triangle with connectivity one, two, and three, respectively. (b) LDOS for all different sites when including the SOC term. The dashed lines correspond to selected energies.

Inspection of the LDOS along the edge, shown in figure 7.12, reveals similar features as before, but now the straight line is more defined and the corner modes at the end are more pronounced. After a gap around $E \sim 0.5$ eV, there are yellow circles around $E = 0.75$ eV, which are a similar state to what we found with the muffin-tin potential, figure 7.5, at $E = 0.403$ eV.

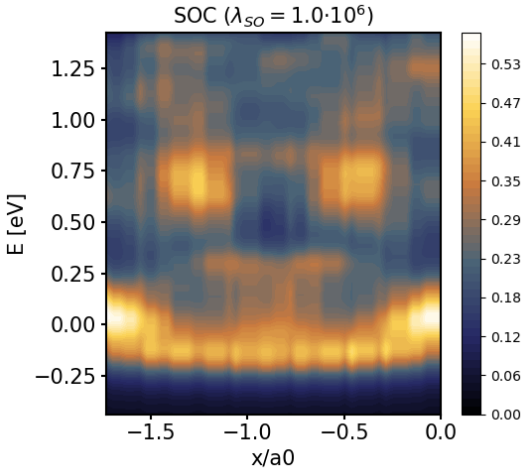

Figure 7.12: Heatmap of the LDOS for the Gaussian potential along the left edge of the Sierpiński following a straight line connecting two red sites.

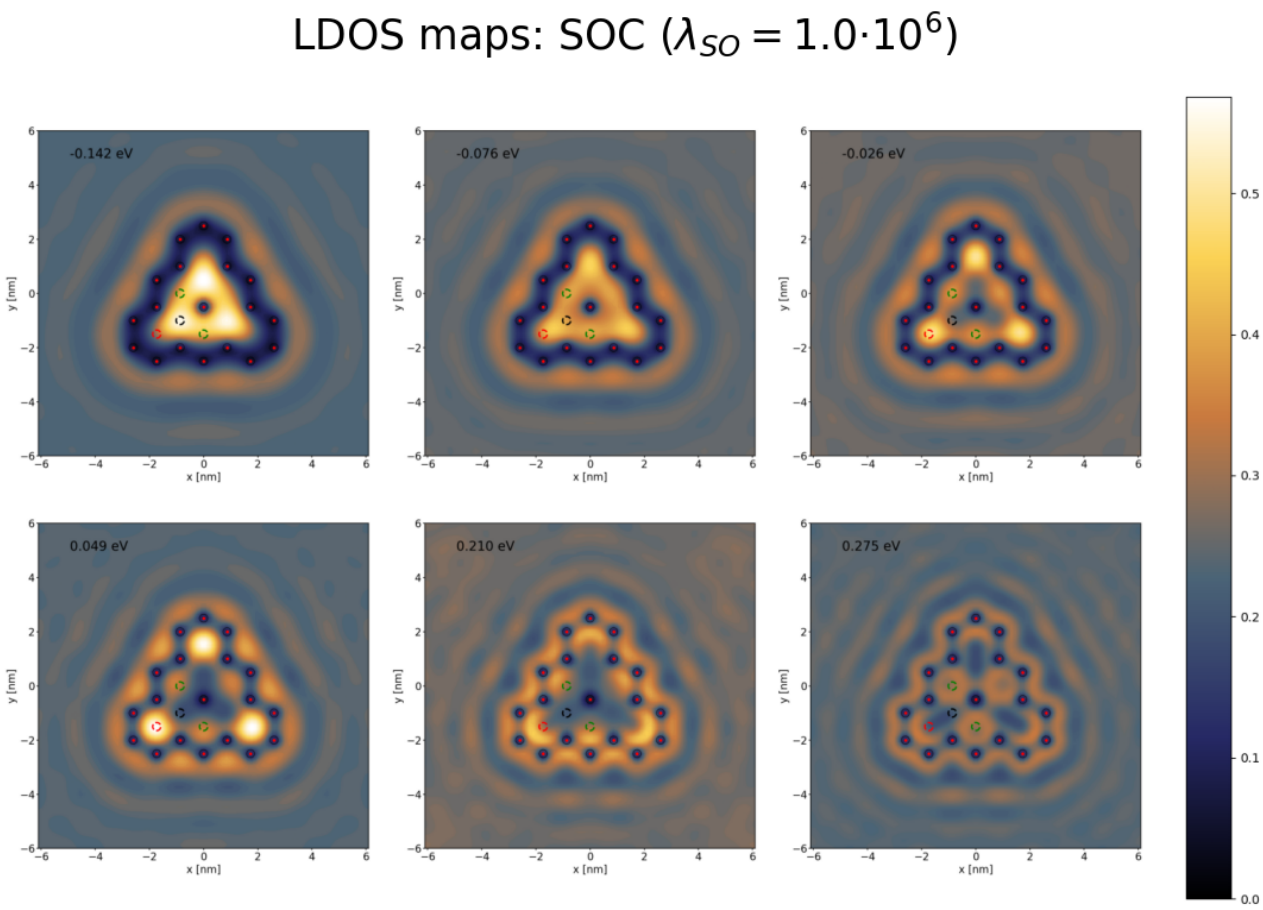

Figure 7.13: Map of the LDOS when including the SOC term. From top left to right bottom, the figures correspond to the values of energy selected in figure 7.11. The maximum of the color bar has been set equal to the LDOS peak of the red site.

7.3 Third generation

Since the Gaussian potential is a more realistic description and shows more features when we include the SOC term, from now on we will only show the results using this potential shape. Next, we will depict the behaviour of higher generations, such as the third one (G=3). In figure 7.14, we show the anti-lattice corresponding to the third generation. Due to self similarity, we have organized all sites by a similar color code as before. Black and blue sites have three NN, green, brown, and salmon have two NN,and the only one that has one NN is the red left low corner. (Similarly for the other three identical triangles, which are self similar upon rotation). When we look at the LDOS plot, we see that all the colors mentioned above are grouped together and follow the same trend as the first generation. The red sites exhibit the highest peak at the non-bonding configuration, and at the same energy value, all the sites with two NN also show a peak, with less intensity. The other sites follow the black curve.

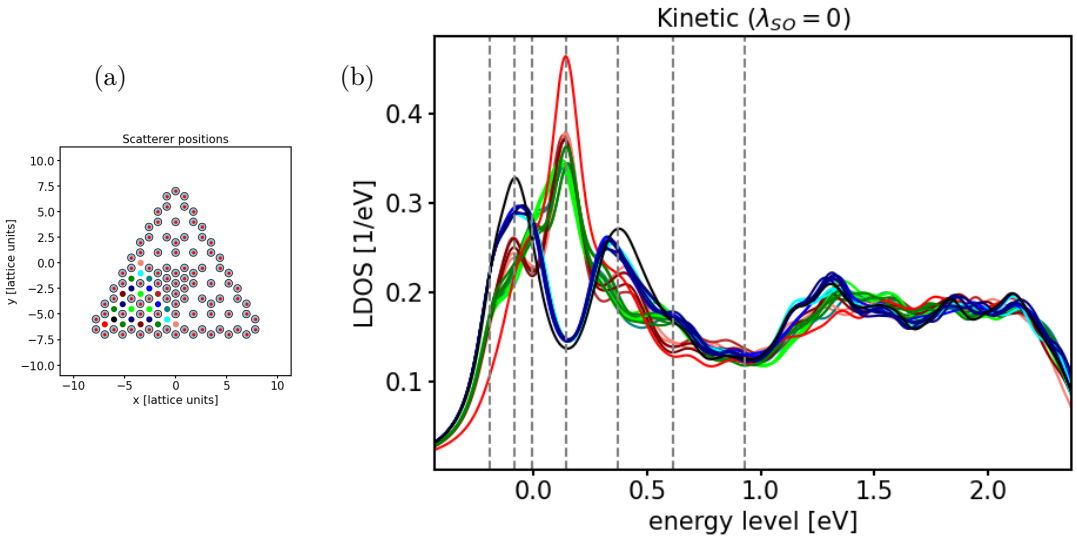

Figure 7.14: (a) Simulation box. The FWHM of the Gaussian potential is given by the blue disk diameter with a red center. Colors of similar code correspond to sites with similar connectivity.(b) LDOS for all different sites when including the SOC term. The dashed lines correspond to selected energies.

Looking at the LDOS mapped to the Cartesian plane shown in figure 7.15, we see that at $E = -0.094$ eV, the highest intensity of the LDOS is along sites connecting the first generations, and there is less occupation at the green sites. On the contrary, at $E = -0.008$ eV, the LDOS has shifted to the full hexagon and sites that connect the first generation have less LDOS, except from the red sites, which remain with high intensity. Then, the characteristic non-bonding configuration appears again, with a bit more predominance at the red sites. Afterwards, the trend continues as for the first generation. However, now there are nine copies building this $G = 3$ Sierpinski triangle. Here, we set the color bar to 80% of the height of the red peak to better visualize the features at higher-order.

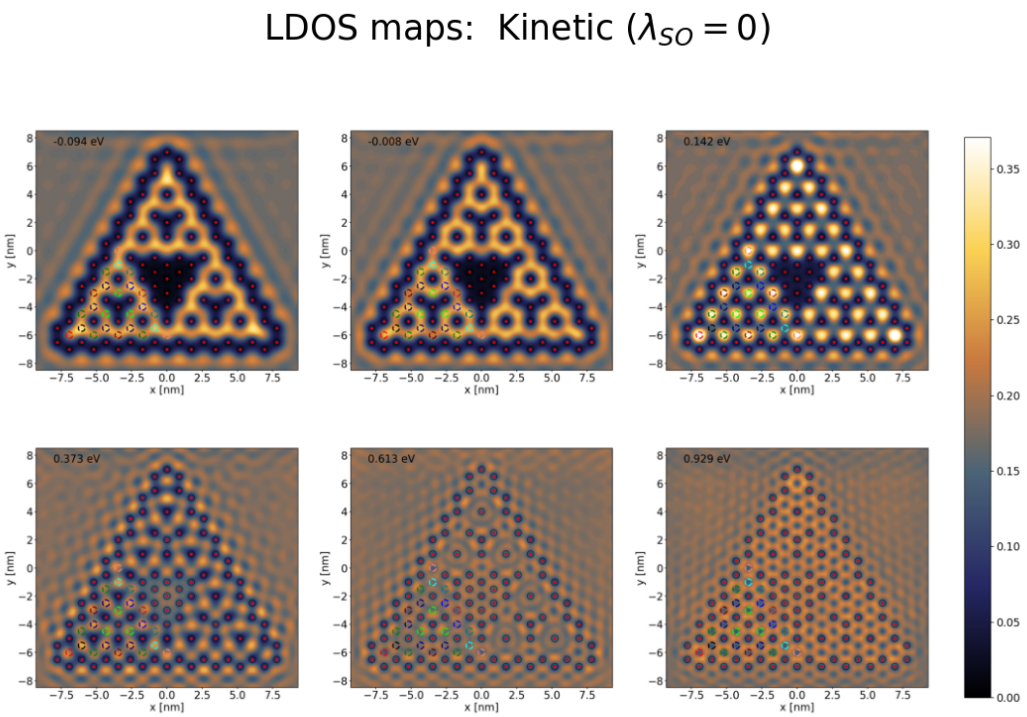

Figure 7.15: Map of the LDOS for the 3rd generation Sierpiński structure. From top left to right bottom, the figures correspond to the selected values of energy from figure 7.14. The maximum of the color bar has been set equal to the 80% LDOS peak of the red site

If we now include the SOC term for this third generation, the results are the same as for the first generation, we only need to scale them accordingly. (see Figs. 7.17 and 7.17) However, now we can see much better the edge states, since the boundary is larger. The first plot in Fig. 7.17 at $E = -0.164$ eV shows nine self-similar copies of the $G = 1$. Each of them exhibit 3 small triangles, with the high intensity mainly localized at the black site. At $E = -0.099$ eV, all sites have nearly equal weight. Now, at $E = -0.044$ eV, we can see the main difference with the lower generations. Instead of only an edge state along the outer larger triangle, there are nine copies of edge states of the first generation. They are extended states, which fully connect the outer and inner perimeters. At $E = 0.041$ eV, on the contrary, we do not find nine copies of corner modes, one for each $G = 1$, but are only the corner modes associated to the larger triangle. For $E = 0.166$ eV, as before, we see that a gap in the LDOS is opened at all the lattice sites, as the LDOS is very low. The difference here is that in addition to the extended edge state along the perimeter of the larger triangle, there are also edge states following the inner perimeter of the second and third generation. Finally, the last plot for $E = 0.252$ eV shows how the LDOS is going from the outer to the inner perimeter of the third generation, surrounding the green sites. The next (not shown) image displays all the LDOS at the inner-scatterers perimeter.

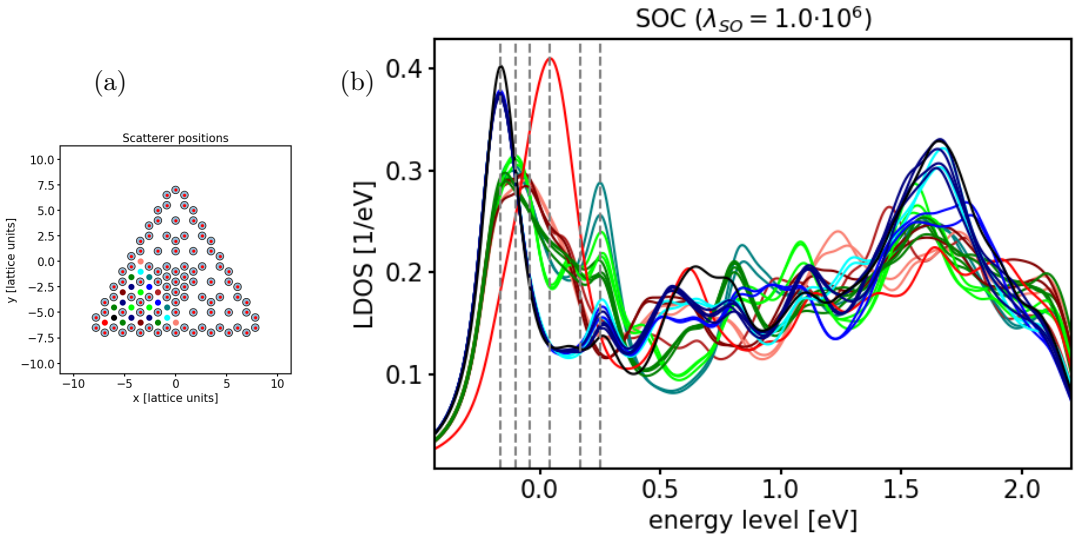

Figure 7.16: (a) Simulation box. The FWHM of the Gaussian potential is given by the blue disk diameter. Colors of similar code correspond to sites with similar connectivity. (b) LDOS for all different sites when including the SOC term. The dashed lines correspond to selected energies.

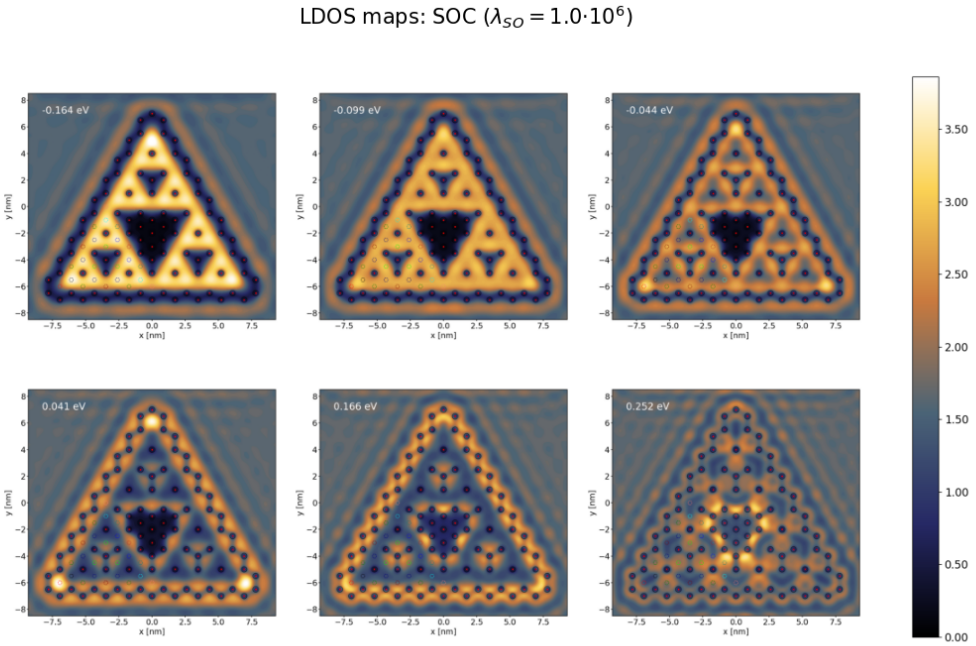

Figure 7.17: Map of the LDOS for the 3rd generation Sierpiński. From top left to right bottom, the figures correspond to the selected values of energy shown in figure 7.16. The maximum of the color bar has been set equal to the 80% of LDOS peak of the red site.

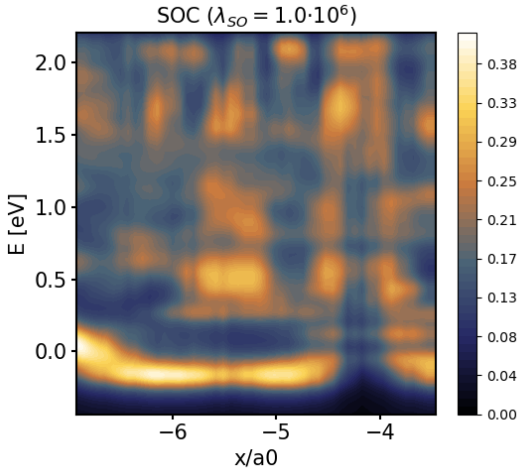

Figure 7.18: Heatmap of the LDOS for the Gaussian potential when including the SOC term. The contour is taken along the left edge of the Sierpiński following a straight line connecting the two red sites of the first generation.

Chapter 8

Comparison between theory and experiments

After obtaining the main theoretical results shown in the previous chapter, we are in a better position to understand the measurements depicted in Fig. 5.10. This chapter aims to compare the experimental measurements done by the group of Jinfeng Jia with our quantum simulations.
In Fig. 8.1, we show an STM image of a sample containing a second generation Sierpiński triangle. However, the structure is not perfect. There is clearly a geometric disorder, but there could be also chemical structural disorder, which would generate a potential difference in that region, or defects, etc. Indeed, it can be observed in Fig. 8.3, that the LDOS does not have a C_3 rotational symmetry, as one would expect from a perfectly clean fractal. We have selected

Figure 8.1: Sample showing a second generation Sierpiński triangle composed of Bi atoms.

the most relevant mappings of the LDOS for the comparison between theory and experiment. To do so, we adopted the same color codes as in the experiments. Figure 8.2 shows two sets of eight figures, where on top there are the experimental measurements, and below the corresponding theoretical simulations. The first two experimental images for the lowest values of the bias voltage, at $E = -507$ meV and $E = -266$ meV, show a good agreement with the theoretical LDOS depicted below them. Both show a high intensity of the LDOS inside the Sierpiński triangle, characterizing a bulk phase. Also, the boundary and the interior hole are perfectly defined with turquoise blue, denoting a low density of states. The next experimental image, at $E = -104$ meV, corresponds to three superposed first generation Sierpiński triangles exhibiting corner modes. Although the theoretical and experimental images are not exactly the same, the one that is closer to the experimental map is the image where we had an edge state along the exterior and interior boundaries. It is possible that there is a missing pink dot at the bottom right of the experimental map due to disorder. This would correspond to five pink blobs along the Sierpiński triangle edges, in the theoretical image. Observe that the corners of the previous generation have a sharper pink blob. The next experimental and

theoretical images at $E = 16.4$ meV also agree, both have corner modes, but there seems to be a missing corner mode, most probably due to disorder. Moving onto the next set of eight figures, at $E = 96.9$ meV the experimental LDOS exhibits an edge state along the Sierpiński triangle boundary, while the interior remains turquoise blue, corresponding to low LDOS. The theoretical maps also shows an image where the boundary surrounding the Sierpiński triangle is pink, which is an edge state. From the outer perimeter, the LDOS gradually goes to the interior perimeter, as shown for $E = 238$ meV. For the corresponding theoretical image, the pink region is mainly localized around the large inner hole. At $E = 318$ meV, the structure observed in the experimental image, forms these pink bubbles, suggesting that they could be related to the LDOS shown in the theoretical image presented below it. However, the experiments might not have enough accuracy to resolve the low LDOS inside the Sierpiński triangle. Finally, in the last picture for $E = 459$ meV, the Sierpiński triangle bulk is all in turquoise blue and the LDOS is outside it. In the theoretical image, there is a high LDOS in the inner hole, but not so much pink outside. This could be due to the fact that there are not scatterers confining the electrons in between the boundaries of the box and the Sierpiński triangle, and hence the wavefunctions decreases exponentially. However, we see the pink dot at the inner center and a relatively pink contour around the structure.

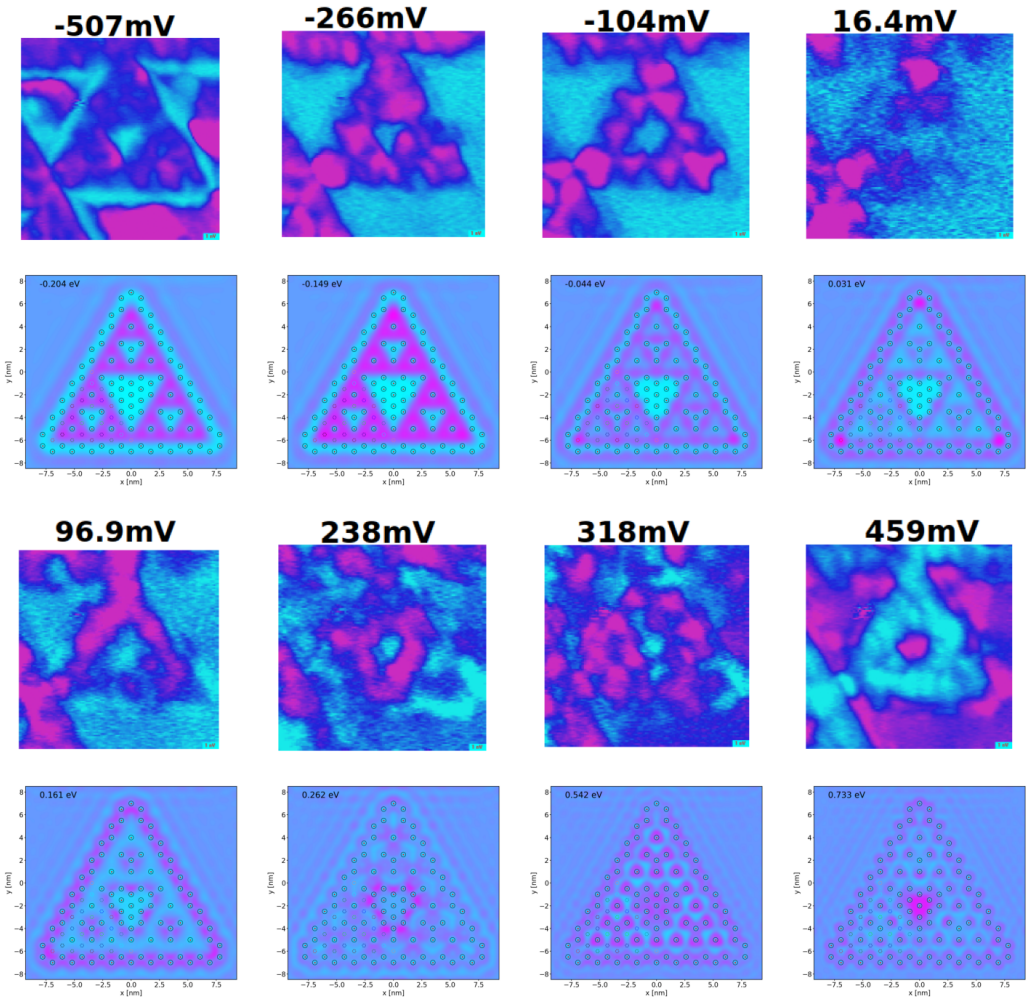

Figure 8.2: Comparison of the experimental and theoretical maps for the most relevant phases observed experimentally. Pink and turquoise blue represent high and low LDOS intensity, respectively.

We discussed in detail the agreement of our calculations with most prominent results observed experimentally, but actually the comparison holds also for other energies, below and above the ones shown in Fig.8.2. Now, we describe the general trends and the different phases distinguished in the full range of energies investigated experimentally. Beginning at the bottom of Fig.8.3, for the lowest value of the bias voltage ($E = -507$ meV), we see a sharp light-blue line surrounding the external boundary and filling the inner hole. Hence, there is a very low LDOS in these regions. Inside the Sierpiński triangle, there are some triangular pink shapes, denoting the high LDOS at the bulk observed in the first generation Sierpiński triangle. As we increase the voltage, the LDOS becomes more defined, and for $E = -447$ meV, we can even identify the hole of the second generation Sierpiński triangle by a darker region in the center of the three smaller triangles. It seems that this corresponds to a bulk phase, where the LDOS is located inside the Sierpiński triangle region. For the next pictures, there is much disorder, and it is not very clear what can be identified. Nevertheless, around $E = -266$ meV, corner modes begin to form for three superposed first-generation Sierpiński triangles. This becomes sharper while increasing the energy, see e.g. the LDOS at $E = -104$ meV, where the top and the left G=1 Sierpiński triangles resemble a three leaf clover (also for the right bottom one, but not as clear). The three-leaf clover could be related to a corner state of the fist generation. Thus, the system is changing from the bulk phase to a corner state of the previous generation. Increasing the bias voltage further, around $E = 16.4$ meV we observe that the corner states that connect the first generation of Sierpiński triangles have disappeared, and now there are only corner states for the top and left corners of the G=2 Sierpiński triangle (we suppose that the last right-bottom corner is missing due to the disorder). From this corner state, the LDOS begins to spread along the edge, as one can see around $E = 96.9$ meV. This could be related to a topological edge state. The next values of voltage that seem to exhibit some clear features are around $E = 218$ meV. Now, the LDOS is localized around the inner hole of the Sierpiński triangle. The next images have too much disorder, and it is not very clear what one can see. At most, it seems that the LDOS in pink is self differentiating in small self-similar parts surrounding the Sierpiński triangle holes (see image at $E = 318$ meV). Finally, at the highest values of bias voltage (from $E = 439$ meV), we find again that all the LDOS is outside the Sierpiński triangle, in agreement with our findings.

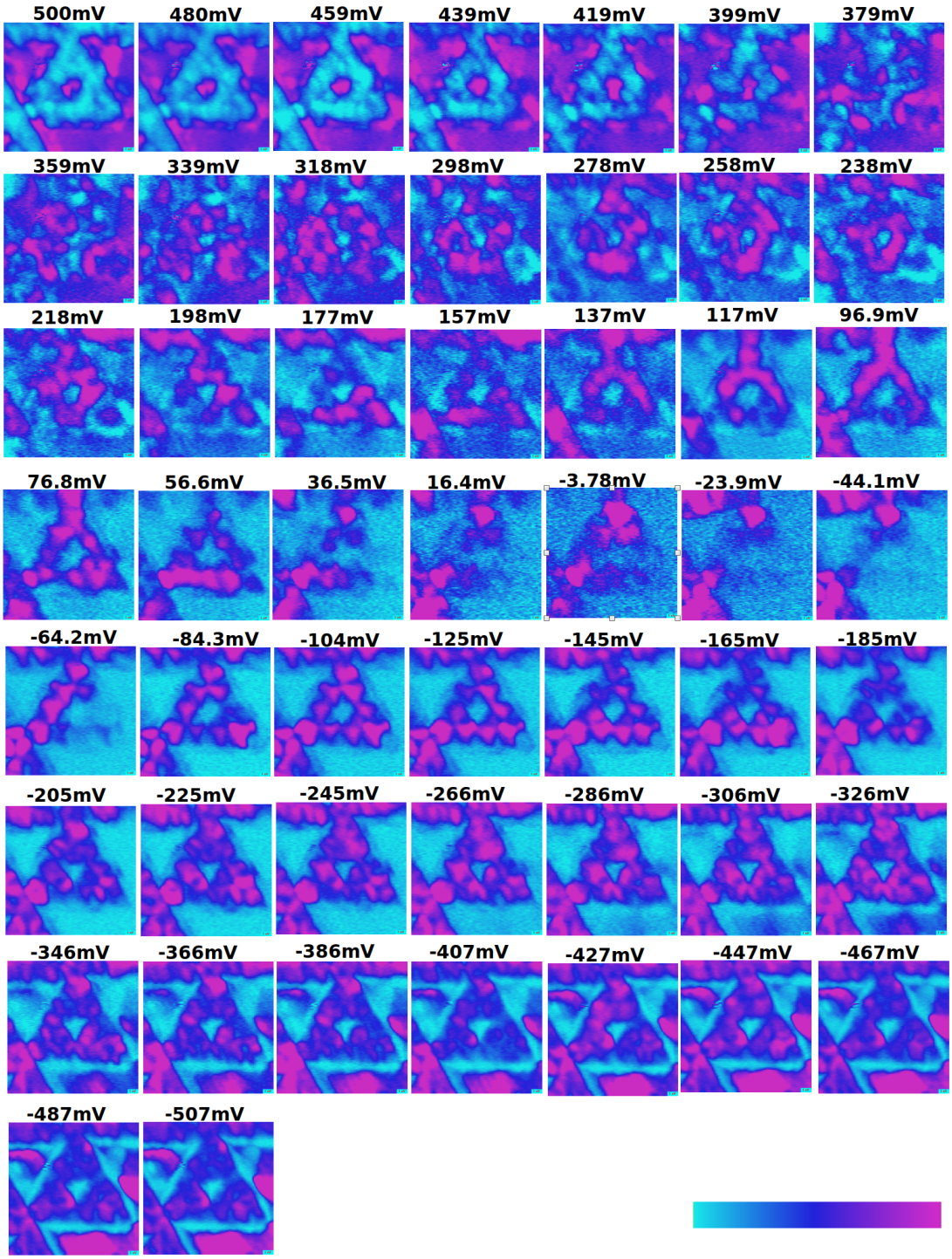

Figure 8.3: Measurements of the LDOS for different values of bias voltage for the sample shown in Fig. 8.1. High intensity is labeled by pink and low intensity by turquoise blue.

Conclusions

In this work, we have studied the effects of the intrinsic spin-orbit coupling in a Sierpiński triangle by performing quantum simulations. We first started by considering a muffin-tin potential and compared the results without SOC with the ones available in the literature. Our findings were shown in chapters 6 and 7. However, to better compare with the experiments performed in real materials, we considered also a Gaussian potential for the continuity barriers. The smoothness of the Gaussian potential is better due to the derivatives of the potential that appear in the spin-orbit coupling term. The Gaussian potential allowed for a more clear transition between phases, enabling us to distinguish new features. The LDOS was also found to be very sensitive due to the implemented method. In addition, enough free space needs to be added around the scatterers to provide a more reliable solution. Hence, the shape and size of the box containing the fractal is also relevant.

When the spin-orbit coupling term is of the order of the kinetic term, new phases such as corner modes and edge states are generated. The sharp corner modes always appear in the vertex of the larger triangle, while the edge modes appear at the outer and inner boundaries. These simulations allow for a much better understanding of the LDOS measured by the group of Jinfeng Jia [8], which were awaiting for some description. We have been able to draw a qualitative comparison, which can describe very well the experimental findings. There is a small difference for one phase, but it can be attributed to a merging of the lobes. Due to their restricted experimental resolution, they are not able to differentiate all of the blobs. Moreover, their samples have much disorder and the results shown do not contain any. Although we did not show implementations of disorder here, we have some preliminary results where we include a geometric disorder to better simulate their topographic images. These results show that whenever different Sierpiński triangles touch each other, the LDOS of the whole sample is shifted towards that point. This indicates that if there is a region that has an overall increase of the potential in comparison with the other regions, the LDOS is going to be more pronounced there. In addition, to seek for a better agreement between theory and experiments, we also studied another type of confinement. Instead of defining an antilattice and a potential centred there, as in the muffin-tin or in the Gaussian, we constructed a straight boundary with a width that had a constant potential. The inner inverted equilateral triangles had a similar straight constant potential everywhere. By implementing these configurations and by rotating the fractal by ten degrees, we obtained the same two corner modes as observed experimentally, with the right corner missing. In addition, the edge estates were also shifted, thus supporting the argument of disorder.

In order to verify whether the corner and edge modes have a topological origin, calculations with a Rashba spin-orbit coupling and a magnetic field have also been (done but not shown). As expected, when the Rashba term is of the order of the kinetic and intrinsic spin-orbit coupling, the corner and edge states do not appear. The system looks more like the one obtained when only the kinetic contribution is present.

Finally, as an outlook, besides more in depth investigations of disorder configurations, it is necessary to calculate topological invariants to the models considered here to better substantiate the argument that the corner and edge modes might have a topological origin. Our work

has answered many of the open questions, but many more remain to be investigated.

Appendix A

Landau Levels in the Continuum

The classical dynamics of an electrons in a static magnetic field is due to the Lorentz force $\mathbf{F_L} = -e\mathbf{v} \times \mathbf{B}$ acting on a charged particle. We can supose that the spin is polarized in the direction of the magnetic field and therefore write the Lagrangian of a spinless electron with charge e and mass m under a magnetic field $\mathbf{B} = \nabla \times \mathbf{A}$ as

$$L = \frac{1}{2}m\dot{\mathbf{x}}^2 - e\dot{\mathbf{x}} \cdot \mathbf{A} \tag{A.1}$$

and obtain the evolution of the trajectories using the Euler-Lagrange equations, or just use the second Newton's law. The quantum treatment begins by writing the hamiltonian in terms of the canonical momentum $\mathbf{p} = \frac{\partial L}{\partial \dot{\mathbf{x}}} = m\dot{\mathbf{x}} - e\mathbf{A}$. This momentum $\mathbf{p}$ does not have any physical interpretation as it is gauge dependent.

$$H = \dot{\mathbf{x}} \cdot \mathbf{p} - L = \frac{1}{2m}(\mathbf{p} + e\mathbf{A})^2 \tag{A.2}$$

As we have promoted our canonical variables $\mathbf{x}$ and $\mathbf{p}$ to operators, we need as well to substitute the Poisson brackets by canonical commutation relations

$$[x_i, p_j] = i\hbar\delta_{ij} \quad \text{and} \quad [x_i, x_j] = [p_i, p_j] = 0 \tag{A.3}$$

Similarly the commutator for the mechanical momentum $\boldsymbol{\pi} = m\dot{\mathbf{x}} = \mathbf{p} + e\mathbf{A}$ is

$$[\pi_x, \pi_y] = -ie\hbar\epsilon_{xyz}B_z = -ieB \tag{A.4}$$

restricting the motion in xy plane with a perpendicular magnetic field $\mathbf{B} = B\hat{z}$ for simplicity. What we have left now is to define the usual creation $a^\dagger$, and annihilation a operators in terms of the mechanical momentum operator, which will allow us to rewrite the Hamiltonian in a quantized form

$$a = \frac{1}{\sqrt{2e\hbar B}}(\pi_x - i\pi_y) \quad \text{and} \quad a^\dagger = \frac{1}{\sqrt{2e\hbar B}}(\pi_x + i\pi_y) \quad \text{obeying} \quad [a, a^\dagger] = 1 \tag{A.5}$$

Using $\{|n\rangle\}$ as the eigenbasis that spans the Hilbert space with the ground state $|0\rangle$ obeying $a|0\rangle$. Then, by acting with the creation operator we can generate the rest. With the new set of operators the Hamiltonian reads

$$H = \frac{1}{2}\boldsymbol{\pi} \cdot \boldsymbol{\pi} = \hbar\omega_B(a^\dagger a + \frac{1}{2}), \tag{A.6}$$

with $\omega_B = \frac{eB}{m}$ the cyclotron frequency. To obtain the energy spectrum we use the eigenvalue equation $H|n\rangle = E_n|n\rangle$ with energy $E_n = \frac{1}{2}\hbar\omega_B(n + \frac{1}{2})$. This are the so called Landau levels (LL), quantized with integer n and a gap proportional to the cyclotron frequency. Each of them do not have a single state assigned, they are wildly degenerated as the energy E_n is

independent of k. This approach is useful as the spectrum can be obtained easily, but also have several restrictions. Does not allow to write wavefunctions in the position space and does not exploit all the symmetries of the Hamiltonian. To understand this we can see that the motion of particles have two degrees of freedom, but we only associated one quantum number. To completely describe the system one should find another operator that commutes with the Hamiltonian and form a complete set of commuting observables. We can use the gauge freedom ot the vector potential $\boldsymbol{A} \to \boldsymbol{A} + \nabla\alpha$, that leaves invariant the magnetic field $\boldsymbol{B} = \nabla \times \mathbf{A} + \nabla \times (\nabla\alpha)$ due to Schwart's theorem, to explore those preserved symmetries.

In the Landau gauge, $\boldsymbol{A} = xB\hat{y}$, we have translation invariance in the y direction. This will define the other quantum number. The Hamiltonian becomes

$$H = \frac{1}{2m}(p_x^2 + (p_y + eBx)^2) \tag{A.7}$$

We know that in the y direction the solution will be plane waves, therefore we only need to solve for the x-dependent part. This is the harmonic oscillator equation with equilibrium position $x_0 = -kl_m^2$ and magnetic length $l_m = \sqrt{\frac{\hbar}{eB}}$

$$H_k(p_x, x)f_k(x) = \frac{1}{2m}\left[p_x^2 + \frac{m\omega_B}{2}(x - x_0)^2\right] f_k(x) \tag{A.8}$$

The solution, quantized with two quantum numbers n and k, can be written in terms of the Hermite polynomials, $\mathcal{H}_n$

$$f_{nk}(x) = \frac{1}{\sqrt{2^n n! l_m \pi^{1/2}}}\mathcal{H}_n\left(\frac{x - x_0}{l_m}\right) e^{-(x-x_0)^2/2l_m^2} \tag{A.9}$$

To determine the degeneracy one needs to fix the dimension of the sample $A = L_x L_y$ which will quantize the electron momentum k in units of $2\pi/L_y$ in the y-direction. For the x-direction the momentum will lie in the range $-L_x/l_m^2 \leq k \leq 0$. Summing all the available states in one LL gives:

$$\mathcal{N} = \frac{L_y}{2\pi}\int_{-L_x/l_m^2}^{0} dk = \frac{A}{2\pi l_m^2} = \frac{BA}{\phi_0} \tag{A.10}$$

with $\phi_0 = h/e$ the quantum flux. See that each LL has the same degeneracy of states.
If now the electrons are also under the influence of an Elecric field $\boldsymbol{E}$ in the x-direction, we will need to add the corresponding electric potential to the Hamiltonian

$$H = \frac{1}{2m}(p_x^2 + (p_y + eBx)^2) + eEx \tag{A.11}$$

completing the square we can rewrite the Hamiltonian as before but now the equilibrium position is shifted to $x_0 + \frac{mE}{eB^2}$. Furthermore the energy levels now are tilled, as they depend linearly on k and all LL are lifted by a kinetic constant term.

$$E_{nk} = \hbar\omega_B\left(n + \frac{1}{2}\right) + k\hbar\frac{E}{B} + \frac{1}{2}m\left(\frac{E}{B}\right)^2 \tag{A.12}$$

With group velocity given by $v_y = \frac{1}{\hbar}\frac{\partial E_{nk}}{\partial k} = \frac{E}{B}$ and we see how the wavepackets localized at x_0 they move in the direction $\boldsymbol{E} \times \boldsymbol{B}$.

Appendix B

Comparison between theory and experiments

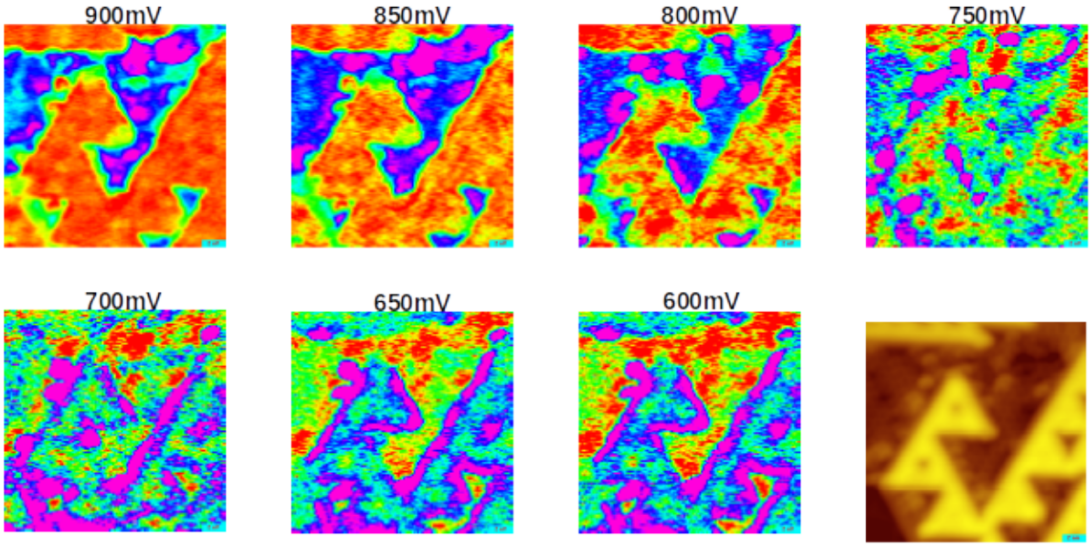

Figure B.1

To conclude the comparison between our theoretical results and the experimental measurements, it is presented in Fig. B.2 the same selected images as above, but now with the high contrast color bar. See, if by changing the color code, phases can be better compared. The first theoretical image, at the lowest energy, exhibits the trend in a more fine way than in Fig. 8.2. The LDOS in pink appears discontinuously first at each building block of a Sierpiński triangle (the equilateral triangle). It is completely localized at the black site surrounded by a blue boundary. When compared with the the experimental image at $E = -507$ meV, there are similar features as it also have disconnected pink regions, surrounding the Sierpiński triangle holes. However, disorder does not allow us to confirm this for sure. At $E = -266$ meV, the pink region now is not as similar as the theoretical bulk configuration below. Before at Fig. 8.2 there was a better agreement. The next one, at $E = -104$ meV either the experimental and theoretical images have a more confined region for the pink lobes. However, the theoretical image looks more like an edge state, with high intensity at each triangle corner, and the experimental shows only corner modes for each G=1 Sierpiński triangle. At $E = 16.4$ meV there is also a good agreement, either theoretical and experimental display corner modes. The two following experimental images at $E = 96.9$ meV and $E = 238$ meV, exhibit the the mentioned edge states at the outer and inner boundaries. With this new color code, the the-

oretical edge states are more sharp. At $E = 319$ meV, the experimental image shows less disorder than before at Fig. 8.2. The pink regions forming this bubbles surrounding the holes of the Sierpiński triangle, are better defined. Looking at the theoretical image below, seems as well that the regions where there is LDOS in pink is similar as the experimental. Finally, at $E = 459$ meV, there is an empty Sierpiński triangle for both experimental and theoretical images, although they differ with the intensity. Also in both the high LDOS in pink is inside the central Sierpiński triangle hole.

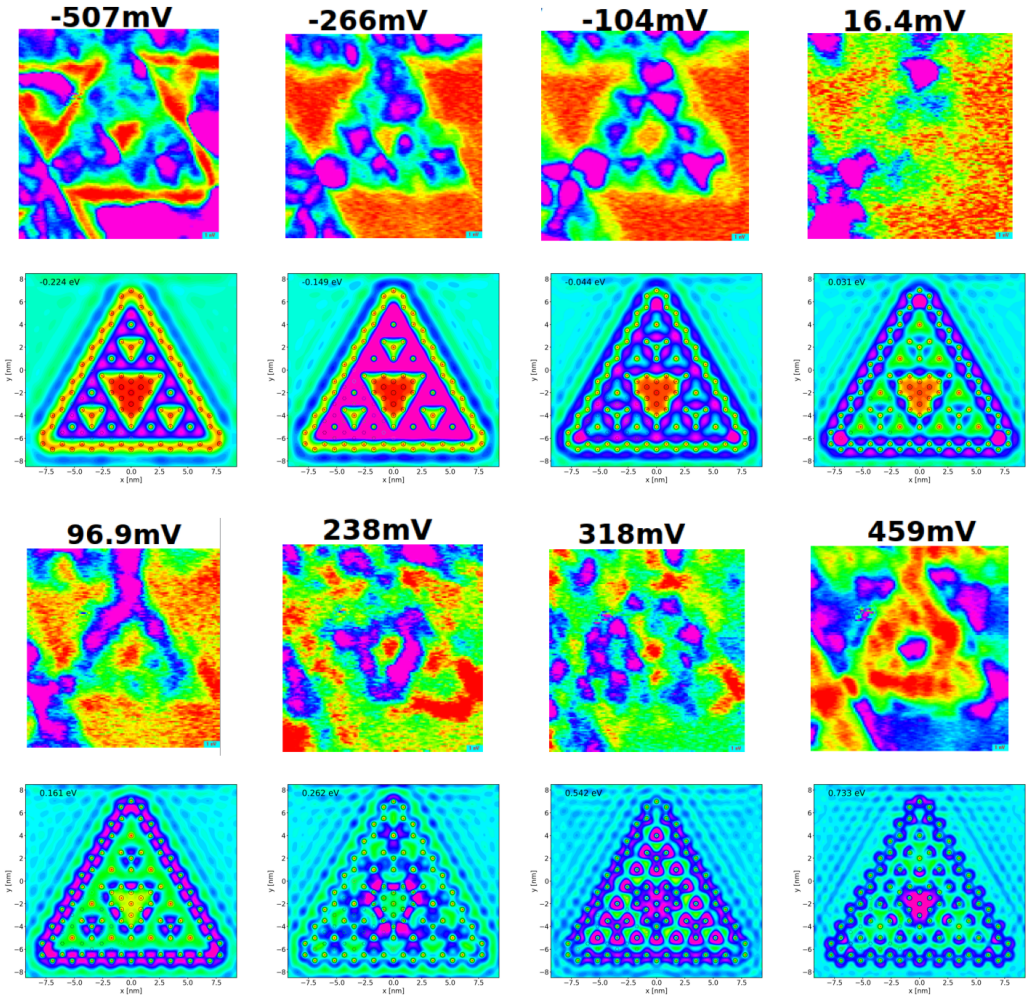

Figure B.2: Same experimental and theoretical comparison, but now using the most relevant phases observed at Fig. B.3. Pink and red represent high and low LDOS intensity respectively.

Figure B.3 shows again the same results, but now using the high contrast color map. This helps for distinguishing the relevant phases mentioned before. At the lowest value, for $E = -507$ meV, the pink bulk phase begins to form, but is not completely filled. However, we can see a perfect red edge and the red hole at the interior of the Sierpiński triangle. The bulk phase observed before at $E = -266$ meV, is not as clear for this color map. Nevertheless, the trend seems to be the same. First LDOS spreads around the Sierpiński triangle bulk, then begins to form the three leafs clove, which is shown to be more localized at the corners of the G=1 Sierpiński triangles, around $E = -104$ meV. Then, the corner modes of the second generation of the Sierpiński triangle gain predominance, through increasing the bias voltage , and at 16.4 meV, they are completely developed. Subsequently, the corner modes shift to an edge state, which first is at the outer boundary (see e.g. $E = 96.9$ meV), and then at $E = 238$ meV, to the inner boundary. At $E = 318$ meV, now shows better the localization of the pink circles, but there is still too much disorder. For the last values we can see again the same, from $E = 439$ meV the LDOS is beginning to be localized at the exterior and the interior is filled with red, labeling low LDOS.

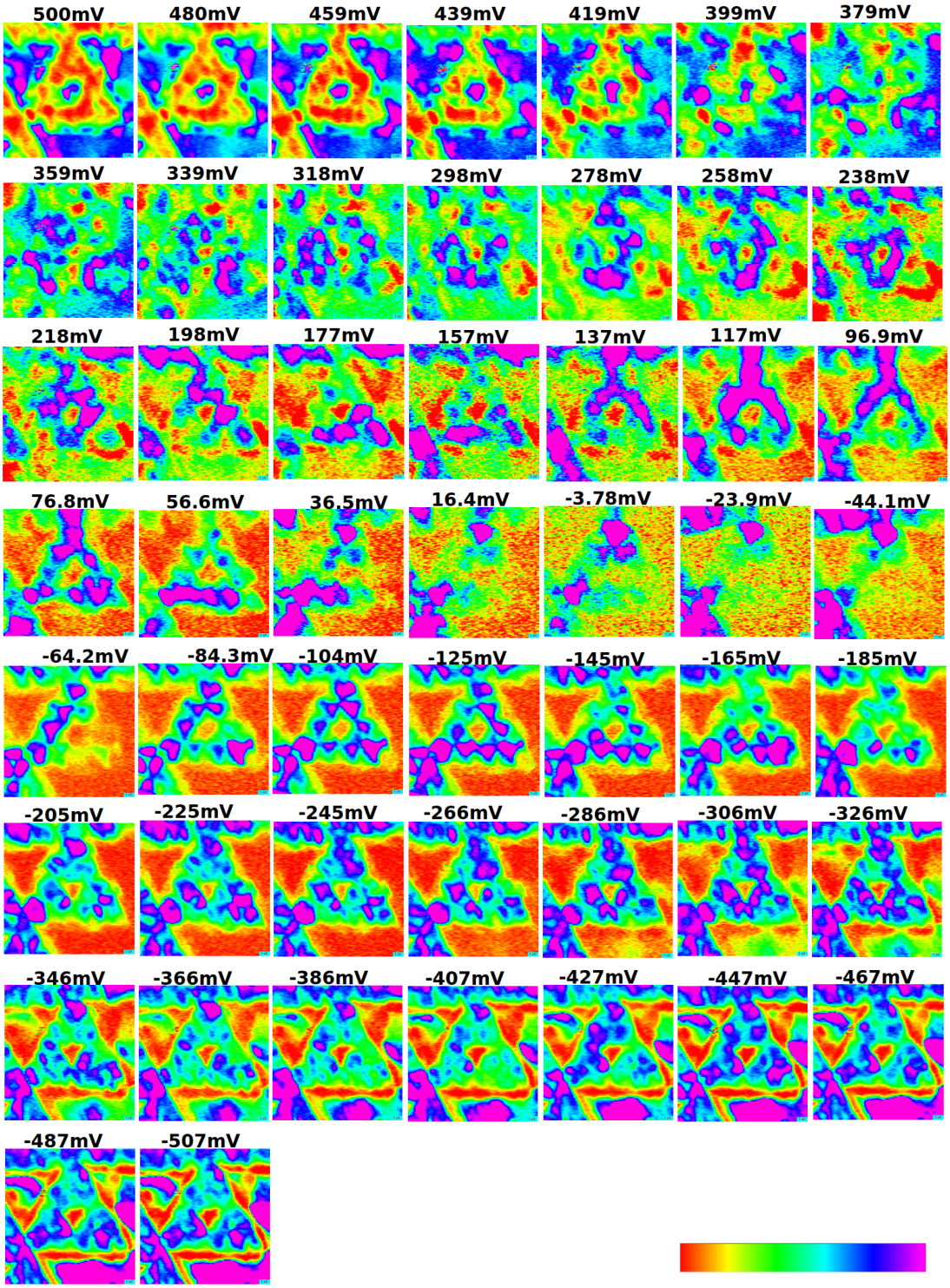

Figure B.3: Same measurements of the LDOS as Fig. 8.3, but now with a high contrast color code. High intensity is labeled by color pink and low intensity by red.

Bibliography

[1] J. M. Kosterlitz and D. J. Thouless. *Ordering, metastability and phase transitions in two-dimensional systems.* Journal of Physics C: Solid State Physics **6** (1973), 1181.

[2] K. v. Klitzing, G. Dorda, and M. Pepper. *New method for high-accuracy determination of the fine-structure constant based on quantized Hall resistance.* Physical Review Letters **45** (1980), 494.

[3] D. J. Thouless, M. Kohmoto, M. P. Nightingale, and M. den Nijs. *Quantized Hall Conductance in a Two-Dimensional Periodic Potential.* Phys. Rev. Lett. **49** (1982), 405.

[4] C. L. Kane and E. J. Mele. *Quantum spin Hall effect in graphene.* Physical review letters **95** (2005), 226801.

[5] C. L. Kane and E. J. Mele. *Z 2 topological order and the quantum spin Hall effect.* Physical review letters **95** (2005), 146802.

[6] F Reis et al. *Bismuthene on a SiC substrate: A candidate for a high-temperature quantum spin Hall material.* Science **357** (2017), 287.

[7] A. Altland and M. R. Zirnbauer. *Nonstandard symmetry classes in mesoscopic normal-superconducting hybrid structures.* Physical Review B **55** (1997), 1142.

[8] C. Liu et al. *Sierpiński Structure and Electronic Topology in Bi Thin Films on InSb (111) B Surfaces.* Physical Review Letters **126** (2021), 176102.

[9] A. Altland and B. D. Simons. *Condensed Matter Field Theory.* 2nd ed. Cambridge University Press, 2010.

[10] E. C. Marino. *Quantum Field Theory Approach to Condensed Matter Physics.* Cambridge University Press, 2017.

[11] R. Shankar. *Quantum Field Theory and Condensed Matter: An Introduction.* Cambridge University Press, 2017.

[12] X.-L. Qi and S.-C. Zhang. *Topological insulators and superconductors.* Rev. Mod. Phys. **83** (2011), 1057.

[13] G. Binnig, H. Rohrer, C. Gerber, and E. Weibel. *Tunneling through a controllable vacuum gap.* Applied Physics Letters **40** (1982), 178.

[14] G. Binnig, H. Rohrer, C. Gerber, and E. Weibel. *Surface Studies by Scanning Tunneling Microscopy.* Phys. Rev. Lett. **49** (1982), 57.

[15] G. Binnig, C. F. Quate, and C. Gerber. *Atomic Force Microscope.* Phys. Rev. Lett. **56** (1986), 930.

[16] A. Liebsch. *Theory of the angular-resolved photoemission from TaS2.* Solid State Communications **19** (1976), 1193.

[17] F. J. Himpsel and D. E. Eastman. *Experimental energy dispersions for valence and conduction bands of palladium.* Phys. Rev. B **18** (1978), 5236.

[18] A. Kampf and J. R. Schrieffer. *Pseudogaps and the spin-bag approach to high-T_c superconductivity.* Phys. Rev. B **41** (1990), 6399.

[19] J. A. Sobota, Y. He, and Z.-X. Shen. *Angle-resolved photoemission studies of quantum materials*. Rev. Mod. Phys. **93** (2021), 025006.

[20] F. Giustino et al. *The 2021 quantum materials roadmap*. Journal of Physics: Materials **3** (2020), 042006.

[21] L. Hoddeson, G. Baym, and M. Eckert. *The development of the quantum-mechanical electron theory of metals: 1928—1933*. Rev. Mod. Phys. **59** (1987), 287.

[22] L. D. L. D. Landau. *Statistical physics / by L.D. Landau and E.M. Lifshitz ; translated from the Russian by J.R. Sykes and M.J. Kearsley*. eng. 3d ed. / by E.M. Lifshitz and L.P. Pitaevskiĭ. Their Course of theoretical physics ; v. 9, pt. 2. Oxford ; Pergamon Press, 1980. isbn: 0080230733.

[23] L. P. Pitaevskii and E. M. Lifshitz. *Statistical Physics, Part 2: Volume 9 (Course of Theoretical Physics Vol. 9)*. Butterworth-Heinemann, Jan. 1980. isbn: 0750626364.

[24] X.-G. Wen. *Topological orders and edge excitations in FQH states*. Adv. Phys. **44** (1995), 405.

[25] J. M. Lee. *Introduction to Topological Manifolds*. 1st ed. Vol. 202. Graduate Texts in Mathematics. Springer, May 2000.

[26] B. Bernevig and T. Hughes. *Topological Insulators and Topological Superconductors*. Princeton University Press, 2013.

[27] J. Asbóth, L. Oroszlány, and A. Pályi. *A Short Course on Topological Insulators: Band Structure and Edge States in One and Two Dimensions*. Lecture Notes in Physics. Springer International Publishing, 2016.

[28] N. W. Ashcroft and N. D. Mermin. *Solid State Physics*. Holt-Saunders, 1976.

[29] J. Bardeen, L. N. Cooper, and J. R. Schrieffer. *Microscopic Theory of Superconductivity*. Phys. Rev. **106** (1957), 162.

[30] J. Bardeen, L. N. Cooper, and J. R. Schrieffer. *Theory of Superconductivity*. Phys. Rev. **108** (1957), 1175.

[31] X.-L. Qi, T. L. Hughes, and S.-C. Zhang. *Topological field theory of time-reversal invariant insulators*. Phys. Rev. B **78** (2008), 195424.

[32] J. E. Moore and L. Balents. *Topological invariants of time-reversal-invariant band structures*. Phys. Rev. B **75** (2007), 121306.

[33] R. Roy. *Topological phases and the quantum spin Hall effect in three dimensions*. Phys. Rev. B **79** (2009), 195322.

[34] L. Fu, C. L. Kane, and E. J. Mele. *Topological insulators in three dimensions*. Physical review letters **98** (2007), 106803.

[35] L. Fu and C. L. Kane. *Topological insulators with inversion symmetry*. Phys. Rev. B **76** (2007), 045302.

[36] D. Tong. *Lectures on the Quantum Hall Effect*. 2016.

[37] P. W. Anderson. *Absence of diffusion in certain random lattices*. Physical review **109** (1958), 1492.

[38] D. C. Tsui, H. L. Stormer, and A. C. Gossard. *Two-dimensional magnetotransport in the extreme quantum limit*. Physical Review Letters **48** (1982), 1559.

[39] D. J. Thouless, M. Kohmoto, M. P. Nightingale, and M. den Nijs. *Quantized Hall conductance in a two-dimensional periodic potential*. Physical Review Letters **49** (1982), 405.

[40] M. V. Berry. *Quantal phase factors accompanying adiabatic changes*. Proceedings of the Royal Society of London. A. Mathematical and Physical Sciences **392** (1984), 45.

[41] E. Noether. *Invariant variation problems*. Transport Theory and Statistical Physics **1** (1971), 186.

[42] A. Uhlmann. *Anti-(conjugate) linearity*. Science China Physics, Mechanics & Astronomy **59** (2016), 1.

[43] E. P. Wigner. *On the statistical distribution of the widths and spacings of nuclear resonance levels*. Mathematical Proceedings of the Cambridge Philosophical Society **47** (1951), 790–798.

[44] E. P. Wigner. *On the Distribution of the Roots of Certain Symmetric Matrices*. Annals of Mathematics **67** (1958), 325.

[45] F. J. Dyson. *The Threefold Way. Algebraic Structure of Symmetry Groups and Ensembles in Quantum Mechanics*. Journal of Mathematical Physics **3** (1962), 1199.

[46] P. Heinzner, A Huckleberry, and M. R. Zirnbauer. *Symmetry classes of disordered fermions*. Communications in mathematical physics **257** (2005), 725.

[47] A. P. Schnyder, S. Ryu, A. Furusaki, and A. W. W. Ludwig. *Classification of topological insulators and superconductors in three spatial dimensions*. Phys. Rev. B **78** (2008), 195125.

[48] S. Ryu, A. P. Schnyder, A. Furusaki, and A. W. W. Ludwig. *Topological insulators and superconductors: tenfold way and dimensional hierarchy*. New Journal of Physics **12** (2010), 065010.

[49] A. W. W. Ludwig. *Topological phases: classification of topological insulators and superconductors of non-interacting fermions, and beyond*. Physica Scripta **T168** (2015), 014001.

[50] C.-K. Chiu, J. C. Y. Teo, A. P. Schnyder, and S. Ryu. *Classification of topological quantum matter with symmetries*. Rev. Mod. Phys. **88** (2016), 035005.

[51] A. Kitaev. "Periodic table for topological insulators and superconductors". *AIP Conference Proceedings*. Vol. 1134. AIP. 2009, 22.

[52] E. Wigner. *Group Theory: And its Application to the Quantum Mechanics of Atomic Spectra*. Pure and applied physics. Elsevier Science, 2012.

[53] H. A. Kramers. *Théorie générale de la rotation paramagnétique dans les cristaux*. Proc. Acad. Amst **33** (1930).

[54] G. Akemann, J. Baik, and P. Di Francesco. *The Oxford handbook of random matrix theory*. Oxford University Press, 2011.

[55] É. Cartan. *Sur une classe remarquable d'espaces de Riemann*. Bulletin de la Société mathématique de France **54** (1926), 214.

[56] É. Cartan. *Sur une classe remarquable d'espaces de Riemann. II*. Bulletin de la Société Mathématique de France **55** (1927), 114.

[57] P. A. Lee and T. Ramakrishnan. *Disordered electronic systems*. Reviews of modern physics **57** (1985), 287.

[58] S. Fischer et al. *Robustness of chiral edge modes in fractal-like lattices below two dimensions: A case study*. Physical Review Research **3** (2021), 043103.

[59] M. Fremling, M. van Hooft, C. M. Smith, and L. Fritz. *Existence of robust edge currents in Sierpiński fractals*. Phys. Rev. Research **2** (2020), 013044.

[60] F. Hausdorff. *Dimension und äußeres Maß*. Mathematische Annalen **79** (1918), 157.

[61] P. C. Ivanov et al. *Multifractality in human heartbeat dynamics*. Nature **399** (1999), 461.

[62] E. R. Weibel. *Fractal geometry: a design principle for living organisms*. American Journal of Physiology-Lung Cellular and Molecular Physiology **261** (1991), L361.

[63] E. E. Peters. *Fractal structure in the capital markets*. Financial Analysts Journal **45** (1989), 32.

[64] F. Salvat. *Física Atómica y Radiación*. Facultat de Física Universitat de Barcelona, 2016.

[65] J. D. Jackson. *Classical electrodynamics*. American Association of Physics Teachers, 1999.

[66] J. J. Sakurai and E. D. Commins. *Modern quantum mechanics, revised edition*. 1995.

[67] Y. Yao, F. Ye, X.-L. Qi, S.-C. Zhang, and Z. Fang. *Spin-orbit gap of graphene: First-principles calculations*. Physical Review B **75** (2007), 041401.

[68] M. Konig et al. *Quantum spin Hall insulator state in HgTe quantum wells*. Science **318** (2007), 766.

[69] A. Roth et al. *Nonlocal transport in the quantum spin Hall state*. Science **325** (2009), 294.

[70] C. Liu, T. L. Hughes, X.-L. Qi, K. Wang, and S.-C. Zhang. *Quantum Spin Hall Effect in Inverted Type-II Semiconductors*. Phys. Rev. Lett. **100** (2008), 236601.

[71] G. Li et al. *Theoretical paradigm for the quantum spin Hall effect at high temperatures*. Physical Review B **98** (2018), 165146.

[72] N. Wittemeier, P. Ordejón, and Z. Zanolli. *Tuning the Topological Band Gap of Bismuthene with Silicon-based Substrate*. arXiv:2203.00114 ().

[73] S. Murakami. *Quantum spin Hall effect and enhanced magnetic response by spin-orbit coupling*. Physical Review Letters **97** (2006), 236805.

[74] Z. Liu et al. *Stable nontrivial Z 2 topology in ultrathin Bi (111) films: a first-principles study*. Physical review letters **107** (2011), 136805.

[75] M Wada, S Murakami, F Freimuth, and G Bihlmayer. *Localized edge states in two-dimensional topological insulators: Ultrathin Bi films*. Physical Review B **83** (2011), 121310.

[76] P. Hohenberg and W. Kohn. *Inhomogeneous Electron Gas*. Phys. Rev. **136** (1964), B864.

[77] W. Kohn and L. J. Sham. *Self-Consistent Equations Including Exchange and Correlation Effects*. Phys. Rev. **140** (1965), A1133.

[78] S. N. Kempkes et al. *Design and characterization of electrons in a fractal geometry*. Nature physics **15** (2019), 127.

[79] X.-Y. Xu, X.-W. Wang, D.-Y. Chen, C. M. Smith, and X.-M. Jin. *Quantum transport in fractal networks*. Nature Photonics **15** (2021), 703.

[80] E. Farhi and S. Gutmann. *Quantum computation and decision trees*. Phys. Rev. A **58** (1998), 915.

[81] Z Darázs and T Kiss. *Pólya number of the continuous-time quantum walks*. Physical Review A **81** (2010), 062319.

[82] E. Agliari, A. Blumen, and O. Mülken. *Dynamics of continuous-time quantum walks in restricted geometries*. Journal of Physics A: Mathematical and Theoretical **41** (2008), 445301.

[83] H. Tang et al. *Experimental two-dimensional quantum walk on a photonic chip*. Science advances **4** (2018), eaat3174.

[84] T. Biesenthal et al. *Fractal photonic topological insulators*. Science **376** (2022), 1114.

[85] X. Zhang et al. *Robust Sierpiński triangle fractals on symmetry-mismatched Ag (100)*. Chemical Communications **52** (2016), 10578.

[86] Q. Sun, L. Cai, H. Ma, C. Yuan, and W. Xu. *On-surface construction of a metal–organic Sierpiński triangle*. Chemical Communications **51** (2015), 14164.

[87] Y. Wang et al. *Construction and properties of Sierpiński triangular fractals on surfaces*. ChemPhysChem **20** (2019), 2262.

[88] J. van den Broeke, I Swart, C. M. Smith, and D Vanmaekelbergh. *Spin-orbit gaps in the s and p orbital bands of an artificial honeycomb lattice.* arXiv:2104.06912 (2021).

[89] K. K. Gomes, W. Mar, W. Ko, F. Guinea, and H. C. Manoharan. *Designer Dirac fermions and topological phases in molecular graphene.* Nature **483** (2012), 306.